Flexible flapping airfoil propulsion at low Reynolds numbers

Heathcote, Samuel Francis

Award date:
2006

Awarding institution:
University of Bath

FLEXIBLE FLAPPING AIRFOIL PROPULSION AT LOW REYNOLDS NUMBERS

Samuel Francis Heathcote

A thesis submitted for the degree of Doctor of Philosophy

University of Bath

Department of Mechanical Engineering

ProQuest LLC
789 East Eisenhower Parkway
P.O. Box 1346
Ann Arbor, MI 48106-1346

ABSTRACT

There is renewed interest in the aerodynamics of oscillating airfoils because of the wish to build flapping-wing Micro Air Vehicles (MAVs). To study the role of wing flexibility, an experimental investigation of the effect of chordwise and spanwise flexibility on the propulsive characteristics of an oscillating wing has been carried out for Reynolds numbers of zero to 30,000. Laser Doppler Velocimetry (LDV), Particle Image Velocimetry (PIV), dye flow visualisation, thrust and efficiency measurements were taken in a water tunnel over a range of oscillation frequencies, amplitudes, and airfoil flexibilities. The airfoil was oscillated in pure heave.

The chordwise-flexible airfoil was observed to pitch passively, and an analogy was made with a rigid airfoil in coupled heave and pitch. Optimum flexibilities were found to yield high thrust coefficients and efficiencies relative to the rigid airfoil case. Peak efficiency was observed for pitch phase angles of 95-100 degrees, (consistent with experimental and Navier-Stokes analyses of rigid airfoils in coupled heave and pitch) and a Strouhal number of 0.29, which lies within the range observed in nature of 0.2-0.4. Peak thrust coefficient was observed for pitch phase angles of 110-120 degrees, consistent with values for rigid airfoils in coupled heave and pitch in the literature. Studies of the flow field revealed stronger trailing-edge vortices corresponding to higher thrust coefficients, and weaker leading-edge vortices corresponding to higher efficiencies. At high Strouhal numbers the jet from the airfoil was found to be deflected away from the freestream direction. The direction of the jet was observed to switch periodically with a period of order 100 oscillations. A degree of spanwise flexibility was also found to increase efficiency.

Chordwise flexibility is suggested as an alternative, and mechanically simpler, way to achieve a coupled heave and pitch motion than traditional mechanical linkages. From a design aspect, flexibility may benefit flapping wing MAVs both aerodynamically and in the inherent lightness of flexible structures.

ACKNOWLEDGEMENTS

This work has been supported by an EPSRC (Engineering and Physical Sciences Research Council) studentship.

The author is grateful for the support, ideas, focus and enthusiasm of supervisor Prof. I. Gursul, and for the help of technicians Mr D. Rushton, Mr L. Dudrudge, Mr R. Wiltshire, and Mr P. Griffiths, instrumentation specialists Mr P. Prest, Mr R. Grant, and Mr P. Philips, and rapid prototyping specialist Mr A. Green. The author is also grateful to Dr J. A. Whitehead for his enthusiasm and guidance in experimental techniques.

The author is appreciative of the support and humour of everyone in the office: Gordon, Colin, Panagiotis, Eleni, Giota, Paul, Dave, Nathan, Anna, Charbel, and Zhijin, and also of Dave Martin, Sean Ng, and Alastair Burls for their tremendous help.

Final, the author is grateful for the help and support of his parents, and of Maggie.

CONTENTS

NOMENCLATURE

SYMBOL	DESCRIPTION	UNIT
a	amplitude	[m]
b	plate thickness	[m]
c	chord length	[m]
C_M	momentum flux coefficient	-
C_P	power-input coefficient	-
C_T	thrust coefficient (defined on the freestream velocity)	-
$C_{T,VP}$	thrust coefficient (defined on the peak heave velocity)	-
E	modulus of elasticity	$[Nm^{-2}]$
f	frequency	$[s^{-1}]$
F	drive force	[N]
h	normalised amplitude (a_{LE}/c or a_{ROOT}/c)	-
K	thin plate bending stiffness ($Eb^3/12$)	-
k_G	Garrick frequency ($\pi fc/U_0$)	-
M	momentum flux per unit span	$[Nm^{-1}]$
Re	Reynolds number (U_0c/ν)	-
s	displacement	[m]
St	Strouhal number ($2fa/U_0 = 2k_Gh/\pi$)	-
t	time	[s]
T	thrust per unit span; period	$[Nm^{-1}]$; [s]
U	fluid velocity	$[ms^{-1}]$
U_0	freestream velocity	$[ms^{-1}]$
V	velocity magnitude	$[ms^{-1}]$
v	airfoil leading-edge velocity	$[ms^{-1}]$
v_P	peak airfoil leading-edge velocity ($a_{LE}\omega$)	$[ms^{-1}]$
x	streamwise position	[m]
y	cross-stream position	[m]
α	effective angle of attack ($\tan^{-1}(v/U_0) - \theta$)	deg.
α_0	peak effective angle of attack	deg.
η	propulsive efficiency (C_T/C_P)	-

λ	bending stiffness coefficient	-
λ_0	bending stiffness coefficient of b/c=0.56x10^{-3} plate	-
μ	Viscosity	[kgm^{-1}s^{-1}]
ν	kinematic viscosity (μ/ρ)	[m^{2}s^{-1}]
ε	thrust/power-input ratio	[N/W]
θ	pitch angle	deg.
θ_0	pitch amplitude	deg.
ρ	density	[kgm^{-3}]
φ	phase advance angle, spanwise flexibility	deg.
ϕ	phase advance angle, chordwise flexibility	deg.
ω	angular frequency ($2\pi f$)	[s^{-1}]
Ω	vorticity	[s^{-1}]

ABBREVIATIONS

LE	leading-edge
TE	trailing-edge
PIV	Particle Image Velocimetry
LDV	Laser Doppler Velocimetry
MAV	Micro Air Vehicle
ROOT	Wing root
TIP	Wing tip
MID	Wing mid-span
CSV	Comma Separated Variable

LIST OF FIGURES

OUTLINE OF THESIS

This thesis describes an experimental study of the effect of chordwise flexibility on the force and flow field characteristics of a two-dimensional airfoil in pure heave at low Reynolds numbers. The effect of spanwise flexibility is investigated in the final chapter of results.

Chapter 1 gives an introduction to flapping wing flight and the development of MAVs, summarises the key works of the last 100 years, and discusses the present state of the art. The predictions of computational models of oscillating airfoils are discussed. An interesting feature is seen to be how the force and efficiency characteristics relate to the pattern of flow over the airfoil. The Strouhal number and Reynolds numbers are seen to be key parameters. The review of the literature highlights the importance of flexibility in nature, but reveals that the subject of wing stiffness outside the realm of biology is relatively unexplored.

Chapter 2 describes the experimental apparatus and method. Details of the experimental setup for the Particle Image Velocimetry, Laser Doppler Velocimetry, flow visualisation, and force measurement methods are given.

Chapter 3 is the first chapter of results. The aim is to establish whether chordwise flexibility is beneficial for a two-dimensional airfoil in pure heave in still water. Force measurements, and studies of the flow field, show that flexibility is beneficial in terms of thrust. Significant benefits to efficiency are also suggested.

Chapter 4 explores the deflected jet phenomenon, where the vortex street from an oscillating airfoil is deflected away from the streamwise direction. Such deflected jets are observed for high Strouhal numbers, and hence arise when the freestream velocity is zero (infinite Strouhal number). PIV and LDV experiments in still water and air are described, and the observation of periodic switching is made. Although deflected jets, and even jet switching, have been observed before in the experimental and numerical literature, these observations appear to be the first of periodic switching. The chapter

concludes with a water tunnel study, in which the transition to higher freestream velocities, and hence lower Strouhal numbers, is investigated. Jet deflection effects are observed to diminish rapidly.

Chapter 5 extends the work of chapter 3, with the aim of establishing whether chordwise flexibility benefits extend to non-zero freestream velocities. Trends in propulsive force and efficiency are related to the flow pattern and shape characteristics of the airfoil. An analogy is made between a chordwise flexible airfoil in pure heave, which pitches passively, and a rigid airfoil in coupled heave and pitch. This approach introduces the parameters pitch amplitude and pitch phase angle, and allows for a comparison between data from the present experiment and data on rigid airfoils in coupled heave and pitch from the literature. The optimum pitch phase angles and Strouhal numbers are found to correlate with those in the literature. Chordwise flexibility is consequently suggested as an alternative, and mechanically simpler, way to achieve a coupled heave and pitch motion than traditional mechanical linkages.

The natural progression to spanwise flexibility is made in Chapter 6. Water tunnel experiments on a finite aspect ratio NACA0012 airfoil, flexible only in the spanwise direction, are described. The Strouhal number based on the amplitude of the mid-span is found to be a key parameter. Moderate efficiency benefits are observed with appropriate choice of flexibility.

Chapter 7 summarises the main conclusions of the four chapters of results. A list of publications is given in Chapter 8. References are given in Chapter 9.

1 INTRODUCTION

1.1 BACKGROUND

There is a wish to build miniature radio controlled aircraft known as Micro Air Vehicles (MAVs) for which numerous applications have been cited. One example is to relay video pictures from the source of a leak on an offshore oil rig. A second example is to relay sound and picture in "over the hill" reconnaissance situations. Some MAVs have already been constructed[1-3]. A super-capacitor powered ornithopter[1] of weight 6.5g is shown in Figure 1.1; a Lithium ion battery powered flapping wing aircraft of weight 14.4g is shown in Figure 1.2. The first aircraft has a pair of flexible flapping wings which provide lift and thrust. The second aircraft has a pair of wings which oscillate in heave (in a bellows arrangement) to provide thrust, and a fixed wing to provide lift. It is thought that it may be possible to approach the agility and endurance of birds and insects by adopting a flapping wing mechanism[4], and for this reason there is a need to understand the aerodynamics of oscillating airfoils. The key aerodynamic parameter is the Reynolds number[5]. Since the length scale of birds, insects and MAVs is of the order of the centimeter, the Reynolds number is very low, typically $Re=10^3$-10^5, and an understanding of the nature and relative importance of inviscid and viscous phenomena in this regime is sought.

The first scientific explanation of bird flight was given by Knoller[6] in "*The laws of wind resistance*" (1909). He described how the flapping motion of an airfoil would give rise to oscillatory lift and thrust forces. The work was repeated independently by Betz[7], and published shortly afterwards in 1912. In "*A paper to explain glider flight*", Betz described the potentially positive effect of air turbulence. Vertical

oscillations of the air flowing over a gliding bird's wing were shown to generate a force in the direction of flight, thereby reducing the drag. Wind tunnel experiments by Katzmayr[8] verified what is now known as the Knoller-Betz effect. In the manner of Betz, the wing in Katzmayr's experiment was stationary, and the oscillations were of the air. In 1936, Garrick[9] published a set of equations for the thrust and efficiency of a flat plate oscillating in inviscid flow. Pure heave, pure pitch, and coupled heave and pitch motions were modelled, although the equations were valid only in the limit of small amplitude oscillations. Other key inviscid studies were by Wu[10], Lighthill[11], and Chopra[12], the last of whom extended Garrick's theory to oscillations of arbitrary amplitude. An inviscid panel method was developed and applied by Jones et al.[13] to a heaving NACA0012 airfoil. A remarkable similarity was found between the flow patterns predicted by the panel method and those observed in experiments[13], illustrating how the formation of a reverse von Kármán street for an oscillating airfoil is essentially an inviscid phenomenon. Example figures are shown in Figure 1.3. These inviscid methods are valid in the case of high Reynolds number and small local (or *effective*) angles of attack. For the low Reynolds numbers of birds, insects, fish, and MAVs, flow separation tends to occur at the leading-edge[14], especially at high angles of attack. Inviscid methods are not capable of predicting such flow separation effects and, for this reason, Navier-Stokes codes have been developed. These methods are able to predict leading-edge flow separation, leading-edge vortex formation and shedding, and the consequent merger of the leading-edge vortices into the trailing-edge vortex system. An example thrust-indicative flow field is shown in Figure 1.4. The propulsive efficiency of oscillating airfoils has been shown to depend greatly on leading-edge flow separation effects. Navier-Stokes analyses by Isogai et al.[15], Tuncer and Platzer[16], Lewin and Haj-Hariri[17], and Tuncer and Kaya[18] show that efficiency is degraded by the formation of leading-edge vortices. For example, Tuncer and Platzer[16] observed the transition from weakly separated leading-edge flow to the shedding of large scale leading-edge vortices to correspond to a sharp decline in efficiency. The diminished efficiency was attributed to both a rise in power-input (due to the suction effect of the leading-edge vortex) and a fall in thrust (due to the disruption of the reverse vortex street caused by the arrival of the leading-edge vortex). Peak efficiencies are found to occur at angles of attack sufficiently small for such phenomenon to occur only very weakly. Example flow fields are shown in Figure 1.5 and Figure 1.6.

The airfoils in the majority of experimental studies have been rigid. Of these studies, the majority have been carried out at low Reynolds numbers, although a number have modelled hovering flight[19-21] (U_0=0). A number of experimental techniques have been used, including force balance measurements of thrust and efficiency[22], Particle Image[22] or Molecular Tagging Velocimetry[23] measurements of the velocity field, and dye[24] and smoke visualisation[25]. A variety of different oscillating motions have been investigated, including harmonic heave[13], harmonic pitch[26], coupled heave and pitch[22], and also alternative displacement waveforms to the Cosine wave (e.g. triangle waveform)[27]. Introducing a pitch motion to the heave of rigid airfoils has been found to yield potentially higher efficiencies. The mechanism has been found to be the diminishing of the leading-edge vortex[16, 28] through a lower effective angle of attack. The coupled heave and pitch motion is of interest in studies of nature, particularly in the thunniform swimming[29] of, for example, tuna, swordfish, and dolphins (see Figure 1.7). The approach taken in experimental studies has been to design a mechanical linkage to pitch the airfoil throughout the stroke[22, 27].

If we are to be guided by nature in the design of miniature aircraft, then it becomes necessary to study birds and insects in more detail. One question is of the stiffness of their wings. Studies of insect wings by Wootton[30] and Steppan[31] have revealed intricate variations in their stiffness. However, although areas of the wing have been identified as being specifically flexible[30], how this benefits the insect aerodynamically is still not clear[32]. Flexibility is an interesting subject in the design of MAVs, because in addition to any aerodynamic benefits it is noted that flexible wings are inherently light. The subject of flexibility in the arena of oscillating airfoils is relatively unexplored, however, despite the knowledge that it is of importance in bird and insect flight, and essential in fish swimming[33]. Numerical models have indicated higher efficiencies for flexible airfoils[34-36], though the computational complexity of the situation requires assumptions either of inviscid flow[34, 37] or of a pre-defined flexing motion[36, 38]. Experimentally, there are findings of higher thrust at zero freestream Reynolds number (the special case of hovering flight) [39, 40], and of higher efficiency at non-zero Reynolds numbers[41]. A systematic study of the effect of airfoil deformation on the flow field and force coefficients is absent from the

literature, however. The aim of the present study is to examine the flow-structure interaction, thrust, and efficiency of a flexible airfoil oscillating in heave at low Reynolds numbers.

1.2 SUMMARY OF PARAMETERS

1.2.1 PURE HEAVE

A rigid airfoil in pure heave is shown in Figure 1.8(a). The displacement of the leading-edge, s_{LE}, is given by $s_{LE}=aCos(\omega t)$. The velocity, v, is given by $v = -a\omega Sin(\omega t) = -v_p Sin(\omega t)$, where v_p is the peak heave velocity. The local, or *effective*, angle of attack, α, is given by $\alpha=\tan^{-1}(v/U_0)$.

The dimensionless heave amplitude may be defined as the ratio of heave amplitude to chord length, h=a/c. The amplitude is taken to be that of the leading-edge, although in some studies the parameter is based on the trailing-edge amplitude.

The *Garrick*, *Strouhal*, and *Reynolds* frequency parameters are found to be widespread in the literature. The Garrick frequency, $k_G=\pi fc/U_0$, when divided by π, is equal to the number of oscillations in the characteristic time c/U_0. The parameter is relevant when leading-edge vortices form and their streamwise separation is of interest. The Strouhal number, $St=2k_Gh/\pi=2fa/U_0$, is related to the peak effective angle of attack, $\tan(\alpha_0)=2\pi fa/U_0$. The parameter has been shown to be significant in the study of the wake pattern from a heaving airfoil[24], and in particular whether the wake pattern is characteristic of net drag or thrust[13]. It has also been found to have significance in nature, where the Strouhal numbers of insects, birds, bats, and fish are observed to lie within a narrow range[42] of $0.2<St<0.4$ (see Figure 1.9). In inviscid theory, the thrust coefficient of a heaving airfoil increases with St^2 for sufficiently high frequencies[43, 44]. For this reason the quantity 'C_T/St^2' is sometimes plotted[27], rather than 'C_T'. The Strouhal number in the present investigation is defined based on the heave amplitude 'a' and, although this definition is found throughout the literature[27, 28, 41], other definitions are possible. For example the parameter may be defined based on the chord length[45]. The third frequency parameter, the Reynolds frequency, $Re_f=fc^2/\nu$, (so named because of its resemblance

to a Reynolds number), is useful when the freestream velocity is zero[19, 46], in which case the Garrick and Strouhal parameters are undefined.

1.2.2 COUPLED HEAVE AND PITCH

A rigid airfoil in coupled heave and pitch is shown in Figure 1.8(b). The pitch angle, θ, is given by $\theta=\theta_0 Cos(\omega t+\phi)$, where θ_0 is the pitch amplitude and ϕ is the phase angle by which the pitch *leads* the heave. The effective angle of attack is given by:

$$\alpha=\tan^{-1}(v/U_0) - \theta. \quad (1.1)$$

The pitch phase angle is often chosen to be in the region of 90 degrees, since the airfoil then tends to be aligned to the local flow, thus reducing the effective angles of attack.

1.2.3 CHORDWISE BENDING STIFFNESS

The bending stiffness parameter, 'λ', is defined following the approach of Murray[37] as:

$$\lambda = \frac{K}{\frac{1}{2}\rho U_0^2 c^3}, \quad (1.2)$$

where, 'K', the bending stiffness of a thin plate, is given by:

$$K = \frac{Eb^3}{12}, \quad (1.3)$$

where, 'E' is the modulus of elasticity, and 'b' is the thickness of the plate.

1.3 EXPERIMENTAL STUDIES

Experimental studies on oscillating airfoils at low Reynolds numbers have focused on the effect of heave amplitude, heave frequency, pitch amplitude and pitch phase angle on the flow field and thrust and lift forces. Traditionally, the flow pattern has been photographed with smoke flow visualisation techniques[19, 25]. Point velocity

measurements were made with LDV apparatus[26]. More recently, PIV apparatus has been used to obtain a more complete picture of the flow field[22]. Measurements of the thrust and lift forces, from which propulsive efficiencies have been derived, have been made with force balances. One of the primary aims of experimental research has been to relate changes in the flow pattern to trends in thrust and efficiency, and in particular to find the optimum conditions for propulsion.

Investigations of both the two-dimensional and three-dimensional cases have been carried out. Studies of the two-dimensional case involve a relatively high aspect ratio wing confined to oscillate between splitter plates. In some cases, end-plates are attached to the tips of the wing. The purpose of such plates is to diminish three-dimensional effects such as spanwise flow. These effects were investigated by Koochesfahani[26] for an airfoil oscillating in pitch between splitter plates. Three dimensional effects were observed near the splitter plates, where the vortices appeared as cones (*viz.* delta wing vortex), rather than cylinders, suggesting the presence of spanwise flow.

Studies of the three-dimensional case involve a relatively low aspect-ratio wing, often confined to oscillate with the root near a single end plate. In this way the experiment simulates a single wing of a bird or insect. Moving to three dimensions introduces a vast number of parameters (aspect ratio, wing planform shape, angles of axes of motion for example), and for this reason three-dimensional experimental studies have often been related to a particular species of bird or insect. For example, Van Den Berg and Ellington[47] constructed a model of a Hawkmoth, in an attempt to discover the mechanisms by which the insect generates lift and thrust. While it is certainly important to consider the three dimensional case when considering natural flight, there are a great many aspects to consider in the relatively simple two dimensional case. These will now be discussed.

1.3.1 ZERO FREESTREAM VELOCITY

As is evident from the hovering of birds and insects, it is possible for an airfoil oscillating in still air to generate thrust. Freymuth[19] showed, through a set of smoke flow visualisation experiments, that it is possible to create thrust in still air with a two-

dimensional airfoil oscillating in coupled heave and pitch. Estimates of the thrust were made from measurements of the velocity of the jet (obtained with a pitot tube). Thrust coefficient was found to be a function of heave amplitude, pitch amplitude and pitch phase angle. The airfoil in the experiment was a flat plate, showing that neither a camber nor thickness is required for thrust generation. Later, Lai and Platzer[21] carried out a set of experiments on a NACA0012 airfoil in pure heave in still water. The time-averaged velocity profile downstream of the trailing-edge was measured with LDV apparatus. The velocity measurements revealed a jet, showing that a pure heave motion is sufficient for a NACA0012 airfoil to generate thrust. The experiment was repeated with a cylindrical airfoil and, as expected, a jet was not created. The results of these two experiments suggested that, for a two-dimensional airfoil to experience thrust when oscillating in still fluid, the airfoil must either be oscillated in coupled heave and pitch, or, if oscillated in pure heave, must have an asymmetric cross section (i.e. must not be a flat plate, ellipse or cylinder for example). Recent experiments by Vandenberghe et al.[47] suggest otherwise, however. A flat plate oscillating in pure heave was found to accelerate, and therefore to experience a thrust force, when the heave frequency exceeded a critical value. The phenomenon was attributed to the formation of asymmetric vortices during the oscillation cycle. As the plate accelerated, a vortex structure resembling a reverse von Kármán street was observed (Figure 1.10).

1.3.2 NON-ZERO FREESTREAM VELOCITY

At non-zero freestream velocity, airfoils in pure heave are found to experience net thrust when oscillated above a critical frequency[24]. Lai and Platzer[24] studied the transition with dye flow visualisation in a water tunnel. Example photographs of the wakes are shown in Figure 1.11. At very low heave frequencies the airfoil behaves in a similar manner to a stationary airfoil; a von Kármán street is observed downstream of the trailing-edge, the net velocity profile shows a velocity deficit, and the airfoil experiences drag. At slightly higher heave frequencies, vortices from the oscillation of the airfoil are observed to mix with the "drag" vortices; a complex multiple-vortex wake pattern is observed. As the frequency increases further the velocity profile downstream becomes neutral; the airfoil experiences neither thrust nor drag. As the oscillation frequency increases further the "thrust" vortices begin to dominate, and a

reverse von Kármán street is observed, where the sense of rotation of the vortices is opposite to a conventional von Kármán street. The time-averaged velocity downstream of the trailing-edge has a jet profile.

1.3.3 DEFLECTED JETS AND JET SWITCHING

It has been seen above (flat sheet oscillating in still water) that an apparently symmetrical oscillating airfoil arrangement can lead to an asymmetric flow pattern. A further example of this is the *deflected* jet. The change in nature of the vortex wake pattern with increasing Strouhal number for a NACA0012 airfoil in pure heave at low Reynolds numbers has been described above. Lai and Platzer[24] observed one further change at higher still Strouhal numbers. It was that the direction of the jet was deflected away from the freestream direction. Such a deflected jet is shown in Figure 1.3(b). Although the initial direction of the jet was found to depend on the starting position of the airfoil, the direction thereon was found to switch randomly from one side to the other. Deflected jets have also been observed for zero freestream velocity[21], the case of infinite Strouhal number. Such experimental findings of deflected jets were first reported by Bratt[48] in 1953, though have received little attention since. Jones et al.[13] found them to occur for Strouhal numbers greater than approximately 0.35, for a NACA0012 airfoil in pure heave. Again, the jet was observed to switch randomly.

1.3.4 EFFICIENT FLAPPING MOTIONS

Although the pure heave motion has been shown to produce thrust in both zero and non-zero freestream situations, experimental studies have found it to be an inefficient form of propulsion. For example, Schouveiler et al.[49] measured a peak efficiency of approximately 33% for a NACA0012 airfoil in pure heave (Re=40,000, h=0.75), compared with over 70% for coupled heave and pitch. An extensive study of the efficiency of oscillating airfoils was carried out by Anderson et al.[22]. Experiments were carried out in a water tunnel with a NACA0012 airfoil (Re=40,000). High efficiencies were observed for effective angles of attack of 15-25 degrees, phase angles of 75-90 degrees, and Strouhal numbers of 0.15-0.4. Hover et al.[27] performed a similar study with a NACA0014 airfoil (Re=30,000). High efficiencies were observed for effective angles of attack of 10 degrees, phase angles of 90 degrees,

and Strouhal numbers of 0.25. Both studies found efficiency to decay rapidly to zero at low Strouhal numbers (due to the transition from thrust to drag), and to fall again at high Strouhal numbers. The origin of these trends has been considered in numerical and computational studies of oscillating airfoils. The effects of leading-edge flow separation, and the proximity of trailing-edge vortices to the airfoil, are found to be of importance.

In the coupled heave and pitch experiments described above, the heave and pitch motions both followed the form Cos(ωt). The effect of adjustments to this type of motion were investigated experimentally by Hover et al.[27]. Enhancements in efficiency and/or thrust were found to be possible by manipulating the effective angle of attack profile. The harmonic motion was found to yield the highest efficiency, and a sawtooth angle of attack profile to yield the highest thrust coefficient. Changes in the angle of attack profile were observed to cause changes in the wake pattern, with either a pair of vortices being shed per stroke (cosine angle of attack profile) or multiple vortices per stroke (cosine angle of attack with higher harmonics added).

1.4 THEORETICAL AND NUMERICAL METHODS

Theoretical and numerical models of flapping wings have been developed for two reasons. The primary reason has been to improve the understanding of the fluid dynamics of the situation – to discover the importance of viscous effects, for example. The secondary reason has been to assist the design of *ornithopters*, aircraft with flapping wings[43]. One example is the bi-plane MAV of Jones et al. (Figure 1.2), where two rectangular planform airfoils oscillate in heave in a "bellows" arrangement. A panel method predicted that such an arrangement would benefit both thrust and efficiency.

The thrust, efficiency and flow pattern predictions of the theoretical, numerical, and computational methods may be compared with corresponding experimental data. Where appropriate experimental data is missing from the literature, it is possible only to compare the methods with each other. This has been necessary in, for example, studies of the flow pattern near the leading-edge, where experimental data is rare, except in cases of high Reynolds number and moderately high Mach number[50]. The

absence of such experimental data may be related to the difficulty in photographing, or capturing with PIV, the flow pattern near the surface of the airfoil.

1.4.1 LINEAR THEORY

The theory of Garrick[9], also known as *linear* theory, has been returned to many times since its publication in 1936. Garrick's theory followed from Theodorsen's[51] theory of flutter, given in 1935. Garrick theory models a thin flat plate oscillating with small amplitude. The theory is two-dimensional, inviscid, and incompressible, and so aspect ratio, Reynolds number, and Mach number do not feature. Linear theory predicts the time-averaged thrust and efficiency of the wing, valid in the limit of small amplitude. Equations are given for pure heave, pure pitch, and coupled heave and pitch.

According to Garrick, thrust and efficiency of a flat plate in pure heave (valid in the limit of small amplitude oscillations) are given by:

$$C_T = \pi^3 St^2 (F^2 + G^2), \tag{1.4}$$

$$\eta = \frac{F^2 + G^2}{F}, \tag{1.5}$$

where, $F(k_G)$ and $G(k_G)$ are the real and imaginary parts of the Theodorsen lift deficiency function. The values in the limits of low and high frequency are F(0)=1, G(0)=0, $F(k_G \to \infty)=½$, $G(k_G \to \infty)=0$.

Thrust coefficient and efficiency are plotted as a function of k_G in Figure 1.12(a) and Figure 1.12(b) respectively for $k_G h=0.3$ (St=0.19). It is seen from the two equations that efficiency is independent of heave amplitude, and depends only on the frequency, k_G. The efficiency tends to a value of one in the low frequency limit, and to a value of one-half in the high frequency limit. For high frequencies, the thrust coefficient tends to a value of $\pi^3 St^2/4$. The thrust coefficient tends to a value of zero in the low frequency limit (amplitude constant). This is contrary to experimental measurements[52], which find airfoils to experience drag in this limit. In the low

frequency regime there is therefore disagreement between linear theory and experiment. The disagreement is most marked in the case of efficiency, where the theoretical value tends to a maximum of unity in the low frequency limit, whereas experimental measurements yield negative values.

Linear theory also models coupled heave and pitch, which brings two additional variables: pitch amplitude and pitch phase. The effect of introducing a pitch motion is shown in Figure 1.13. Thrust coefficient and efficiency are shown for the complete range of pitch phase angles. The horizontal lines indicate the thrust and efficiency for the pure heave case. It is seen that introducing a pitch motion increases efficiency for pitch phase angles of between 60 and 150 degrees, though at the expense of a lower thrust coefficient. It is also seen that for phase angles in the region of 270 degrees, thrust coefficient is greater than for the pure heave case, though at the cost of lower efficiency. It is seen that it is not possible to simultaneously increase both thrust coefficient and efficiency. For pitch phase angles in the region of 90 degrees, the lower thrust coefficient may be attributed to lower effective angles of attack (the phase of the pitch motion is such that the airfoil tends to align itself to the flow). Similarly, the higher thrust coefficient for phase angles in the region of 270 degrees may be attributed to the higher effective angles of attack. Returning to the 90 degree case, Jones et al.[43] show a special situation to arise when the pitch amplitude reaches a critical value. It is for the chord of the airfoil to be aligned to the local flow throughout the stroke, and for the effective angle of attack to be zero. In this condition the airfoil experiences zero net force at each instant in time. If the pitch amplitude is increased further then the airfoil experiences angles of attack of opposite sign to those in the conventional thrust configuration. The thrust coefficient becomes negative and energy is extracted from the flow (work is done *on* the driving mechanism). This effect has been applied as a way of generating electricity on a large scale[53].

In order to assess the impact of the restrictions of linear theory (attached flow, small heave amplitude, thin airfoil, inviscid flow), two further numerical models are discussed – the panel method and Navier-Stokes solver – with reference to experimental data from the literature.

1.4.2 PANEL METHOD

The panel method[54, 55] has been applied to oscillating airfoils[13, 56]. As for Garrick theory, since the flow is incompressible, and inviscid, the Mach and Reynolds numbers do not feature. The panel method follows a potential flow approach, in which a thick airfoil is constructed from a number of panels, each with a point source and sheet of vorticity. The Kutta condition is enforced at the trailing-edge. At each time step, the changing relative velocity of the oncoming flow, and velocity induced by the vortices in the wake, changes, and the strengths of the sources and sinks are adjusted in order to satisfy the boundary conditions. The sum of the vorticity of the panels of the wing generally changes from each time step to the next, and, in order to satisfy Kelvin's circulation theorem, a vortex is shed into the wake from the trailing-edge in order that the sum of vorticity over the wing and in the wake is constant. The panel method is able to model airfoils with finite aspect ratio and thickness, oscillating with large amplitude. Furthermore, it is able to model the wake in such a way that the vortices influence each other. This *deforming* wake yields induced velocities in the vicinity of the airfoil that augment the force coefficients[43].

A significant feature of the code is the ability to visualise the wake – to see the formation of vortices at the trailing-edge, and their evolution with time. The vortices may be revealed by symbols showing the location of vortices shed into the wake, by contours of vorticity, or by the computational equivalent of the experimental method of dye flow visualisation, where a stream of particles is released into the flow near the trailing-edge. Since the panel code does not model viscous effects, it can not predict the von Kármán vortex street that trails from bluff bodies. It is only able to predict the reverse von Kármán street (vortices in the same positions but rotating in opposite directions), that has a time-averaged jet profile. The method is therefore not suitable for predicting the flow pattern for drag, or near zero-net-thrust cases. However, it is often the positive thrust case that is of interest, and here the method is able to predict the shape of the flow pattern successfully, even in cases where the jet is deflected. Example wake vortex patterns are shown in Figure 1.3. Figure 1.3(a) shows the reverse von Kármán street for a NACA0012 airfoil in pure heave found experimentally, and as predicted by the panel code. Figure 1.3(b) shows a higher Strouhal number case, where the experimental wake is observed to lie at an angle to

the freestream. The panel code wake is seen to closely resemble the experimental wake pattern. These observations led to the assertion[13] that the creation of thrust via a reverse vortex street is essentially an inviscid phenomenon.

The thrust and efficiency predictions of the panel method are plotted in Figure 1.12(a) and Figure 1.12(b) respectively, for constant Strouhal number. It is seen from the figure that the thrust characteristics of the panel method are similar to those of Garrick theory, but that the panel method predicts lower efficiency, significantly so at high frequency. Jones et al.[43] found that when the wake in the panel method was confined to a horizontal plane, and suppressed from evolving, the method found agreement with linear theory. In this way, Jones et al.[43] showed that it is the absence of a wake evolution model in Garrick theory, rather than the thin airfoil or small amplitude assumptions, that is responsible for the discrepancy between Garrick theory and the panel method. The "roll up" of the wake near the trailing-edge was found to augment the lift force, causing a rise in power-input coefficient and decrease in efficiency. The severity of the effect was found to increase with frequency.

The thrust and efficiency predictions of the panel method for a coupled heave and pitch motion are shown in Figure 1.13. Close agreement is observed in the trends in thrust and efficiency between the panel method and linear theory.

1.4.3 NAVIER-STOKES METHOD

A third approach is to find numerical solutions of the Navier-Stokes equations. Although this method allows viscous effects to be modelled, it has only become popular recently because of the availability of sufficiently powerful computers. The ability to model viscous effects introduces the Reynolds number as a parameter, and allows the prediction of boundary layer separation and the related phenomena of leading-edge vortex formation and shedding. Although the majority of Navier-Stokes codes in the literature solve the incompressible form of the equation, some solve the compressible form, in which case density becomes an additional parameter. A consideration for compressible codes is that the Mach number for birds, insects and MAVs is very low, typically 1/300 [45]. One of the disadvantages of the Navier-Stokes approach is that the computational effort is considerably greater than that

needed for the panel method. As for the panel method, Navier-Stokes codes are able to predict the flow pattern, although in greater detail, particularly upstream of the trailing-edge. A turbulence model may be incorporated[57]. However, for the low Reynolds number flows in nature, closer agreement is observed between the predicted flow patterns and those found experimentally without turbulence models[44], suggesting that the boundary layers observed in experiments were laminar. The wake pattern, thrust and efficiency predictions will now be discussed.

Wake Pattern

An example vortex wake pattern predicted by the Navier-Stokes simulation of Young and Lai[44] is shown in Figure 1.4 for a NACA0012 airfoil in pure heave. The figure illustrates the ability of the method to model leading-edge flow separation and the formation and shedding of leading-edge vortices. A second example wake pattern is shown in Figure 1.14. In this case the Strouhal number is sufficiently low for the airfoil to experience drag. A complex four-vortices-per-cycle pattern is observed experimentally, and this is reproduced successfully by the Navier-Stokes simulations. Young and Lai[44] conject that the four vortices per cycle are composed of two vortices due to the oscillation of the airfoil, and which contribute to thrust, and two from the drag profile of the airfoil – the remnant of the static case von Kármán street. As the oscillation frequency/amplitude increases, the vortices coalesce, and the reverse von Kármán street dominates. The difficulty in this explanation is that the vortex shedding frequency of the "thrust" vortices is equal to the oscillation frequency of the airfoil, while the shedding frequency of vortices from a stationary airfoil is constant. Young and Lai argue that the natural vortex shedding frequency changes when the airfoil starts to oscillate, because separated flow regions in the near vicinity of the trailing-edge cause the edge to be effectively blunt (Hannemann and Oertel[58] showed that the natural vortex shedding frequency of a flat plate with a blunt trailing-edge depends on the finish of the edge). Young and Lai believe a type of phase locking between the frequency of the drag and thrust vortices is therefore possible. A third vortex pattern is shown in Figure 1.15, for a case of high Strouhal number. A reverse von Kármán street is observed, in close agreement with the experimental wake pattern.

Thrust Coefficient – Pure Heave

The thrust coefficient predictions of the Navier-Stokes method of Young[56] are shown in Figure 1.12(a). Agreement is observed with the inviscid methods for high frequencies only. The low frequency trend is reproduced in the similar studies of Wang[45] and Lewin[17]. Lewin[17] observed qualitatively different vortex shedding patterns at low and high frequencies. At low frequencies, strong leading-edge vortices were observed, which shed into the wake and convected downstream. Depending on the frequency of the oscillation, the leading-edge vortices would merge with either same sign (Figure 1.16(i)) or opposite sign (Figure 1.16(ii)) vorticity at the trailing-edge. Meeting with vorticity of the same sign preserved to a degree the pattern of vorticity from the trailing-edge. Meeting with fluid rotating in the opposite direction tended to give rise to a weak jet. (The thrust coefficient in this case incurred an additional penalty.) As the frequency increased, the separation of the vortices shortened, and an apparent interaction with the airfoil caused their strength to diminish (Figure 1.16(iii)). In these cases, where the leading-edge vortices dissipated before reaching the trailing-edge, the thrust coefficient was found to be greater. For higher frequencies still, the vortices, rather than flowing downstream, tended to be swept over the leading-edge, mixing and dissipating rapidly (Figure 1.16(iv)). Wang[45] also found the shedding of leading-edge vortices to be detrimental to thrust. Wang investigated the time history of the forces for the shedding of a leading-edge vortex, and found the formation of a *bound* leading-edge vortex to give rise to a low pressure region near the leading-edge, which contributed to the thrust force. However, once this vortex lifted off the surface and began to flow downstream (i.e. once it *separated*), the low pressure region was located near the trailing-edge, where it contributed to drag. Also, the leading-edge vortices were found to interfere destructively with vortices from the trailing-edge, resulting in a weaker jet.

Thrust Coefficient - Coupled Heave and Pitch

One of the predictions of Garrick theory (and also of the panel method) is that the thrust coefficient for a coupled motion, with a pitch phase advance of 90 degrees, is lower than for a pure heave motion (see Figure 1.13). The prediction is what might be expected from a consideration of the effective angles of attack: stronger trailing-edge vortices are likely when the effective angles of attack are large, hence a stronger jet and greater thrust for a pure heave. A pitching airfoil tends to align itself to the

incident flow (*feathering*), thus generating weaker vortices. It is interesting to discover if Navier-Stokes approaches yield the same predictions. The most pertinent data is provided by Pedro[28]. Contrary to the predictions of linear theory, Pedro showed that for a NACA0012 airfoil and pitch phase angle of 90 degrees, thrust coefficient *increases* as the pitch amplitude is increased, from C_T=0.4 at 5deg, to a maximum of C_T=1.0 for a pitch amplitude of 30 degrees. Over this range the effective angle of attack fell from 55 degrees to 25 degrees. Flow visualisation images showed a significant decrease in the magnitude of the leading-edge vortices over this range. For the high angle of attack (pure heave) case, the leading-edge vortices were clearly visible in the wake, whereas for the coupled motion the vortices were not visible in the wake.

Efficiency

The efficiency predictions of the Navier-Stokes method of Young[56] are shown in Figure 1.12(b). Lower efficiency is observed relative to the panel method and linear theory. Navier-Stokes analyses by Isogai et al.[15], Tuncer and Platzer[16], Lewin and Haj-Hariri[17], and Tuncer and Kaya[18] show that efficiency is degraded by the formation of leading-edge vortices. One question when low efficiencies are observed is whether the origin is a low power output (thrust) or high power input. Tuncer and Platzer[16] observed a transition from weakly separated flow to the shedding of large scale vortices to correspond to a rise in power-input, caused by the suction effect of the leading-edge vortex, and a fall in thrust, due to the disruption of the reverse vortex street caused by the arrival of the leading-edge vortex. A corresponding sharp fall in efficiency was observed.

It is noted that although the trend in efficiency is to fall with increasing frequency for linear theory, the panel method, and Navier-Stokes codes, the mechanism responsible for the fall is different. For the panel method, the roll up of the wake near the trailing-edge causes a rapid increase in the power requirement, and hence steeper decline in efficiency than Garrick theory predicts. In the Navier-Stokes method, the formation of leading-edge vortices is responsible for an additional increase in power-input, and a moderate decrease in thrust.

Deflected Jets

As mentioned above, experimental studies of heaving airfoils have found the vortex jet to lie at an angle to the freestream direction when the Strouhal number is sufficiently high. The panel method has predicted deflected jets, the pattern of which resembles closely the pattern found experimentally. However, whereas the direction of the jet has been found experimentally to switch randomly, the panel method prediction is for the direction to be fixed. Navier-Stokes simulations predict deflected jets for both pure heave and pure pitch oscillations. An example of the transition from reverse von Kármán street to deflected jet is shown in Figure 1.17 for a flat plate in pure pitch. The jet becomes deflected when the Strouhal number exceeds a value of approximately 0.35 [13]. The Navier-Stokes simulation of a NACA0012 airfoil in pure heave by Lewin and Haj-Hariri[17] was the first to predict the *jet switching* phenomenon. The wake at two times in the simulation is shown in Figure 1.18. The periodicity of the switching is not discussed. Other Navier-Stokes simulations have observed deflected jets, though not jet switching. It is noted that the number of cycles through which the simulations may be run is of the order of 10.

Spanwise flexibility

Spanwise flexibility is of interest because the wings of birds and the fins of fish and aquatic mammals are flexible along the span. One question is whether spanwise flexibility is beneficial to natural flight, or whether it is a limitation, due to the finite stiffness of the bone structure of the wing. Liu & Bose[59] studied the effect of spanwise flexibility on the flukes of an immature fin whale. The phase of the flexing motion relative to the heave was found to be a key parameter in determining the thrust and efficiency characteristics of the fin. In-phase motions yielded a benefit in efficiency and a significant increase in thrust. Out of phase motions were found to be detrimental. The subject of spanwise flexibility is particularly relevant to the design of flapping-wing MAVs, for which weight is a key restraint: light wings are inherently flexible.

1.5 OBJECTIVES

The four objectives of the present investigation are to i) establish whether chordwise flexibility is beneficial for an airfoil oscillating in pure heave at zero freestream velocity (zero freestream Reynolds number); ii) investigate the jet switching

phenomenon at zero freestream velocity, with emphasis on the frequency of the switching; iii) establish whether benefits to flexibility exist for freestream velocities greater than zero (low Reynolds numbers), and to relate the propulsive force and efficiency to the shape characteristics of the airfoil and the observed flow pattern; iv) to discover whether spanwise flexibility may be beneficial.

1.6 FIGURES

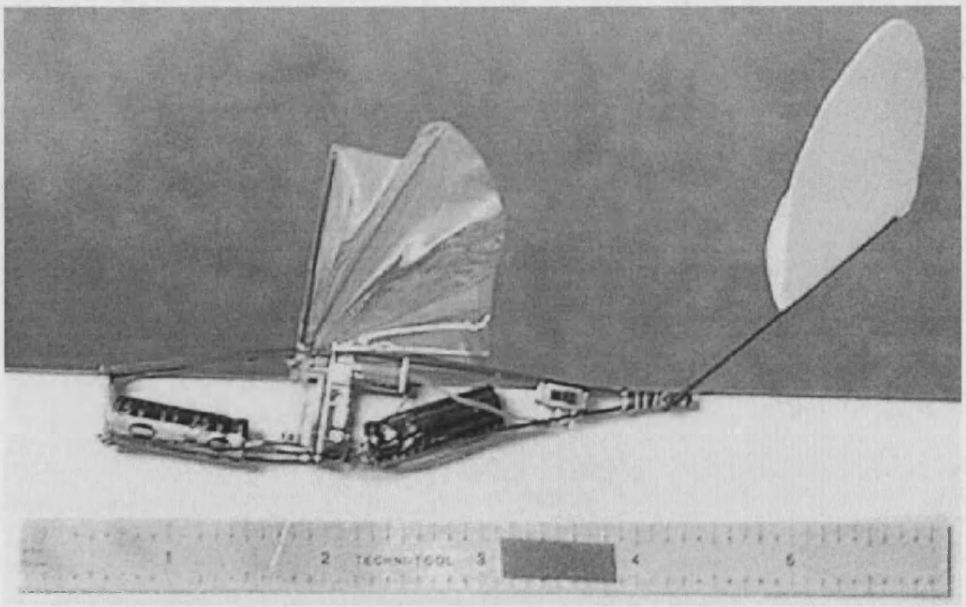

Figure 1.1: A super-capacitor powered flapping wing MAV[1].

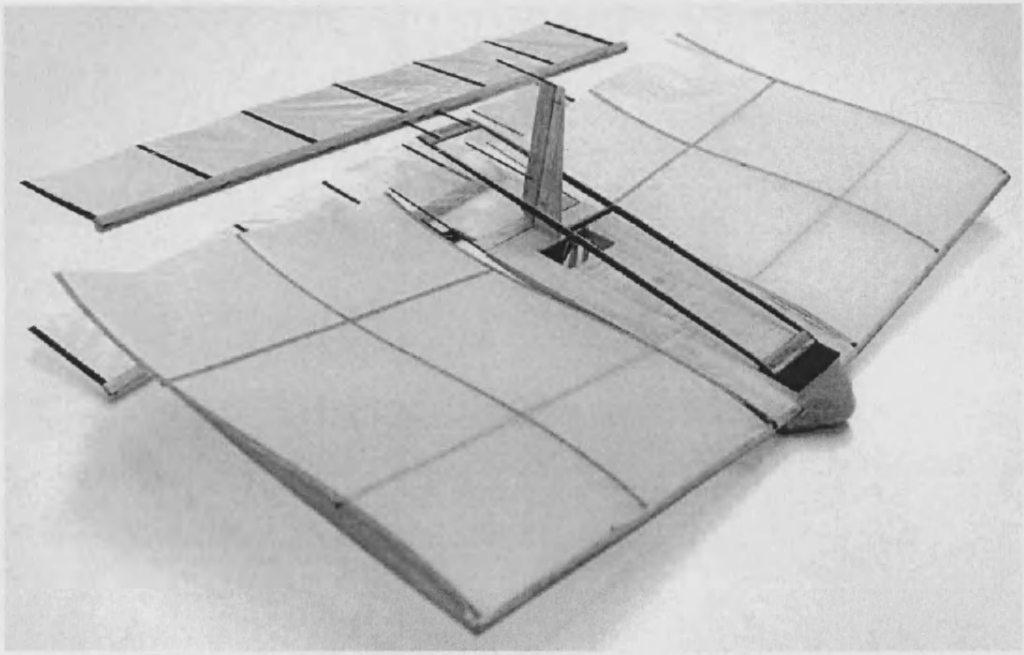

Figure 1.2: A Li-ion battery powered flapping-wing "biplane" MAV[40].

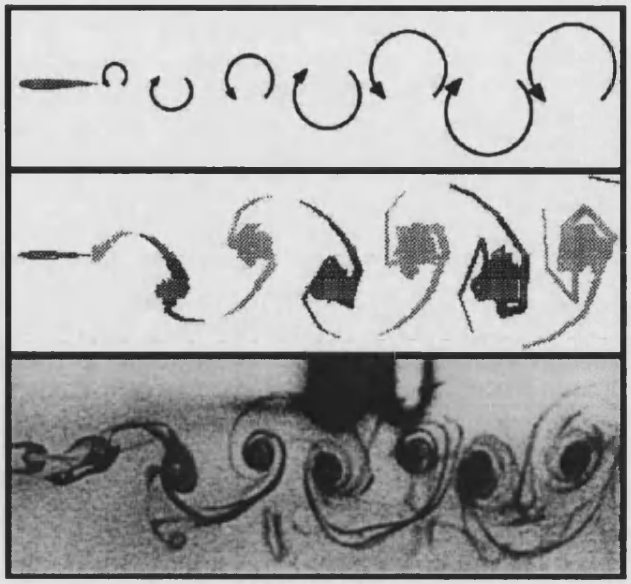

(a)

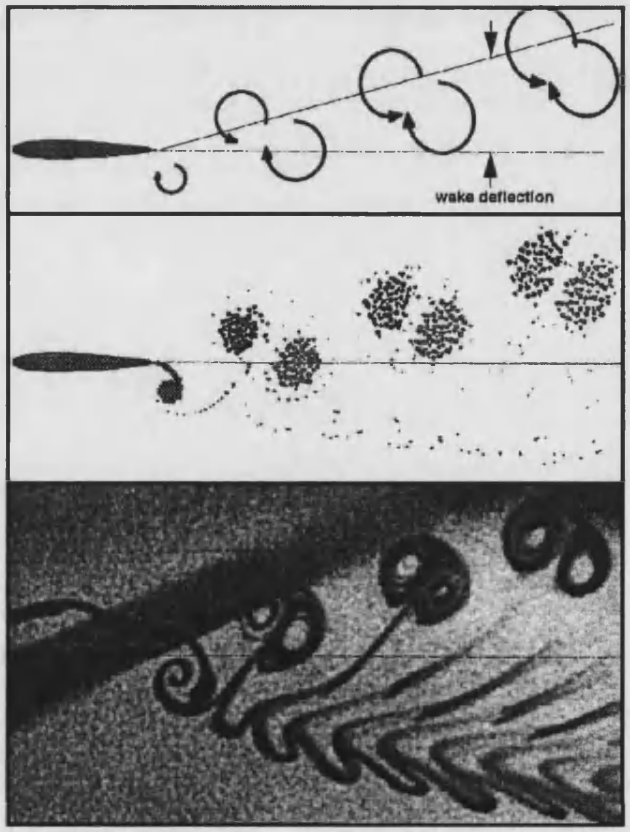

(b)

Figure 1.3: Comparison of panel code and experimental trailing-edge flow patterns. (a) Vortex street indicative of thrust production (St=0.19); (b) Vortex street indicative of thrust and lift (St=0.47); NACA0012 airfoil, pure heave, Reynolds number of order 10^4 [13].

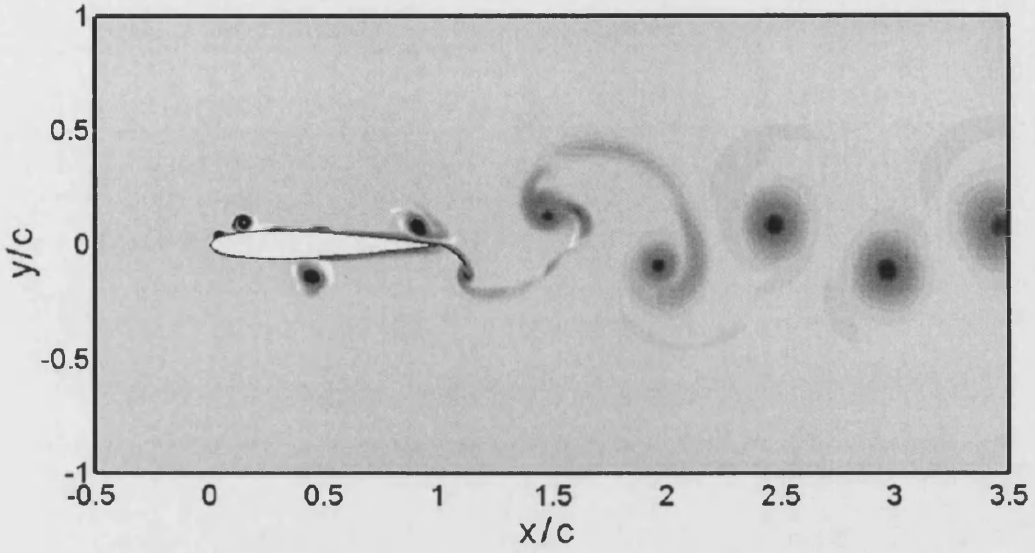

Figure 1.4: Navier-Stokes flow pattern showing leading-edge flow separation and vortex formation; NACA0012 airfoil, pure heave, St=0.19, $Re=2x10^4$ [44].

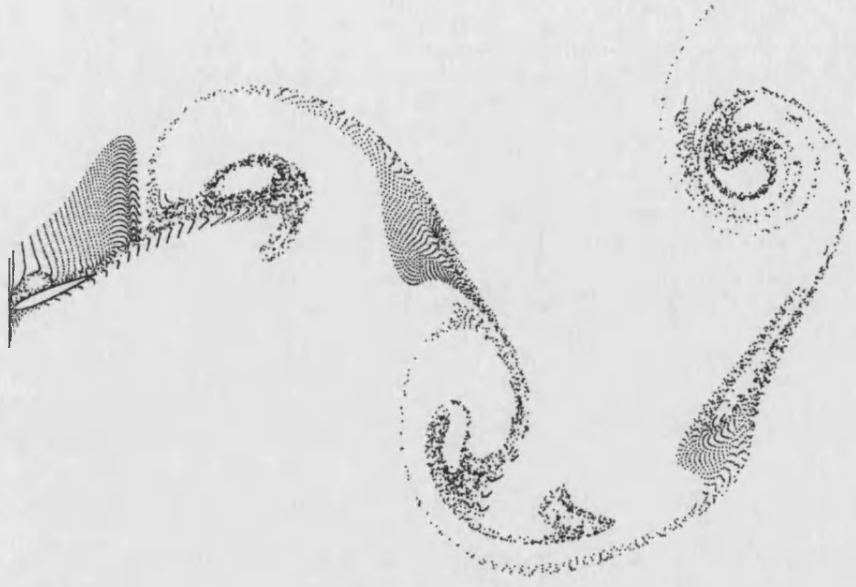

(a)

(b)

Figure 1.5: Navier-Stokes particle traces for coupled heave and pitch motions found to maximise (a) thrust coefficient and (b) efficiency; NACA0012 airfoil, $Re=1x10^4$ [18].

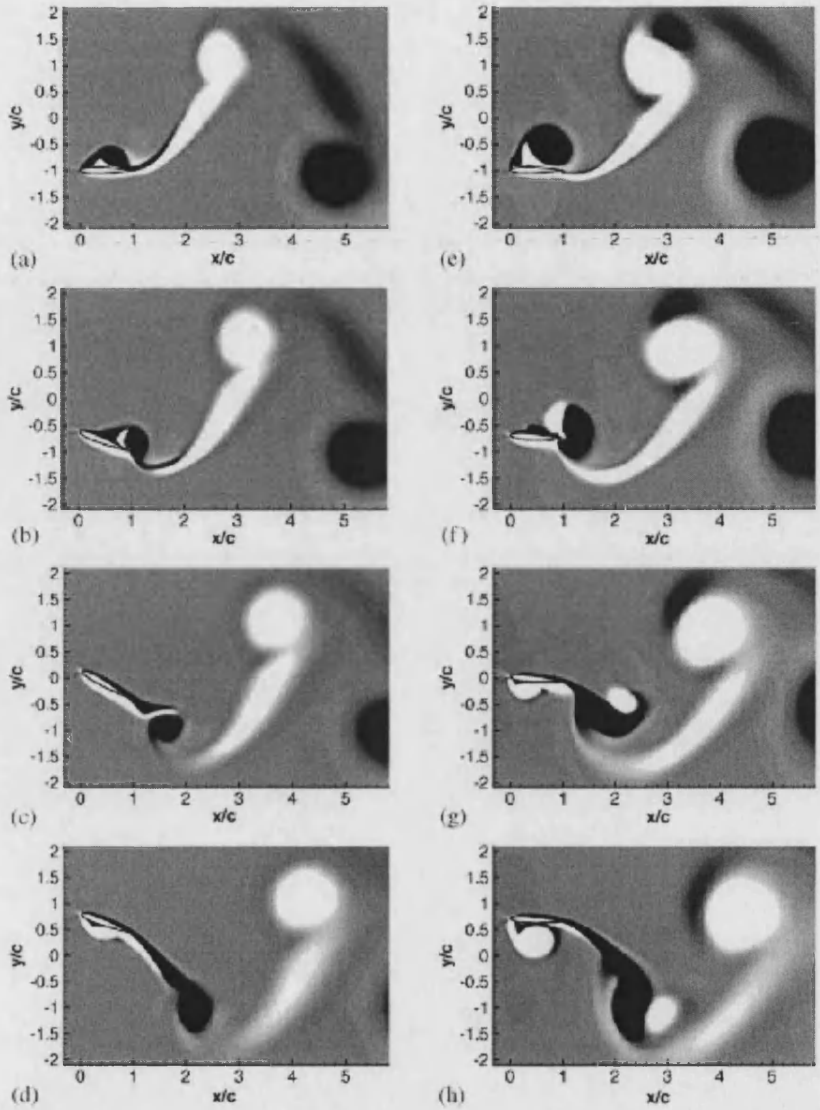

Figure 1.6: Navier-Stokes vorticity contour plots showing the upstroke of an airfoil in coupled heave and pitch with (a-d) 30 deg. pitch amplitude, 25 deg. angle of attack amplitude; (e-h) 5 deg. pitch amplitude, 50 deg. angle of attack amplitude. The second column is near to a pure heave motion, strong leading-edge vortices are observed and the efficiency is correspondingly low (9%). Weaker leading-edge vortices are observed in case (a-d), and the efficiency relatively high (42%). NACA0012 airfoil, $Re=1.1x10^3$ [28].

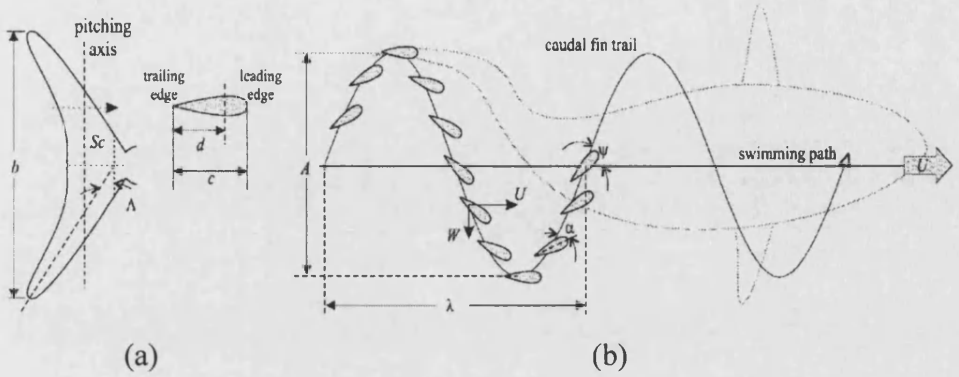

Figure 1.7: (a) Lateral view of caudal fin shape for thunniform swimmers; (b) Trail of an oscillating caudal fin[29].

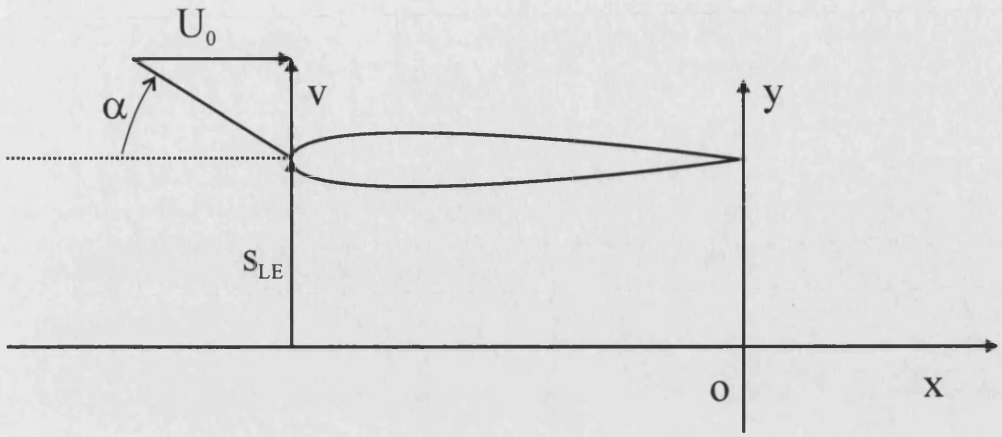

(a)

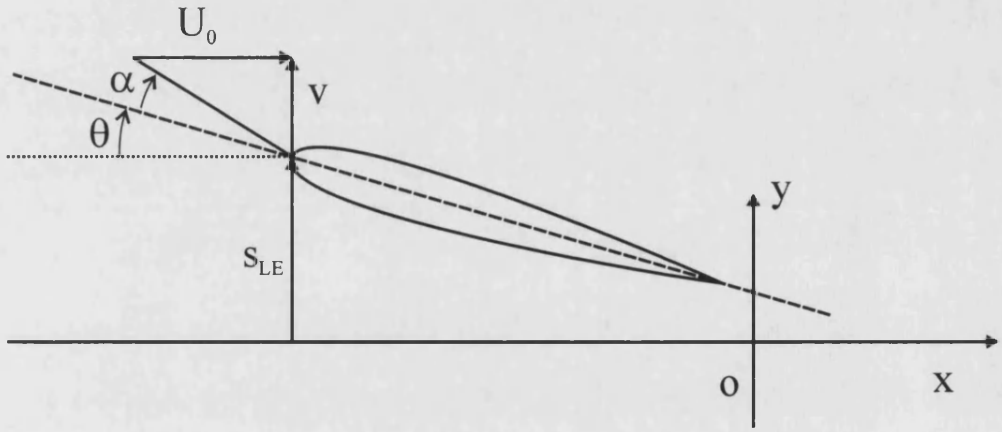

(b)

Figure 1.8: Schematic diagram of a rigid airfoil in (a) Pure heave, (b) Coupled heave and pitch.

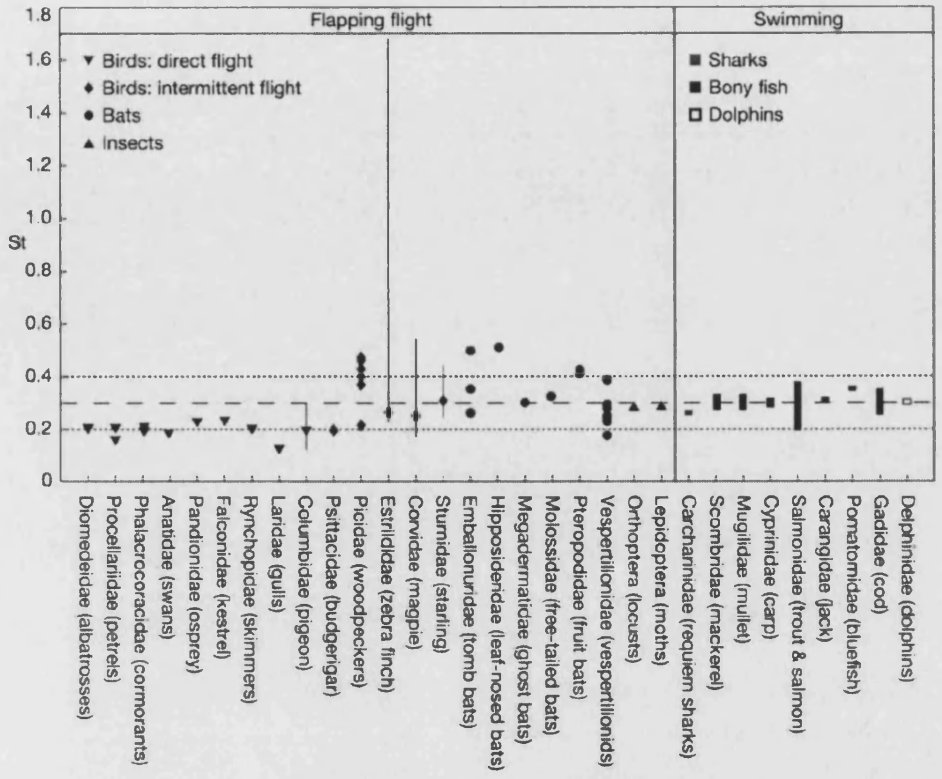

Figure 1.9: Strouhal numbers of birds, bats, insects, fish and dolphins in cruise[42].

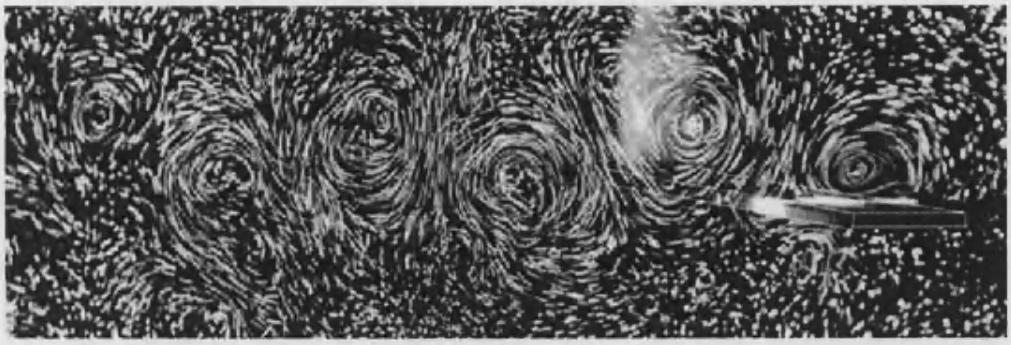

Figure 1.10: Flow visualisation for a flat plate in pure heave, initially oscillating in heave in still water[46].

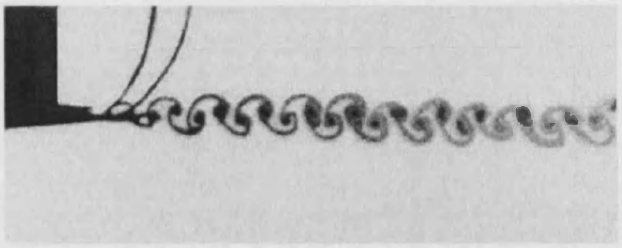

Stationary NACA0012 airfoil

h=0.0125, $k_o h$=0.05

h=0.0125, $k_o h$=0.1

h=0.0125, $k_o h$=0.2

Figure 1.11: Flow visualisation showing the transition from von Kármán street to reverse von Kármán street with increasing Strouhal number[24].

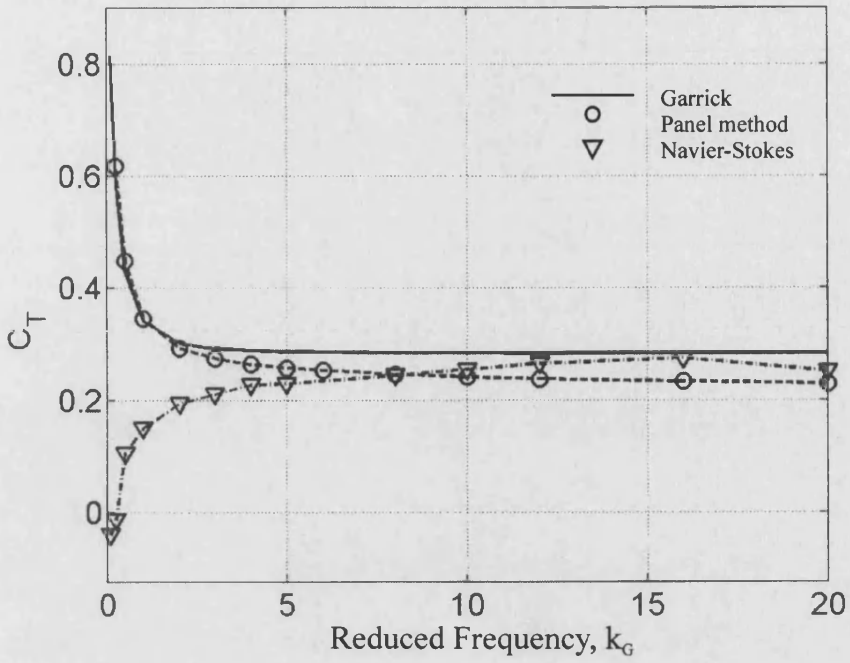

(a)

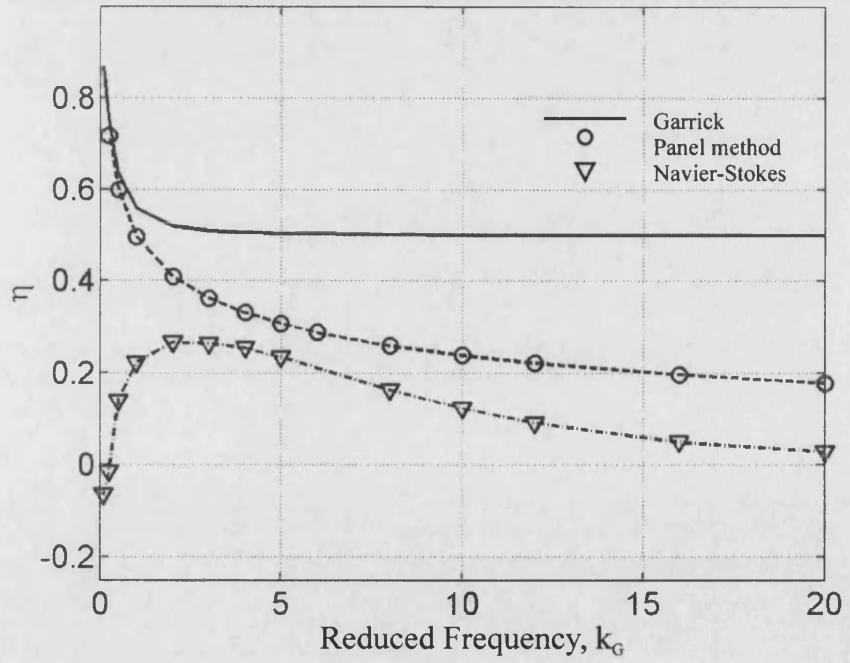

(b)

Figure 1.12: Comparison of linear theory, panel method, and Navier-Stokes predictions for a NACA0012 airfoil in pure heave, $k_G h$=0.3 (St=0.19) [56].

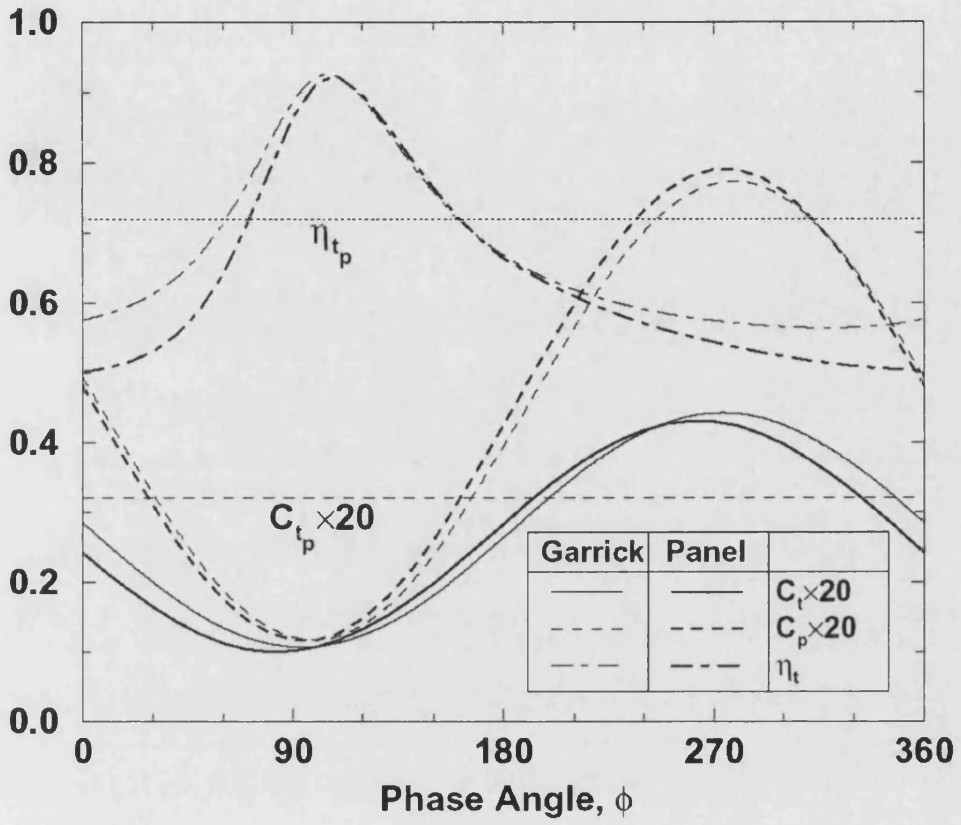

Figure 1.13: Effect of pitch phase angle on the predicted thrust and efficiency according to Garrick theory and the panel method, h=0.2, k_Gh=0.05 [43].

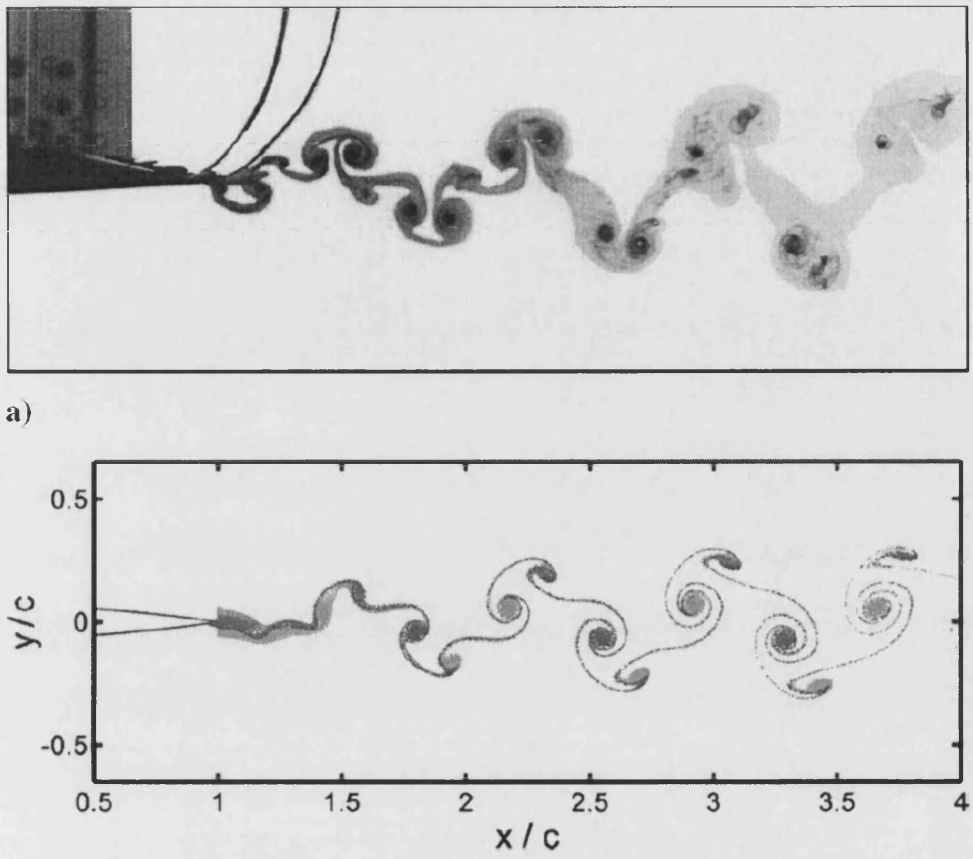

Figure 1.14: Comparison of experimental[24] and Navier-Stokes[44] wake patterns corresponding to drag. NACA0012 airfoil, St=0.05, Re=$2x10^4$.

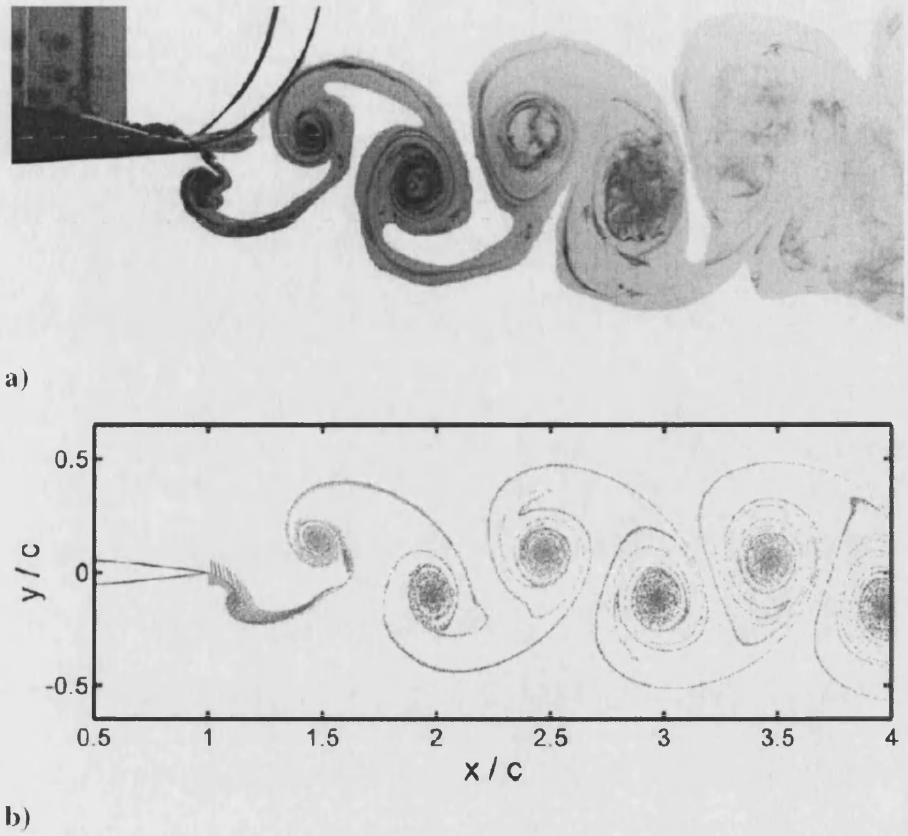

Figure 1.15: Comparison of experimental[24] and Navier-Stokes[44] wake patterns corresponding to thrust. NACA0012 airfoil, St=0.2, Re=$2x10^4$.

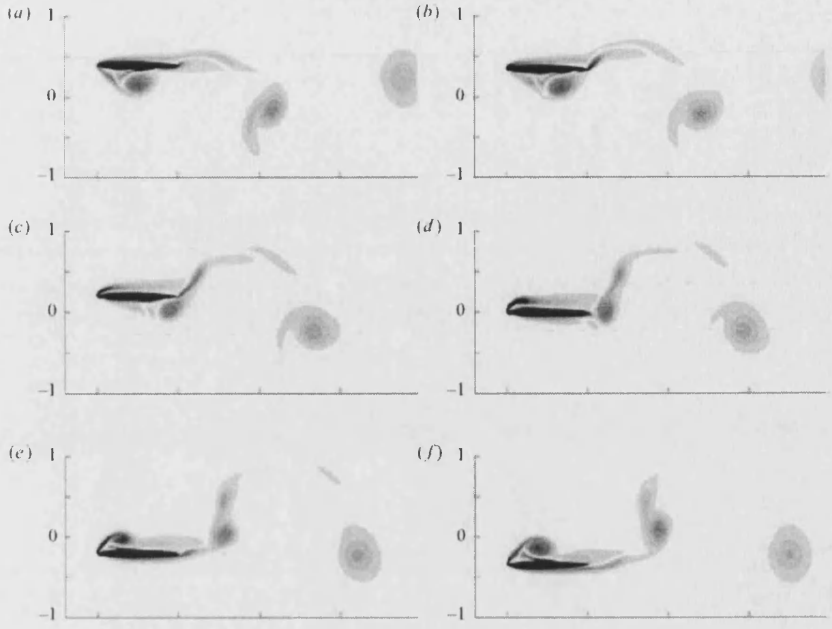

(i)

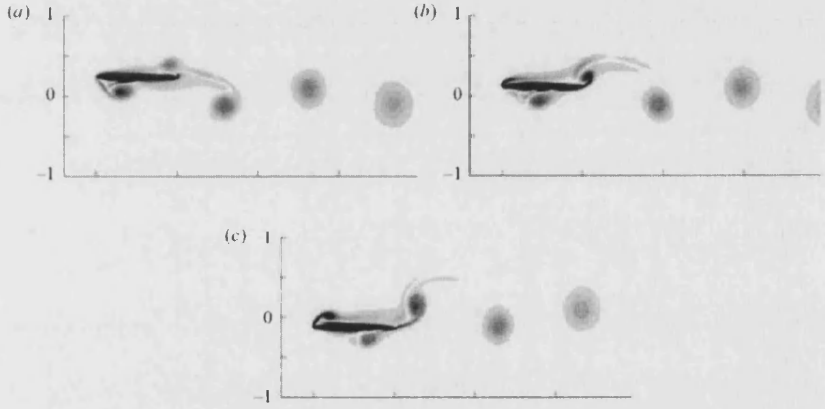

(ii)

Figure 1.16: Navier-Stokes vorticity fields showing: (i) constructive interference between leading and trailing-edge vortices; (ii) destructive interference; (iii) leading-edge vortex dissipation; (iv) leading-edge vortex shredding. NACA0012 airfoil in pure heave. Re=500 [17].

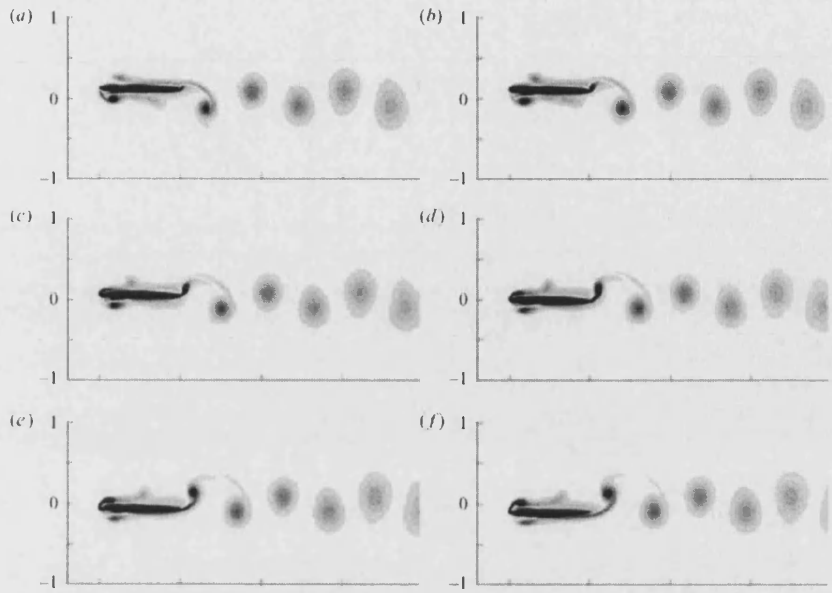

(iii)

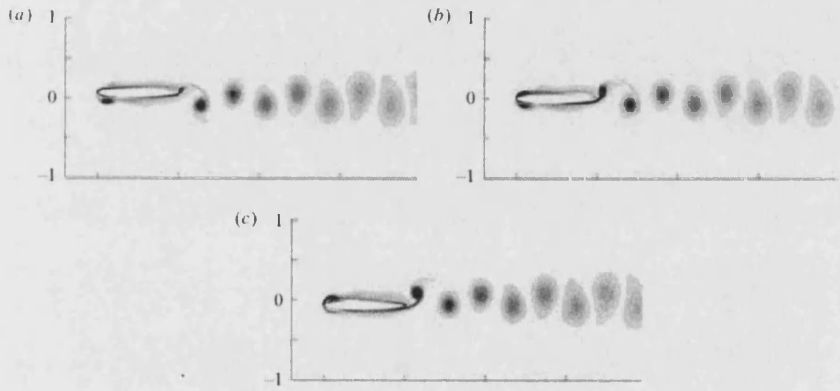

(iv)

Figure 1.16 Cont.

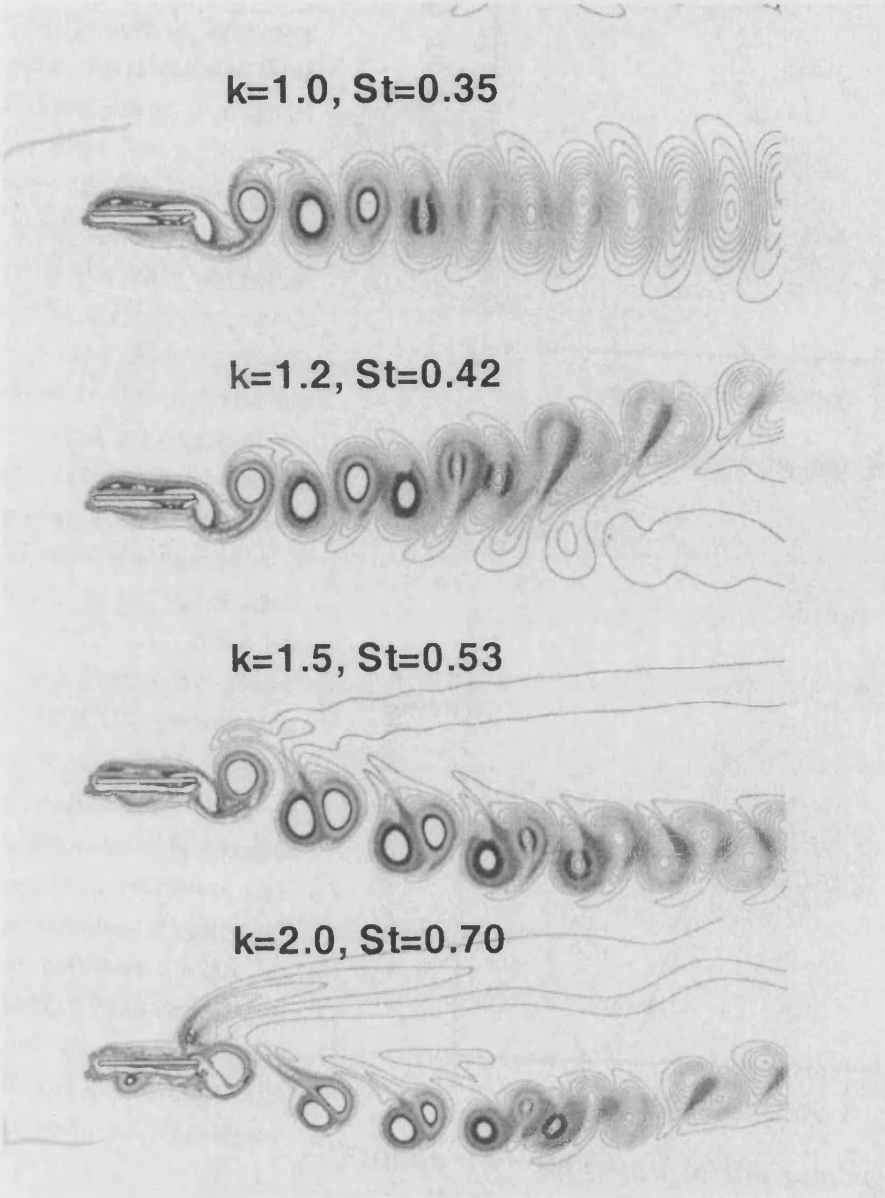

Figure 1.17: Deflected wake patterns observed for a flat plate in pure pitch. Re=200 [60].

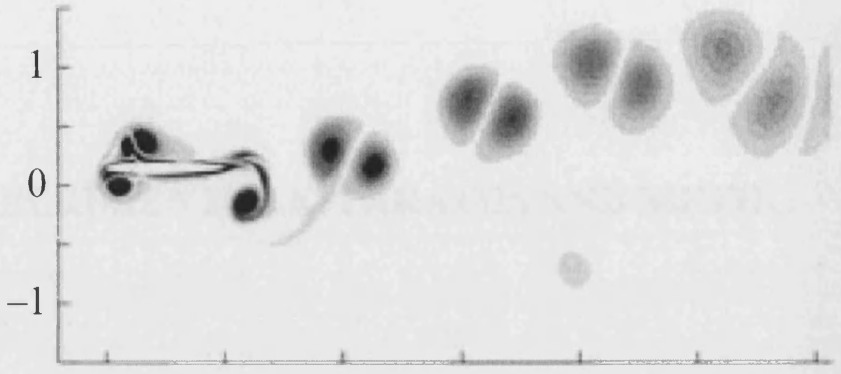

(a)

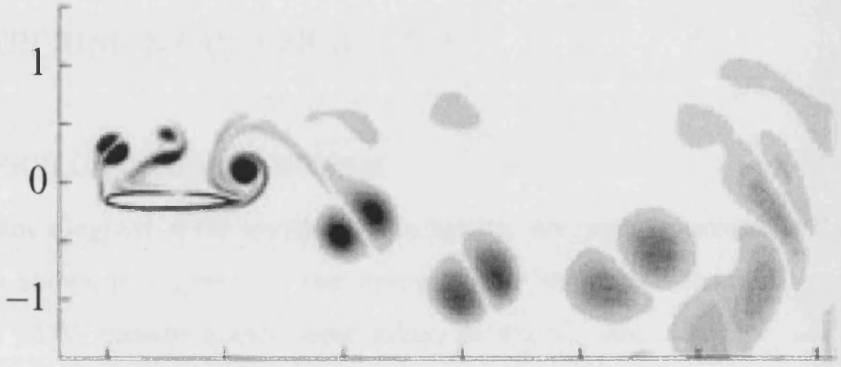

(b)

Figure 1.18: Deflected wake patterns computed for a NACA0012 airfoil in pure heave. The vortex pattern, and thus the direction of the jet, is observed to switch between (a) and (b). St=0.48, Re=500 [17].

2 EXPERIMENTAL APPARATUS AND METHODS

2.1 EXPERIMENTAL APPARATUS

2.1.1 OSCILLATING MECHANISM

A schematic diagram of the oscillating mechanism for the measurements in still water and air is shown in Figure 2.1. The orientation of the measurement plane, in which PIV and LDV measurements were taken is shown, and also the origin of the coordinate system. The airfoil was mounted vertically with one end attached to a horizontal shaker (Motovario 0.37 kW three-phase motor of operational range of 60-600rpm and IMO Jaguar controller). A rotary displacement encoder was attached to the motor spindle, from which the location of the airfoil could be derived.

2.1.2 WATER TANK

Experiments at zero freestream velocity were carried out in a 1.2x0.5x0.5 m glass tank (see Figure 2.2) for frequencies in the range $1<f<2.5$ Hz and amplitudes in the range $5<a<25$ mm. Splitter plates were placed at the root and tip of the wing, in order to preserve the two-dimensionality of the flow. There was a 2 mm (0.03c) gap between the top of the airfoil and a Perspex splitter plate, and a 2 mm gap between the bottom of the airfoil and the bottom of the tank. The orientations of the LDV probe and PIV camera and laser are shown.

2.1.3 OPEN AIR EXPERIMENTS

A number of experiments were carried out in still air, in the absence of the tank. The experimental setup is shown in Figure 2.3. The airfoil oscillates between splitter plates with a 2 mm gap at each end. Smoke is released upstream, and in a vertical direction (parallel to the span), such that the smoke has initially zero velocity in the chordwise direction. Smoke was provided by a 6-jet linsead oil atomiser.

2.1.4 WATER TUNNEL

Experiments at non-zero freestream velocity were conducted in a free-surface closed-loop water tunnel (Eidetics Model 1520) with a 381mm wide x 508mm deep x 1530mm long test section and flow speed range of 0-0.45 m/s (see Figure 2.4). The airfoil was mounted vertically with one end attached to a horizontal shaker (Motovario 0.37 kW three-phase motor, 5:1 worm gear and IMO Jaguar controller). The position of the root of the airfoil was measured with a rotary encoder fixed to the spindle of the worm gear shaft. The amplitude of the oscillation, a=17.5mm, was fixed for all experiments. Experiments were carried out over a frequency range of $0.3<f<2.5$ Hz. The flow velocity was checked with LDV apparatus. The turbulence intensity was measured with LDV to be less than 0.5%. The water-tunnel motor drive was found to generate high-frequency (20kHz) electrical noise, and for this reason a number of low-pass filters were required for the force measurement system, in addition to electrical shielding. Before each test run, the tunnel was given time to attain a steady flow speed. Perspex end plates were placed at one or both ends of the airfoil, in order to preserve the two-dimensional nature of the flow over the wing. The gap between the end of the airfoil and the end plate was less than 3% of the chord-length.

2.1.5 FORCE MEASUREMENT

The forces applied to the wing in the 'x' and 'y' directions, 'F_x' and 'F_y', were measured with a two-component binocular strain gauge force balance[61] machined from Aluminium. The peak lateral forces were found to exceed the peak thrust forces by a factor of approximately 10, and the strain gauges were chosen accordingly. The signal was amplified by a Wheatstone bridge circuit, and sampled with an A/D converter with a sample rate of 1kHz. The gain of the amplifier was chosen to yield a

high output voltage in the case of peak instantaneous force, but to remain within the linear-amplification range. The amplified signal was sampled with an analog to digital converter on a Pentium III desktop computer running HP Vee data acquisition software. The signal from the rotary encoder was also sampled, yielding force-displacement curves for both thrust and lift components.

2.1.6 CHORDWISE FLEXIBLE AIRFOIL

The effect of chordwise flexibility was studied with a 300 mm span, 90 mm chord, tear-drop/flat plate airfoil (Figure 2.5). It is noted that the shape of the airfoil follows the observations of Wootton[30] that bird's wings have relatively stiff leading-edges, and resembles the airfoil of the MAV of Jones[52], and in some ways the tadpole in the CFD study of Liu et al.[62]. Unlike experimental studies of rigid airfoils in coupled heave and pitch, the pitching motion arises naturally through chordwise flexibility. The leading-edge element was machined from solid Aluminium, and designed to be stiff in both the chordwise and streamwise directions. The trailing-edge element was a Carbon-Manganese steel plate of length 60 mm and modulus of elasticity 2.05×10^{11} N/m^2 . Experiments were performed with plate thicknesses of 2/1000", 3/1000", 4/1000", 5/1000", 6/1000", 8/1000", and 15/1000", corresponding to thickness ratios of $b/c=0.56 \times 10^{-3}$, 0.85×10^{-3}, 1.13×10^{-3}, 1.41×10^{-3}, 1.69×10^{-3}, 2.23×10^{-3}, and 4.23×10^{-3} respectively. The choice of thickness values was found to lead to a broad range of flexibilities: the deformation of the airfoil of plate thickness $b/c=4.23 \times 10^{-3}$ was found to be very small (pitch amplitude less than 2 degrees for the highest oscillation frequency), whereas very large deflections (pitch amplitude exceeding 20 degrees) were observed for the airfoil of plate thickness $b/c=0.56 \times 10^{-3}$. The bending of the airfoil is shown schematically in Figure 2.6. If the bending stiffness coefficient of the thinnest plate is given the symbol λ_0, then from Equation 1.2: $\lambda_0=0.614$ for Re=9000; $\lambda_0=0.154$ for Re=18000; and $\lambda_0=0.068$ for Re=27000. The bending stiffness of each plate relative to the thinnest is given in Table 2-1.

Plate Thickness, b/c	Relative Stiffness, λ/λ_0
0.56×10^{-3}	1
0.84×10^{-3}	3.4
1.12×10^{-3}	8
1.41×10^{-3}	15.6
1.69×10^{-3}	27
2.25×10^{-3}	64
4.23×10^{-3}	422

Table 2-1

2.1.7 SPANWISE FLEXIBLE AIRFOIL

Three NACA0012 wings of 300mm span, 100mm chord and rectangular planform were constructed to investigate the effect of spanwise flexibility. The first, termed *Inflexible*, was designed to be as stiff as possible. The second, termed *Flexible*, was designed to be of intermediate flexibility. The third, termed *Highly Flexible*, was designed to be overly flexible. Cross sections of the three wings are shown in Figure 2.7. The Inflexible wing was constructed from Nylon (E=5GPa) in a Rapid Prototyping machine. A hollowed structure and two 8mm diameter steel rods (E=200GPa) spanning from root to tip ensure a high spanwise stiffness. The surface of the wing was sanded smooth. Each of the two flexible wings was constructed from Polydimethylsiloxane rubber (PDMS, E=250kPa) cast in a NACA0012 mould. The Flexible wing was stiffened with a 1mm stainless steel sheet (E=210GPa); the Highly Flexible wing was stiffened with a 1mm aluminium sheet (E=70GPa). The orientation of the wing and end-plate is shown in Figure 2.8. The arrangement may be considered to represent the semi-span of a 600mm span wing. All three wings were designed to be stiff in the chordwise direction. The degree of chordwise flexing in the experiment was observed to be negligible for all wings and all frequencies. For the three-dimensional spanwise flexibility experiments, an end plate was present 2mm from the root of the wing, and the gap between the wing tip and the glass wall of the water tunnel was 5c/3.

2.1.8 FORCE-MEASUREMENT-VALIDATION AIRFOIL

A fourth wing, of 400mm span, was constructed in a Rapid Prototyping machine for a set of force measurement validation tests. The design of the wing was identical to that of the NACA0012 airfoil termed *Inflexible* above.

2.2 EXPERIMENTAL METHOD

2.2.1 FORCE MEASUREMENT

The forces applied to the wing in the 'x' and 'y' directions, 'F_x' and 'F_y', were measured with a two-component binocular strain gauge. The calibration was performed by loading the gauge with known weights. Calibration was repeated before and after sets of experiments to ensure consistency. Sets of data chosen at random were repeated to ensure the reproducibility of the results. The sensitivity of the recorded signal to the sample rate was examined by sampling at rates of 10, 100, 1000, and 10000Hz. A sufficiently high frequency was found to be needed to capture successfully the signals from the position encoder. Excessively high sample rates were avoided because of the consequent large file size. Drive force and thrust force data were collected for 60 oscillations for each test condition. In choosing this number of oscillations, a balance was sought between experimental scatter (too few oscillations) and large file size (too many oscillations).

The force 'F_x' is equal to the drag (or thrust) on the wing. The force 'F_y' is equal to the lift on the wing, plus a contribution arising from the inertia of the wing. For the flexible wings a second contribution arises from the elasticity of the wing. Finding the instantaneous lift force from the driving force would involve a careful kinematics study. However, since the wing returns to the same shape and position at the end of every cycle, the net work done on the *wing* is zero, and the work done by the driving mechanism over one cycle must equal the work done on the fluid. The period-averaged power input therefore equals the period-averaged value of '$F_y v$', where 'v' is the instantaneous velocity of the root.

In the case of non-zero freestream velocity, the thrust coefficient, C_T, is given by

$$C_T = \frac{T}{\frac{1}{2}\rho U_0^2 c} \tag{2.1}$$

where, 'T' is the thrust per unit span. The time-averaged thrust coefficient is found by averaging over 60 complete heave oscillations. The time-averaged power input is given by

$$\overline{C_P} = \frac{\overline{F_y \mathrm{v}}}{\frac{1}{2}\rho U_0^3 c} \tag{2.2}$$

where, '$F_y v$' is the instantaneous power input, and the overbar denotes an average over time. The efficiency is given by

$$\eta = \frac{\overline{T}U_0}{\overline{F_y \mathrm{v}}} = \frac{\overline{C_T}}{\overline{C_P}} \tag{2.3}$$

In the case of zero freestream velocity the thrust coefficient is defined based on the peak heave velocity, $v_p=2\pi fa$:

$$C_{TVp} = \frac{T}{\frac{1}{2}\rho \mathrm{v}_P^2 c} \tag{2.4}$$

The propulsive efficiency, η, is undefined when the freestream velocity is zero. An alternative measure of performance is the thrust to power-input ratio[61] (units of Newton/Watt):

$$\varepsilon = \frac{\overline{T}}{\overline{F\mathrm{v}}} \tag{2.5}$$

2.2.2 FORCE MEASUREMENT ERROR

Since the fluid dynamic forces may vary along the span, it is important for the strain gauge to be sensitive only to force, and insensitive to the distance from the gauge at which the force acts. Insensitivity to bending moment is a key feature of a binocular

strain gauge. It was found during the calibration tests that the error in 'F_x' and 'F_y' induced by a typical range of bending moments is less than 0.5%. Coupling effects – fictitious indicated forces due to loading in the other direction – were found to give rise to a 2% error. The error due to torque about the z-axis was found to be 1%. The error from temperature variations was found to be negligible. The response of the gauge was found to be linear (1% uncertainty) over the experimental range. The combined error in the strain gauge readings is approximately 5%. Since the efficiency calculations depend on the gauge readings in both directions, the error in the efficiency data is approximately 10%.

The uncertainty in the PIV measurements of momentum flux is estimated to be less than 10%.

2.2.3 FORCE MEASUREMENT VALIDATION

Measurements from the present experiment are compared to sets of constant Strouhal number data from the literature in Figure 2.9. Although data for the cases of pure pitch and coupled heave and pitch is present, experimental data for the case of pure heave was found to be largely absent from the literature. For this reason, a comparison with numerical simulations was made. Unless stated, each set of data is for a NACA0012 airfoil in pure heave, and the Strouhal number, St=0.19, and Reynolds number, Re=20,000, are the same in each case. Several series are shown: inviscid predictions (Garrick[9], panel method[44]), Navier-Stokes simulations[44], and experimental data from the present experiment and from the literature[26, 63, 64]. Close agreement is observed between the present experiment and the Navier-Stokes simulations of Young and Lai[44], and between the experimentally measured drag coefficient (C_D=0.028±0.005) and the values of Sheldahl and Klimas[63] (C_D=0.0245) and Koochesfahani[26] (C_D=0.027). The predictions of the inviscid methods are qualitatively different, relating again to flow separation effects[44]. A comparison of efficiency data is made in Figure 2.10 for constant heave amplitude. The present experimental data is found to be in agreement with the Navier-Stokes predictions in terms of magnitude. Although not plotted, experimental data from Schouveiler et al.[49] indicates a peak efficiency of approximately 33% for St=0.12 for the pure heave of a NACA0012 airfoil for Re=40,000, h=0.75. This optimum

Strouhal number is in close agreement with the present experimental data. It is noted that, for the present experimental efficiency results, the effect of Reynolds number is small in the range of 10,000<Re<30,000 and the Strouhal number is the key parameter in determining both the thrust and efficiency of the airfoil.

2.2.4 DISPLACEMENT MEASUREMENT

The oscillating wing was filmed with a 50 frames-per-second high-shutter-speed video camera. Specialist motion-tracking software (RealViz MatchMover Pro 3.1) returned the coordinates of either the leading and trailing-edges (chordwise flexibility) or of the root and tip (spanwise flexibility) in each frame. After the initial transients, the displacements of these points were recorded over six oscillations (beyond six, the improvement in the accuracy of the derived quantities was found to be negligible). The displacement data was exported in Comma Separated Variable (CSV) format, and analysed with a Visual Basic for Applications (VBA) macro written by the author to yield the phases and amplitudes of interest with a cosine fit method.

2.2.5 LASER DOPPLER VELOCIMETRY

A TSI Inc. LDV system was used to make single point velocity measurements in air and water. The LDV system, which operates in backscatter mode, was capable of measuring two components of velocity, although only the streamwise component was measured in the experiments. The system comprised a 300mW air-cooled Argon-Ion laser (wavelength 514.5nm (green light)), photo multiplier tube, photo-diode detector, and data processor. Data is collected in real time mode (as opposed to eventime sampling) on a single processor Xeon computer. A lens of focal length 250mm was chosen, with a beam spacing of 50mm. The measurement volume diameter was of diameter 65μm and length 0.68mm. The Bragg cell frequency, band-pass filter, photo multiplier voltage and burst threshold voltage were set manually through the software (TSI Flowsizer), to values found to optimise the data collection rate and accuracy. The measurements of velocity were exported in CSV format and analysed with a set of VBA macros, written by the author. Data rates in excess of 500Hz were achieved in air, with the seeding provided by a 6-jet atomiser (smoke generator) while data rates in excess of 100Hz were achieved in water, both sufficiently high to yield a

detailed history of the time-variation of the flow, even in the highest oscillation frequency cases.

It is noted that special care was taken to attain the correct degree of seeding, to align the laser and optics to achieve the maximum brightness and therefore data rate, and in the case of open air smoke experiments, to seal the doorways of the lab and to leave the lab for the duration of the data collection, in order to minimise air currents.

2.2.6 PARTICLE IMAGE VELOCIMETRY

A TSI Inc. PIV system was used to measure the instantaneous velocity field in the x-y plane. The system comprised a 2048x2048 pixel 8-bit grey scale digital camera, dual mini Nd:Yag 120mJ pulsed laser, remote focusing apparatus, synchronisation unit, SCSI image acquisition card, and dual Xeon processor computer. The seeding was provided by 4 μm Nylon particles. The separation of laser pulses was 500 μs, and velocity fields were captured at a rate of 3.75 Hz. The images were analysed with TSI Insight 6. A window size of 32x32 pixels with 50% overlapping was chosen, to give 127x127 velocity vectors with spatial resolution 0.016c. A Fast-Fourier-Transform algorithm was used to analyse the image pairs. Time-averaged flow fields were obtained by taking an average of 256 velocity fields. Phase-averaged flow fields were obtained by taking an average of 200 velocity fields. Ensemble-averaging was used to obtain statistical information such as maximum streamwise velocity, circulation, and vortex spacing. Such data analysis was achieved with VBA macros written and tested by the author.

The calibration of the PIV system was verified by comparison with LDV measurements of the freestream velocity. The airfoils were spray-painted black in order to minimise reflections. Special attention was given to the degree of seeding, alignment of the laser and focus of the camera, in order to attain clear images.

The momentum flux per unit span one chord length downstream of the trailing-edge is calculated from the instantaneous velocity fields as:

$$M = \rho \int \overline{U_x^2} dy \qquad (2.6)$$

where U_x is the instantaneous velocity and overbar denotes time-averaging. A momentum flux coefficient may be defined as:

$$C_M = \frac{M}{\frac{1}{2}\rho V_P^2 c} \tag{2.7}$$

2.2.7 LASER SHEET VISUALISATION

A laser sheet was used for visualisation of plate deformation, which was generated from a Coherent 12W Ar-ion continuous laser beam by cylindrical and spherical lenses. A 50 frames per second digital video camera mounted underneath the airfoil was used to record the motion of the wing. The laser sheet illuminated the plane of intersection of the mid-span. The laser sheet and camera were oriented identically to the PIV laser and camera.

2.3 FIGURES

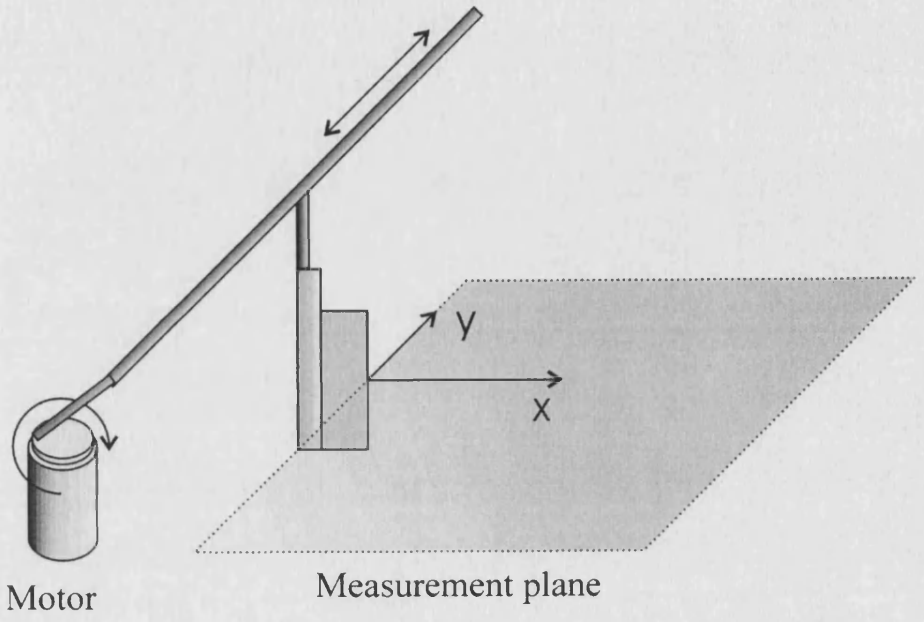

Figure 2.1: Schematic diagram of the water tank drive mechanism.

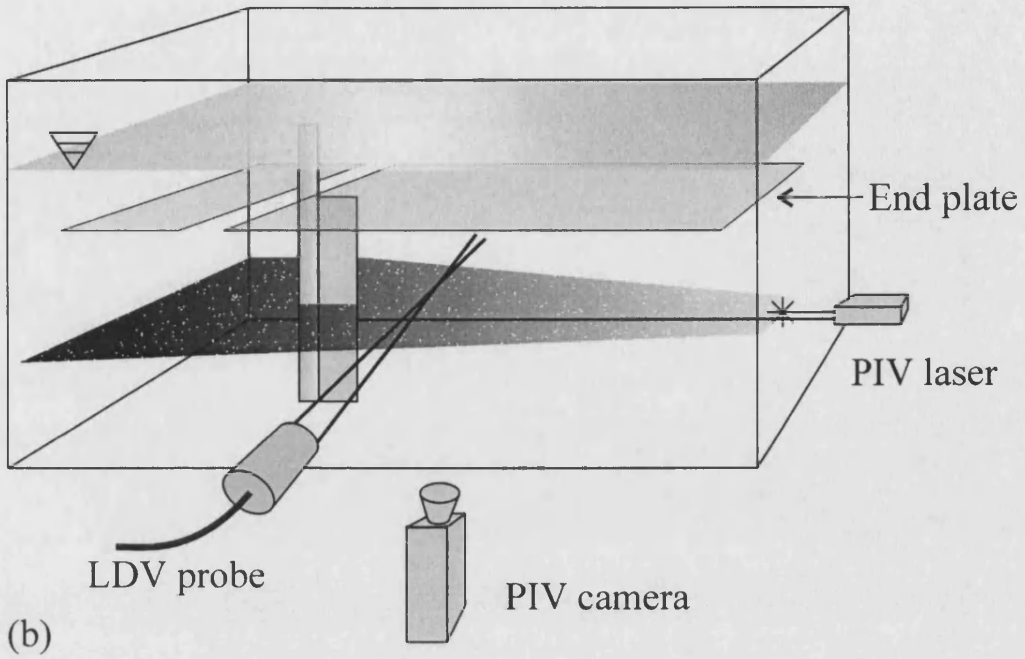

Figure 2.2: Diagram of the orientation of the airfoil and measurement apparatus for the water tank PIV and LDV experiments.

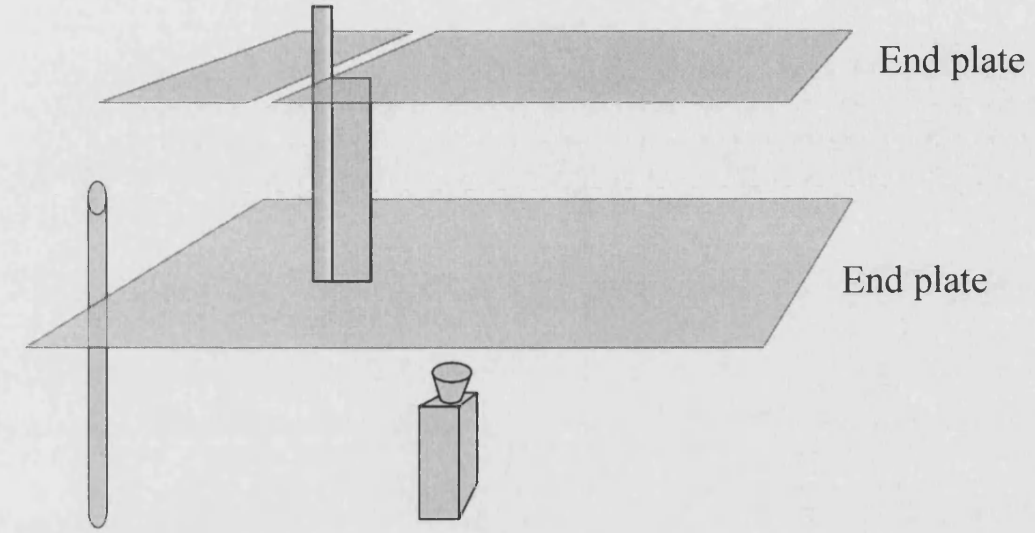

Figure 2.3: Position of the digital camera, end plates and smoke pipe in the open-air flow visualisation experiments.

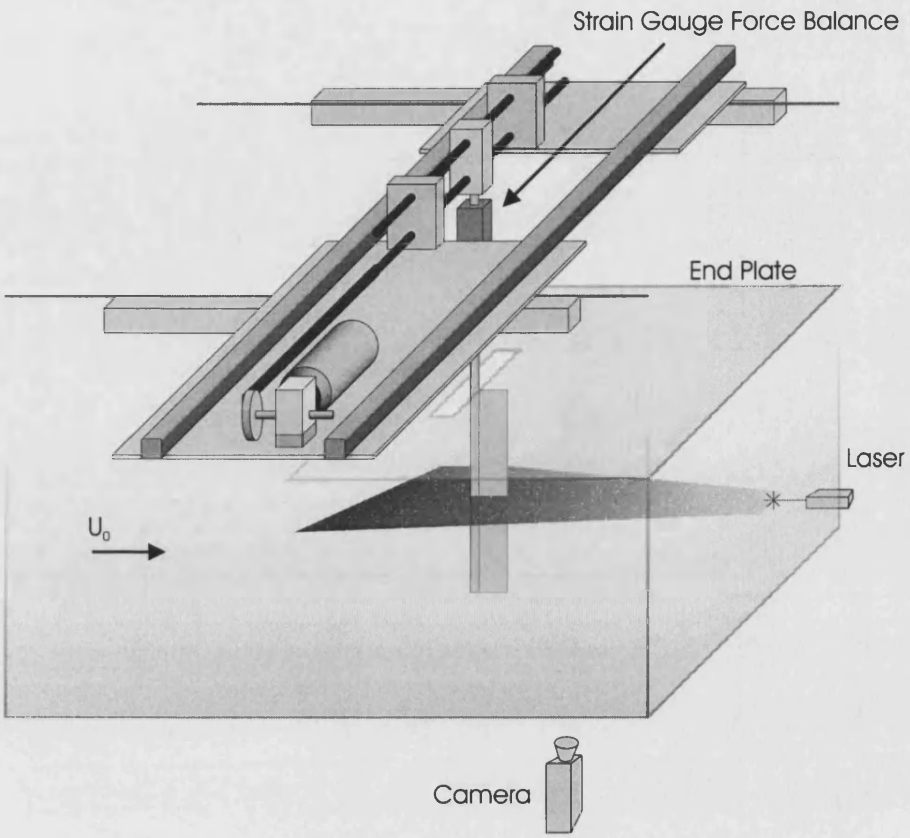

Figure 2.4: Diagram of the water tunnel drive mechanism. The motor and worm gear are shown. One end of the worm gear spindle is attached to the disk and crank arm, the other end to a rotary encoder. The position of the upper end-plate, camera and laser for PIV experiments, and two-component strain gauge, is shown.

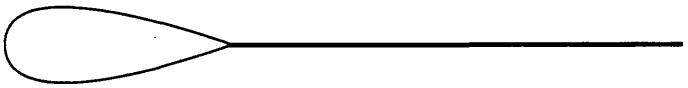

Figure 2.5: Scale diagram of the chord-wise flexible airfoil. The leading-edge is machined in two halves, and the plate clamped between the two.

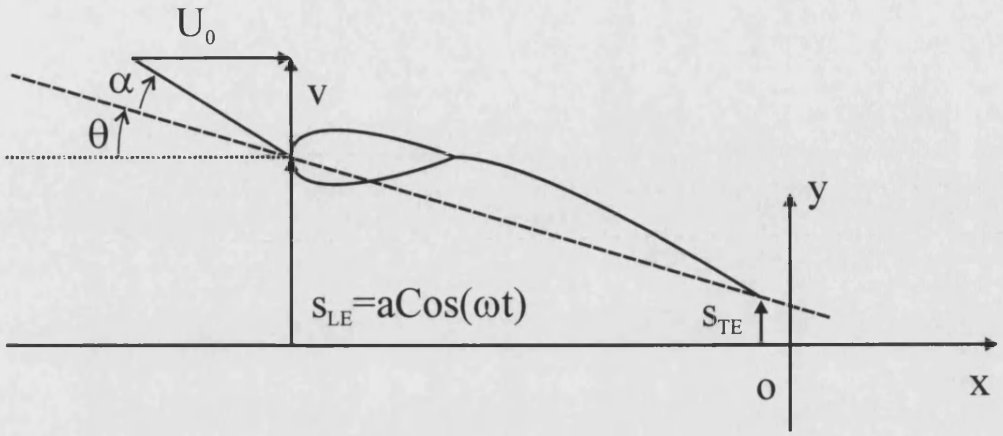

Figure 2.6: Diagram of the chord-wise flexible airfoil oscillating in heave at a point in time during the upstroke. The effective angle of attack, α, plus the angle of pitch, θ, is equal to the angle of incidence, $\arctan(v/U_0)$. The airfoil tends to align itself to the flow, thus lowering the effective angle of attack. The phase and amplitude of the pitch motion may be found from measurements of the pitch angle, θ, over one cycle.

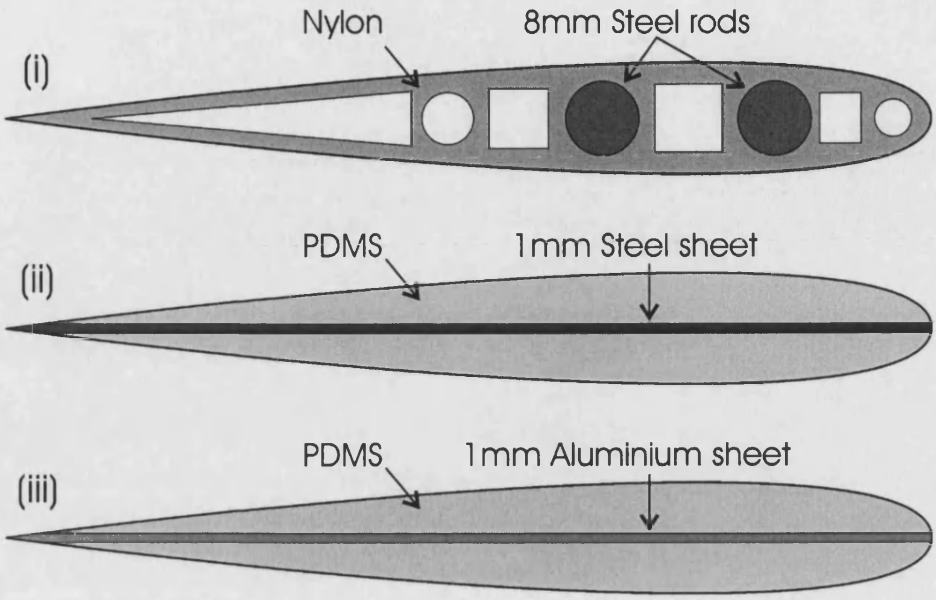

Figure 2.7: Cross sections of the three spanwise-flexible NACA0012 wings; (i)Inflexible, (ii)Flexible, (iii)Highly Flexible.

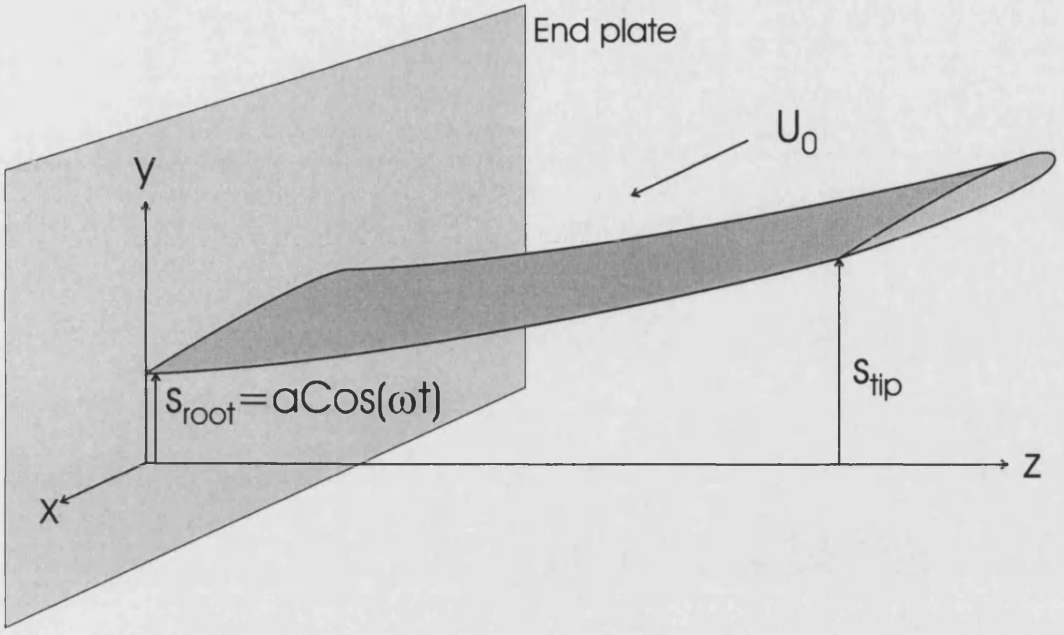

Figure 2.8: Schematic of the spanwise flexible airfoil in heave.

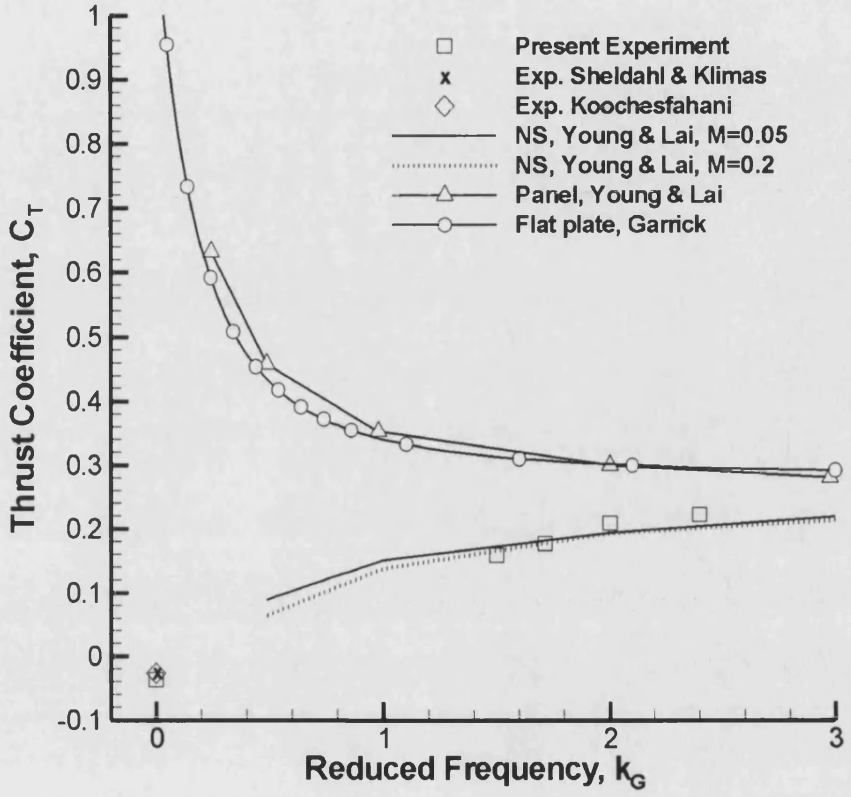

Figure 2.9: Comparison of present experimental data (square symbols) with analytical, numerical and experimental data from the literature; Sheldahl & Klimas[63], Koochesfahani[26], Young & Lai[44], Garrick[9]. Re=20,000, NACA0012 profile. Exception: Koochesfahani, Re=12,000.

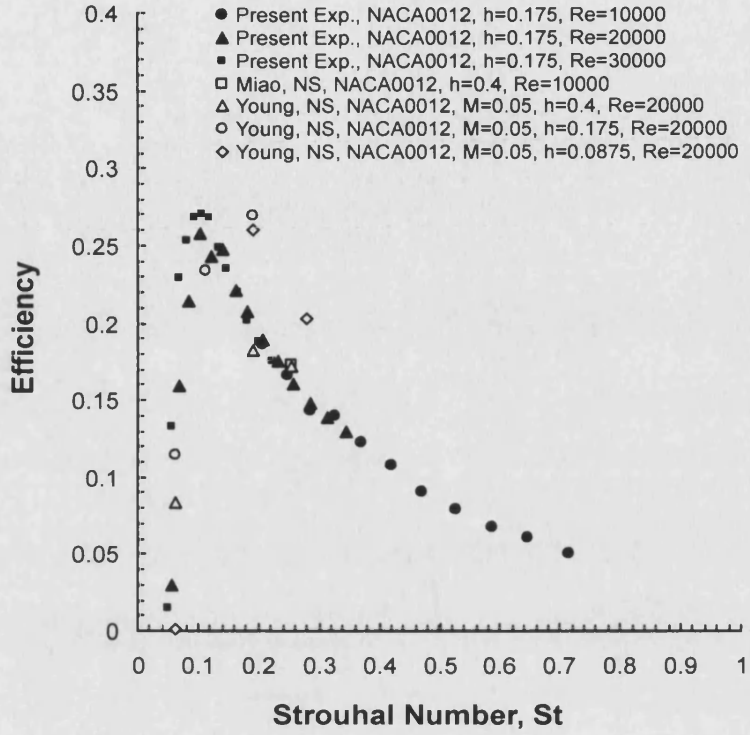

Figure 2.10: Comparison of present experimental efficiency data with values from the literature; Miao & Ho[36], Young[56].

3 EFFECT OF CHORDWISE FLEXIBILITY AT ZERO FREESTREAM VELOCITY

3.1 SUMMARY

Thrust generation for an airfoil heaving at zero freestream velocity, the case relevant to hovering birds and insects, has been studied. The objective was to investigate the effect of airfoil stiffness. PIV and force measurements were taken for three airfoils of relative bending stiffness 1:8:422 in a water tank. The deformation of the flexible airfoils produces an angle of attack, which varies periodically with a phase angle with respect to the heaving motion. Amplitude and phase of this combined heaving/pitching motion play a major role on the flow field and thrust generation. Vortex pairs or alternating vortex streets were observed depending on the amplitude and phase lag of the trailing-edge. The strength of the vortices, their lateral spacing and the time-averaged velocity of the induced jet were found to depend on the airfoil flexibility, heave frequency and amplitude. Direct force measurements confirmed that at high heave frequencies the thrust coefficient of the airfoil with intermediate stiffness was greatest, although the least stiff airfoil can generate larger thrust at low frequencies. It is suggested that there is an optimum airfoil stiffness for a given heave frequency and amplitude. The thrust/power input ratio was found to be greater for the flexible airfoils than for the rigid airfoil.

3.2 AIM

The aim of this chapter is to establish whether chordwise flexibility is beneficial in the case of an airfoil in pure heave in still water/air. The effect of flexibility is studied with measurements of the airfoil shape, velocity field, forces, and thrust/power input ratio. Comparison over a range of frequencies, amplitudes and airfoil flexibilities is made. Since the freestream velocity is zero, the oscillation frequency is expressed through the Reynolds frequency, Re_f, and thrust coefficient is based on the peak heave velocity (Equation 2.4). The thrust to power input ratio (Equation 2.5) is interpreted as a measure of efficiency. The heave amplitude and airfoil stiffness may be expressed through the heave amplitude, h, and plate thickness, b/c, parameters. Experiments were carried out with the chordwise flexible airfoil shown in Figure 2.5. The three plates of thickness $b/c=0.56x10^{-3}$, $b/c=1.13x10^{-3}$, and $b/c=4.23x10^{-3}$ were tested.

3.3 RESULTS

3.3.1 FLOW/STRUCTURE INTERACTION

Figure 3.1 shows the $b/c=0.56x10^{-3}$ plate over one oscillation cycle for $Re_f=20,250$ and h=0.194. The inset in the figure shows the variation of location of the leading-edge as a function of time. The tear-drop leading-edge element is partly visible. The deformation of the airfoil shown in Figure 3.1 produces an angle of attack as well as a camber, which varies periodically with a phase angle with respect to the heaving motion. For the rigid airfoil, the pure heaving motion at zero freestream velocity produces effective angles of attack of +90 or –90 degrees. However, for a flexible airfoil, pitching angle is generally negative during the downward heaving motion, which results in an effective angle of attack smaller than 90 degrees. This pitching motion appears to play a major role on the flow field and thrust production, as will be discussed below.

The instantaneous location of the trailing-edge of the plate was measured and is plotted in Figure 3.2(a). The variation of location of the trailing-edge for the other airfoils is shown in the same figure. It is seen that the displacement of the trailing-edge has a large phase lag for the flexible wings. Surprisingly, the maximum values of the displacement are smaller for the $b/c=0.56x10^{-3}$ plate than the $b/c=1.13x10^{-3}$ plate.

This is due to the phase lag between the heaving motion and deformation of the flexible plates. Figure 3.2(b) shows the displacement of the trailing-edge relative to the leading-edge, which is the time history of the relative deformation. It is seen that the deformation of the $b/c=0.56x10^{-3}$ plate is larger and the phase lag is also substantial. Nevertheless, the amplitude of the deformation is not very different for the two cases. The phase delay, however, appears to play a major role, as will be discussed below.

Since the deformation and dynamic response of the flexible plates affects the resulting flow considerably, the response of the plates will be summarised in this section before the results of the velocity and force measurements are presented. As the first bending mode is dominant in the range of the parameters tested, the amplitude and phase angle of the trailing-edge are sufficient to characterise the dynamic response of the plates. Figure 3.3 shows the variation of amplitude and phase of displacement of the trailing-edge as a function of frequency for h=0.194. The trailing-edge amplitude is greater than the leading-edge amplitude for both the $b/c=1.13x10^{-3}$ and $b/c=0.56x10^{-3}$ airfoils over the range of frequencies tested. The trailing-edge amplitude of the $b/c=1.13x10^{-3}$ plate first increases and then decreases with frequency. The trailing-edge amplitude of the $b/c=0.56x10^{-3}$ plate decreases steadily with frequency and the curves cross at around Re_f =10,000. For higher frequencies, the amplitude of the motion of the trailing-edge is larger for the $b/c=1.13x10^{-3}$ plate than the $b/c=0.56x10^{-3}$ plate, as a consequence of combined heaving motion and dynamic deformation.

It is seen from Figure 3.3b that the phase lag increases roughly linearly with frequency for the two flexible plates. The phase lag is approximately 60 degrees greater for the $b/c=0.56x10^{-3}$ airfoil. Note that the displacement of the trailing-edge depends on the amplitude and phase angle of deformation with respect to the heaving motion. This variable is different to the deformation only. If the deformation only is considered, it is observed to increase with frequency as expected (see Figure 3.4). Figure 3.5 shows the amplitude and phase of the trailing-edge as a function of heave amplitude for Re_f =16,200. Once again, the trailing-edge amplitude is greater than the leading-edge amplitude for both the $b/c=1.13x10^{-3}$ and $b/c=0.56x10^{-3}$ airfoils over the range of amplitudes tested. The normalised trailing-edge amplitude decreases with increasing heave amplitude for both the $b/c=1.13x10^{-3}$ and $b/c=0.56x10^{-3}$ airfoils. The

phase lag is almost independent of heave amplitude, but depends greatly on the flexibility of the airfoil.

3.3.2 VELOCITY MEASUREMENTS

Figure 3.6 shows the instantaneous velocity fields for the three plates, corresponding to Figure 3.2 (Re_f =20,250, h=0.194). It is seen that the structure of the vortical flow is similar for the b/c=4.23x10^{-3} and b/c=1.13x10^{-3} plates, resembling vortex pairs released periodically. Three differences are observed: the vortices from the b/c=1.13x10^{-3} airfoil are slightly stronger, slightly further apart in the lateral direction, and appear to be preserved further downstream than the vortices from the b/c=4.23x10^{-3} airfoil. A quite different flow structure resembling a reverse von Kármán vortex street is observed for the b/c=0.56x10^{-3} plate. The vortices are weaker and closer in the lateral direction; much lower induced velocities are observed.

The pairs of vortices in Figure 3.6(a) are observed to lie at an angle to the 'x' direction. Similarly, the vortex street in Figure 3.6(a) is seen to be deflected away from the axis. The deflected jet indicates the presence of a time-averaged lift force. The deflected jet phenomenon is investigated in Chapter 4.

Instantaneous and time-averaged flow fields were studied in detail for further statistical information. The strength of the vortices generated close to the oscillating plate was calculated by evaluating the line integral of velocity around a square path at every point in the velocity field. The point about which the circulation was found to be greatest was then identified as the vortex core (greatest negative value for the vortex of opposite sign). With the aid of a computer algorith written by the author, the process was repeated for each instantaneous flow field. A line integral of velocity was chosen in preference to a surface integral of vorticity since the latter summation would be dominated by a small number of terms near the vortex core, which the PIV system is unable to measure accurately. The inaccuracy arises partly because of the coarseness of the grid, and partly because of the tendency of seeding particles to be displaced from the core. The average circulation of the vortices is shown in Figure 3.7 as a function of frequency. The strength is slightly larger for the b/c=1.13x10^{-3} plate than the b/c=4.23x10^{-3} plate, but there are substantial differences from the

b/c=0.56x10^{-3} plate at high frequencies. The vortex strength is almost constant for the b/c=4.23x10^{-3} and b/c=1.13x10^{-3} airfoils, but decreases rapidly with increasing frequency for the b/c=0.56x10^{-3} plate.

The variation of the maximum time-averaged jet velocity is shown in Figure 3.8. The variation of streamwise velocity with frequency is seen to be similar to the variation of circulation with frequency, although the flexibility of the plates seems slightly less important. The maximum time-averaged velocity is roughly equal to the peak heave velocity. Figure 3.9 shows the lateral spacing of the vortex rows as a function of frequency. The plate stiffness is seen to have a profound effect on the separation of the vortices, a quantity roughly proportional to the mass flux of the induced jet. The largest spacing is observed for the b/c=1.13x10^{-3} plate whereas the smallest spacing (roughly equal to the peak-to-peak heave amplitude) is observed for the b/c=0.56x10^{-3} plate. The effect of the flexibility is more important at higher frequencies.

In Figure 3.10 the variation of momentum flux with frequency is shown for each plate. The momentum flux has in some studies[19, 26] been taken as an estimate of the thrust force (however, a number of limitations exist[65]). The momentum flux is greatest for the b/c=1.13x10^{-3} plate and least for the b/c=0.56x10^{-3} plate. This implies that there is an optimum flexibility. The variation of the momentum flux resembles that of the vortex lateral spacing, indicating that the most important contribution comes from the effective jet width and mass flux.

Figure 3.11, Figure 3.12, Figure 3.13, and Figure 3.14 show the variation of circulation, peak time-averaged velocity, vortex spacing and momentum flux with heave amplitude for Re_f =16,200. Figure 3.11 shows that the strength of the vortices is least for the b/c=0.56x10^{-3} plate. There is a rapid decrease of the normalised circulation with increasing heave amplitude for the two flexible airfoils. The variation of the maximum time-averaged jet velocity normalised by the peak heave velocity is shown in Figure 3.12. The maximum time-averaged velocity decreases rapidly with increasing heave amplitude for all three airfoils. The effect of heave amplitude on the average lateral separation of the vortex rows is shown in Figure 3.13. At small amplitudes the vortex spacing is as high as three times the peak-to-peak heave amplitude. At high amplitudes the normalised vortex spacing approaches unity. Note

that there is a similarity between the variations of the vortex lateral spacing and the time-averaged jet velocity (see Figure 3.12).

The variation of the momentum flux with heave amplitude is shown in Figure 3.14. For comparison, Lai and Platzer[21] report velocity measurements and momentum flux estimates for a NACA0012 airfoil in pure heave. Momentum flux coefficients of C_M=1.6 and C_M=2.24 were found for 2h=0.08 and 2h=0.494, respectively. These estimated values are in good agreement with the results shown in Figure 3.14, in spite of the differences in geometry of the rigid airfoils and frequencies. It is seen in Figure 3.14 that at small amplitudes the momentum flux is a factor of 2-3 greater for the b/c=1.13x10^{-3} plate than for the b/c=0.56x10^{-3} or b/c=4.23x10^{-3} plates. At higher amplitudes the three curves converge; the effect of flexibility appears to be diminished. While the b/c=1.13x10^{-3} plate provides the largest momentum flux at small heave amplitudes, it decreases rapidly with increasing amplitude. The results shown above suggest that the b/c=1.13x10^{-3} plate generates larger thrust in general. These results were studied more closely by direct force measurements.

3.3.3 FORCE MEASUREMENTS

Figure 3.15 shows the variation of the thrust coefficient obtained directly from force measurements as a function of frequency for h=0.194. For Re_f <10,000, the b/c=0.56x10^{-3} plate has the greatest thrust coefficient. The thrust coefficient falls rapidly with increasing frequency though, and for Re_f >10,000 the b/c=1.13x10^{-3} plate has the greatest thrust coefficient. The thrust coefficient for the b/c=4.23x10^{-3} plate increases almost linearly with frequency. With the exception of the b/c=4.23x10^{-3} plate the trends in the momentum flux coefficient and thrust coefficient are similar. The magnitudes of the momentum flux and thrust coefficients differ by a factor of roughly two, illustrating that downstream momentum flux is not sufficient for an accurate estimate of the thrust. Figure 3.16 shows the variation of the thrust coefficient obtained directly from force measurements as a function of heave amplitude for Re_f =16,200. There is again a similar trend with the momentum flux coefficient obtained from PIV measurements. For coupled pitching and heaving studies reported by Freymuth[19] and Sunada et al.[20], the momentum flux and force coefficients (relatively high thrust coefficients in the range of 1 to 3) for typical

pitching amplitudes corresponding to these cases are consistent with the data for zero freestream velocity.

In Figure 3.17(a) and (b), the variation of thrust per unit power input with frequency and heave amplitude is shown. The power input is calculated from the strain gauge measurements of driving force and the velocity of the airfoil. The $b/c=0.56x10^{-3}$ plate is seen to be the most efficient for all values of frequency and the $b/c=4.23x10^{-3}$ plate the least. This behaviour is qualitatively different to the variation of thrust with frequency, where the $b/c=1.13x10^{-3}$ plate provides larger thrust, except at very low frequencies. The efficiency of the $b/c=0.56x10^{-3}$ plate is particularly high at low frequencies but, as with the thrust coefficient (Figure 3.15), it falls rapidly. The efficiency of the $b/c=1.13x10^{-3}$ plate declines gradually with increasing frequency. The efficiency of the $b/c=4.23x10^{-3}$ plate is remarkably constant. In Figure 3.17(b), thrust per unit power input is plotted as a function of heave amplitude. Over the range of heave amplitudes tested the $b/c=0.56x10^{-3}$ plate is the most efficient and the $b/c=4.23x10^{-3}$ plate the least. The general trend is for the efficiency to fall with heave amplitude.

3.4 CONCLUSIONS

Thrust generation for an airfoil heaving at zero freestream velocity, the case relevant to insects and birds moving off from rest, was studied. The objective was to study the effect of airfoil stiffness. PIV and force measurements were taken for three airfoils of relative bending stiffness 1:8:422.

The displacement of the trailing-edge of flexible airfoils was found to be larger than that of the rigid airfoil, and also to lag the displacement of the leading-edge. The maximum values of the instantaneous displacement are generally smaller for the $b/c=0.56x10^{-3}$ airfoil than the $b/c=1.13x10^{-3}$ airfoil as a consequence of large phase lags between the deformation and heaving motion. This phase lag, which increased with wing flexibility and heave frequency, produced very different vortical flows. Vortex pairs for the $b/c=4.23x10^{-3}$ and $b/c=1.13x10^{-3}$ plates, and alternating vortex streets for the $b/c=0.56x10^{-3}$ plate, were observed. The angle of attack and camber of the flexible airfoil determines the velocity outside the boundary layer at the separation point (trailing-edge). As the trailing-edge is a major source of shedding of vorticity at

zero freestream velocity, the amplitude and phase angle of the motion of the trailing-edge affect the strength and spacing of the vortices.

The strength of vortices is slightly larger for the $b/c=1.13x10^{-3}$ plate than the $b/c=4.23x10^{-3}$ plate, but there are substantial differences from the $b/c=0.56x10^{-3}$ plate, in particular at high frequencies. The airfoil flexibility has much more pronounced effect on the vortex spacing. The largest spacing is observed for the $b/c=1.13x10^{-3}$ plate whereas the smallest spacing is observed for the $b/c=0.56x10^{-3}$ plate. The calculated momentum flux is greatest for the $b/c=1.13x10^{-3}$ plate, followed by the $b/c=4.23x10^{-3}$ and $b/c=0.56x10^{-3}$ plates, implying that there is an optimum flexibility. There is a strong effect of heave amplitude on the circulation of vortices, time-averaged velocity, and vortex spacing. The calculated momentum flux indicates large influence of flexibility at small amplitudes.

Direct force measurements confirmed that at high heave frequencies the thrust coefficient of the airfoil with intermediate stiffness was greatest, although the least stiff airfoil can generate larger thrust at low frequencies. No regime was found in which the stiffest, essentially rigid, airfoil performed best. It is suggested that there is an optimum airfoil stiffness that maximises thrust for a given heave frequency and amplitude. The thrust/power input ratio was found to be greater for the flexible airfoils than for the rigid airfoil.

3.5 FIGURES

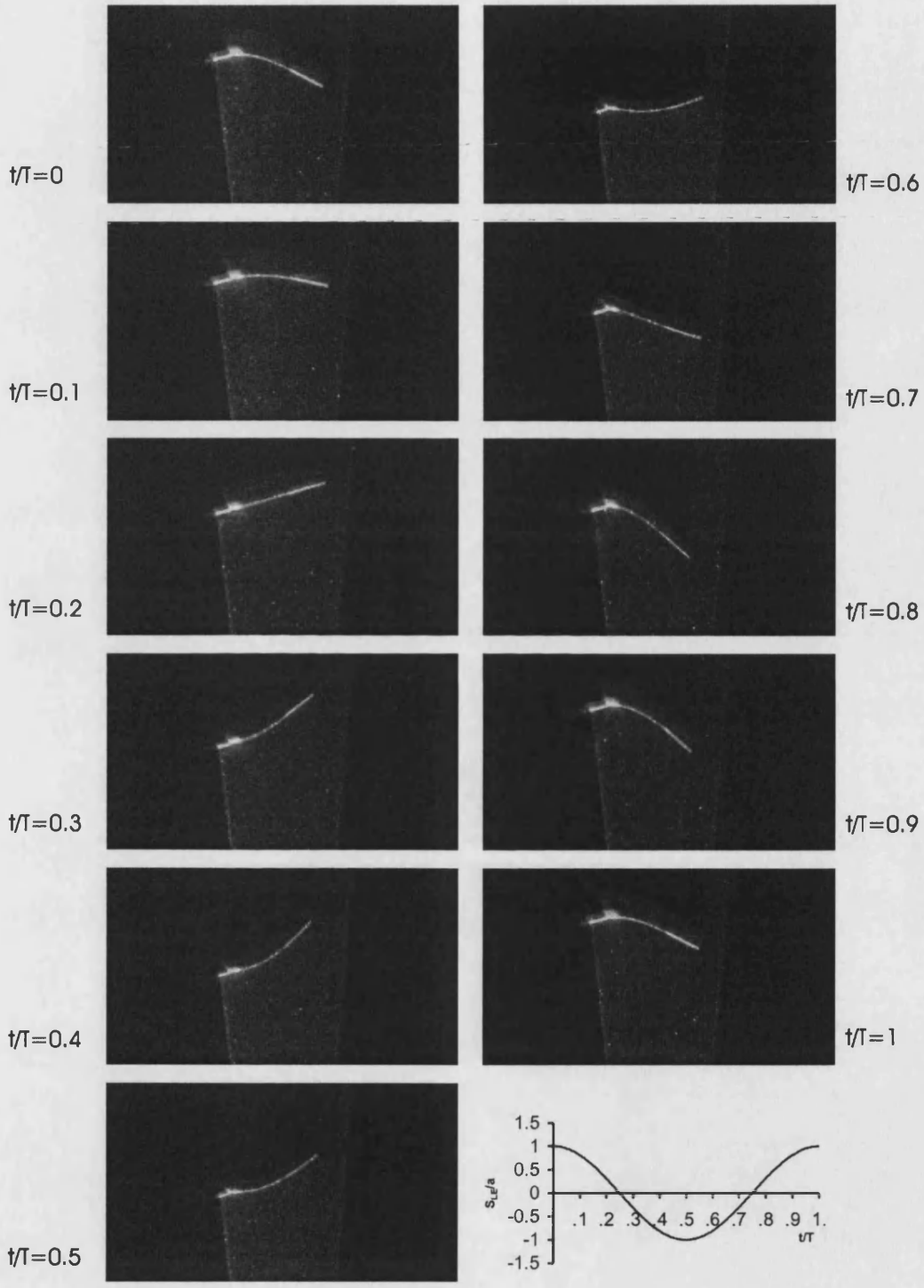

Figure 3.1: The shape of the very flexible airfoil over one period; Re_f=20,250, h=0.194.

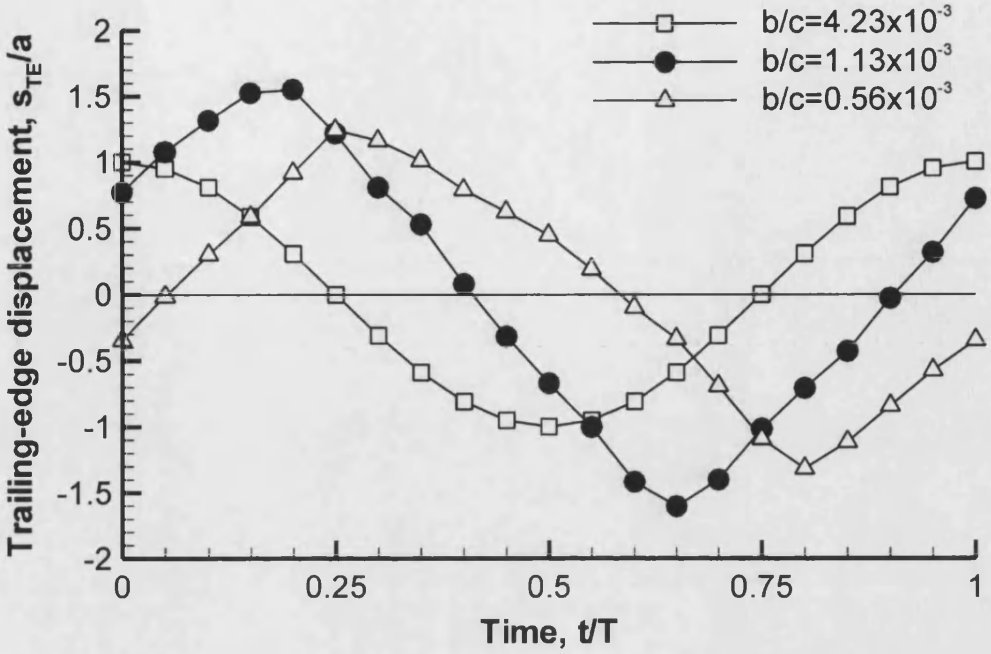

(a)

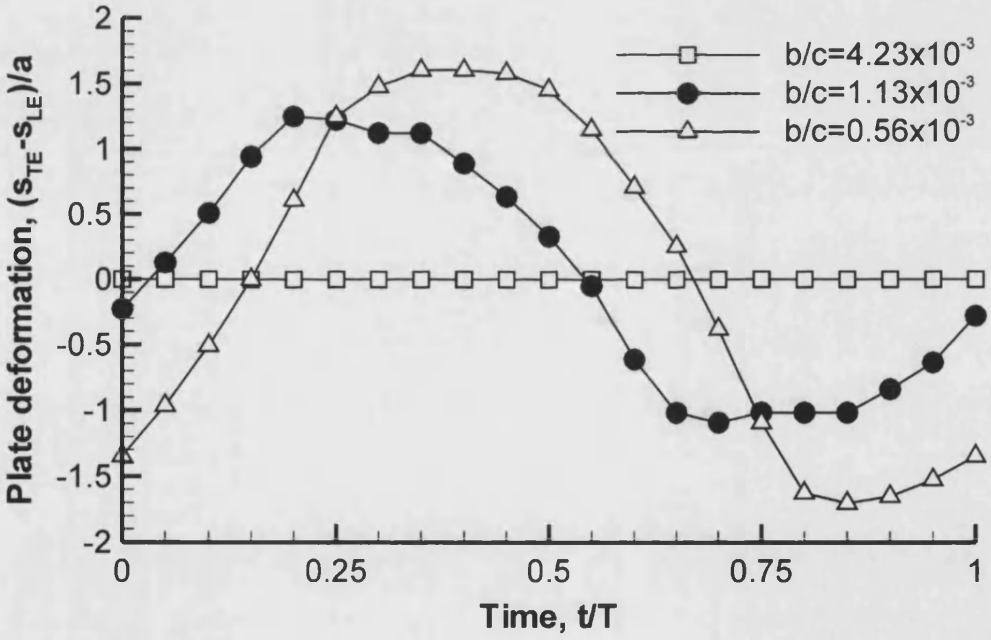

(b)

Figure 3.2: (a) Displacement of the trailing-edge and (b) displacement of the trailing-edge relative to the leading-edge; Re_f=20,250, h=0.194.

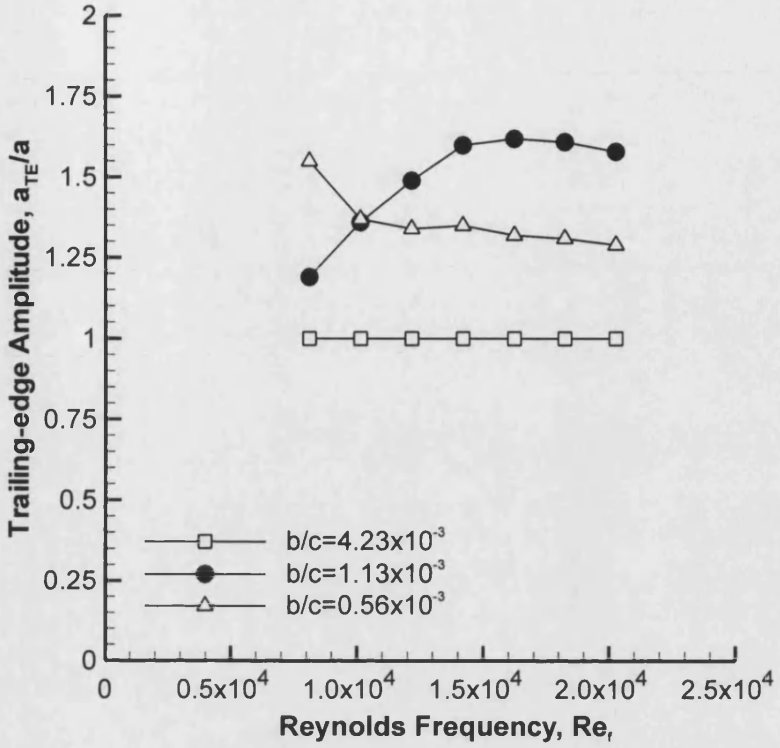

(a)

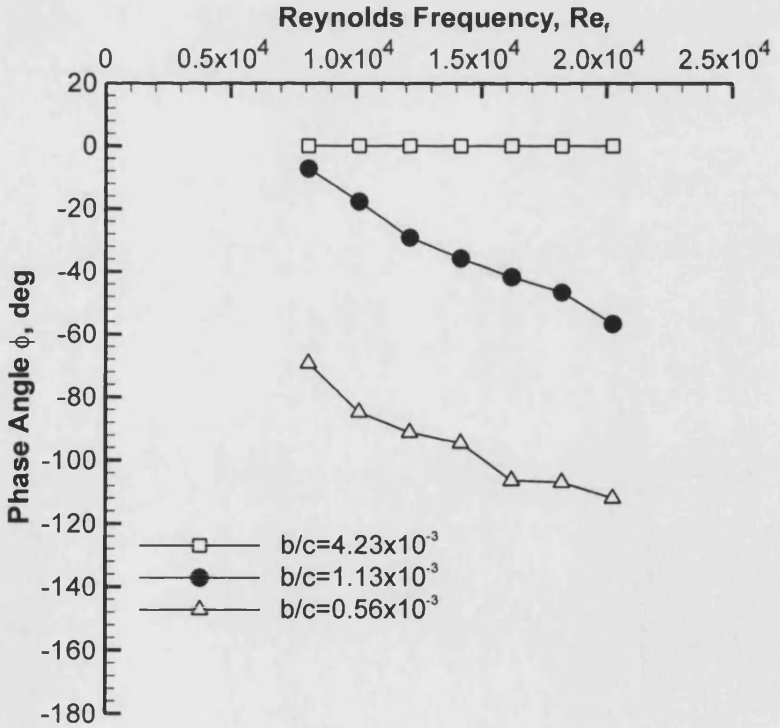

(b)

Figure 3.3: (a) Amplitude and (b) phase of S_{TE}/a as a function of Reynolds frequency; h=0.194.

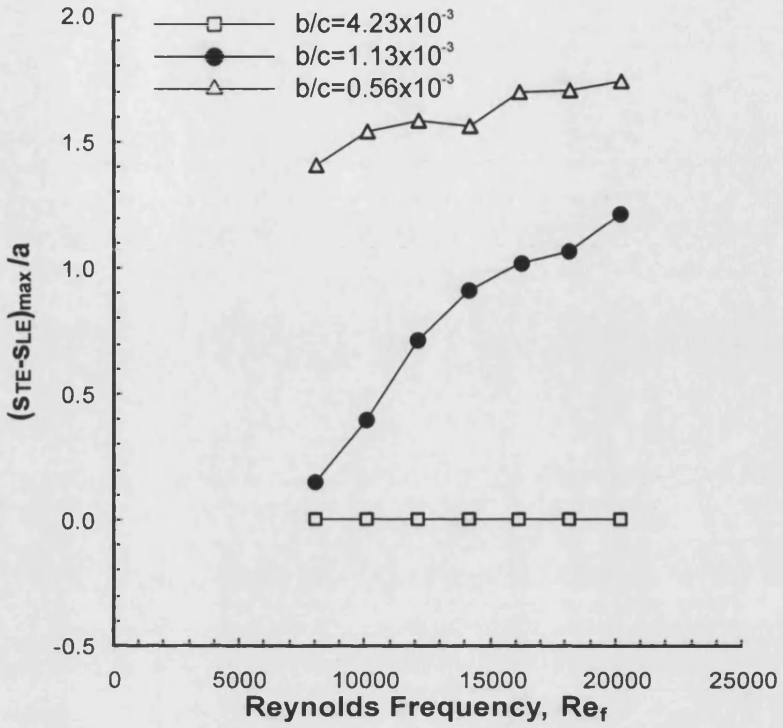

Figure 3.4: Amplitude of $(S_{TE}-S_{LE})/a$ as a function of Reynolds frequency; h=0.194.

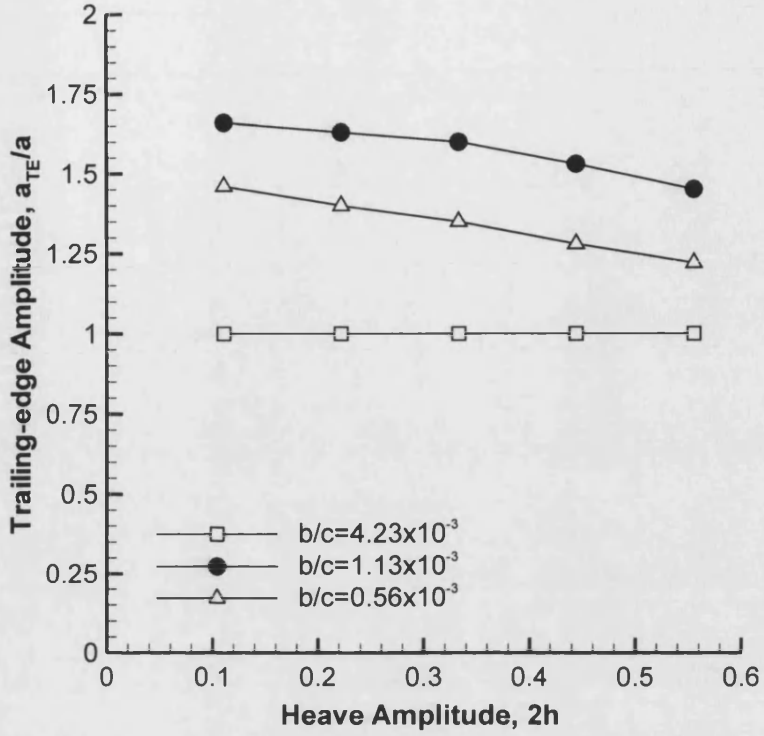

(a)

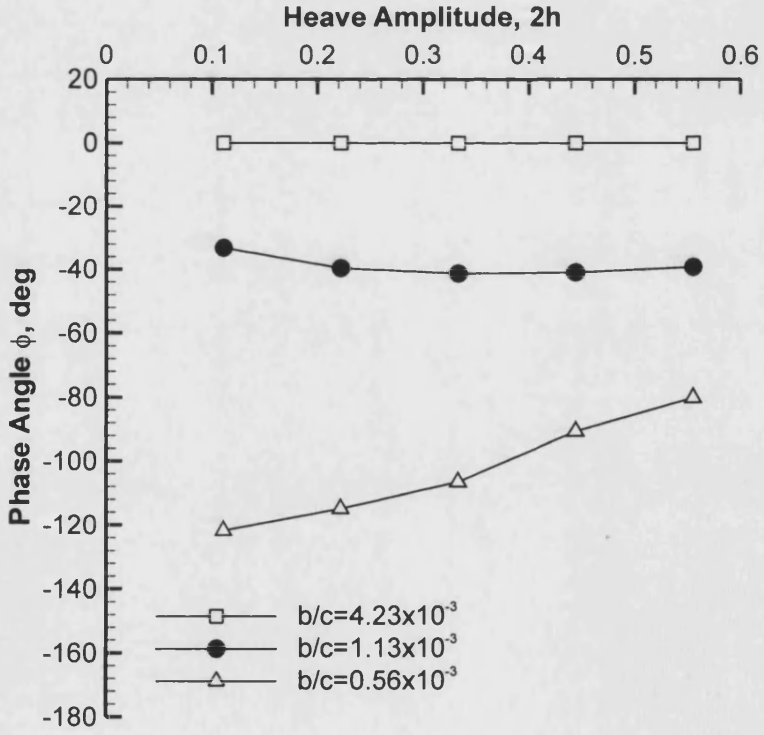

(b)

Figure 3.5: (a) Amplitude and (b) phase of S_{TE}/a as a function of heave amplitude; Re_f=16,200.

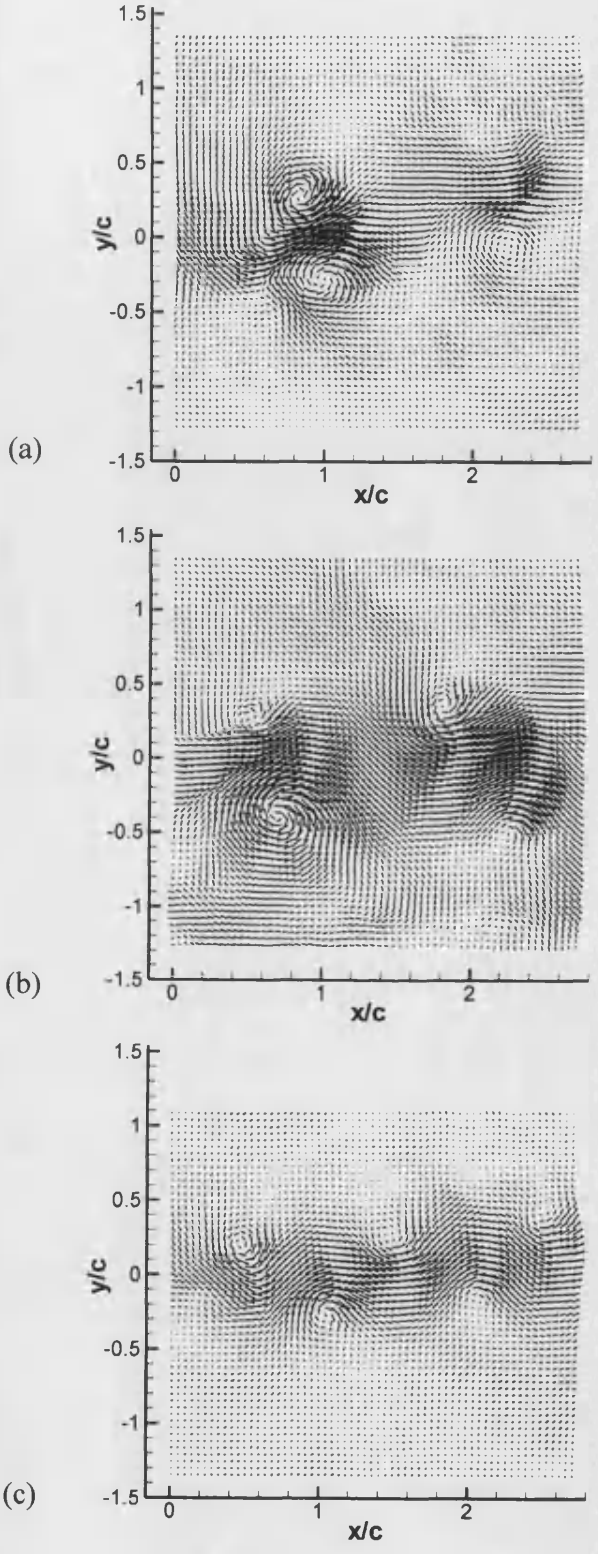

Figure 3.6: Instantaneous velocity field for (a) $b/c=4.23x10^{-3}$, (b) $b/c=1.13x10^{-3}$, and (c) $b/c=0.56x10^{-3}$; $Re_f=20,250$, $h=0.194$.

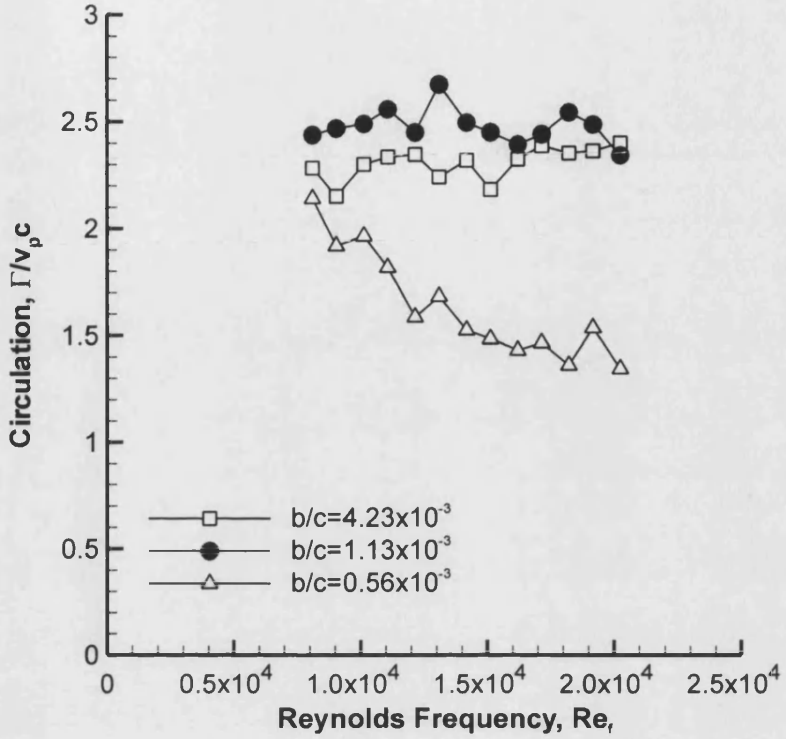

Figure 3.7: Variation of normalised circulation as a function of Reynolds frequency; h=0.194.

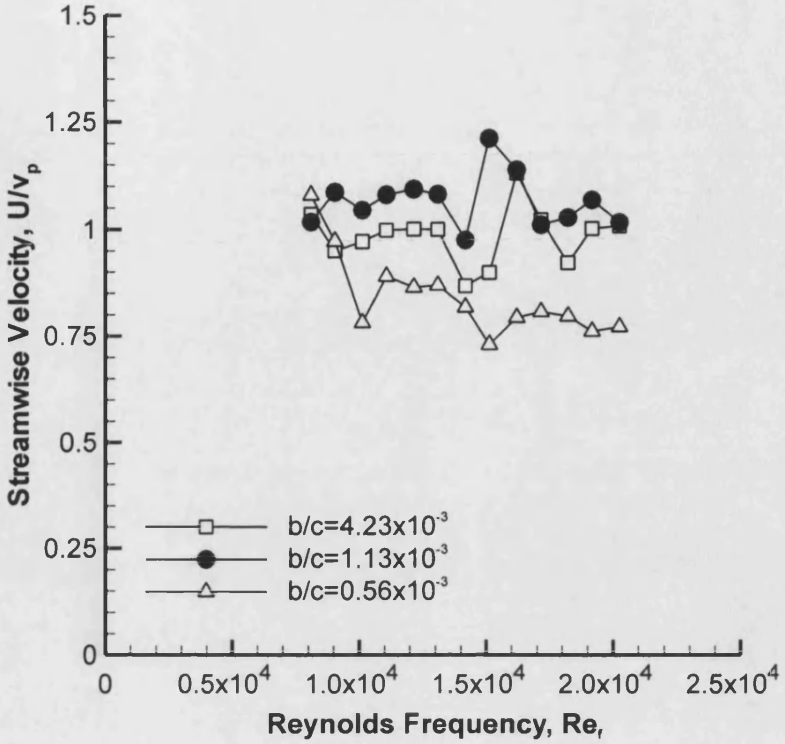

Figure 3.8: Variation of maximum time-averaged streamwise velocity as a function of Reynolds frequency; h=0.194.

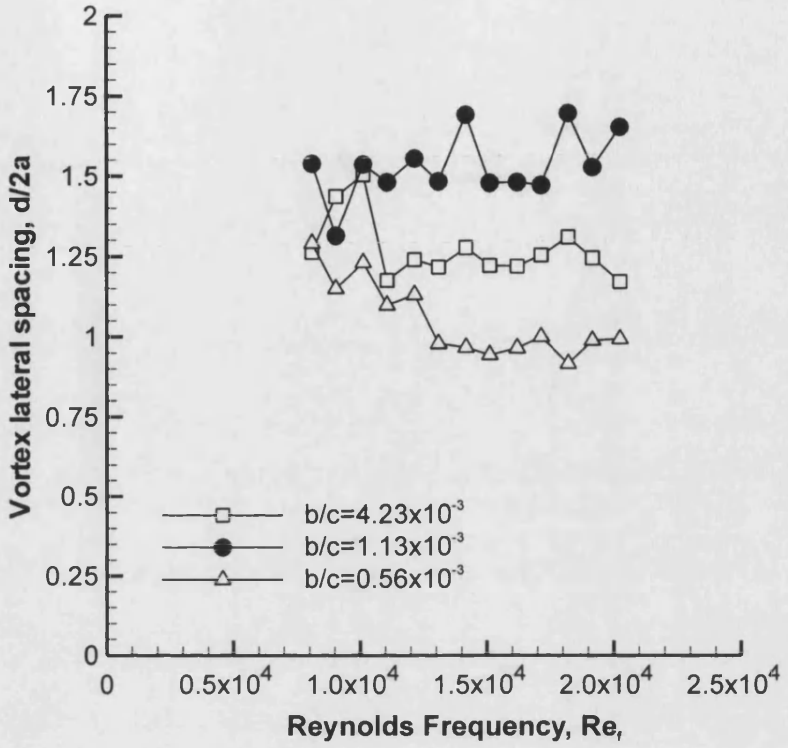

Figure 3.9: Variation of normalised lateral vortex spacing as a function of Reynolds frequency; h=0.194.

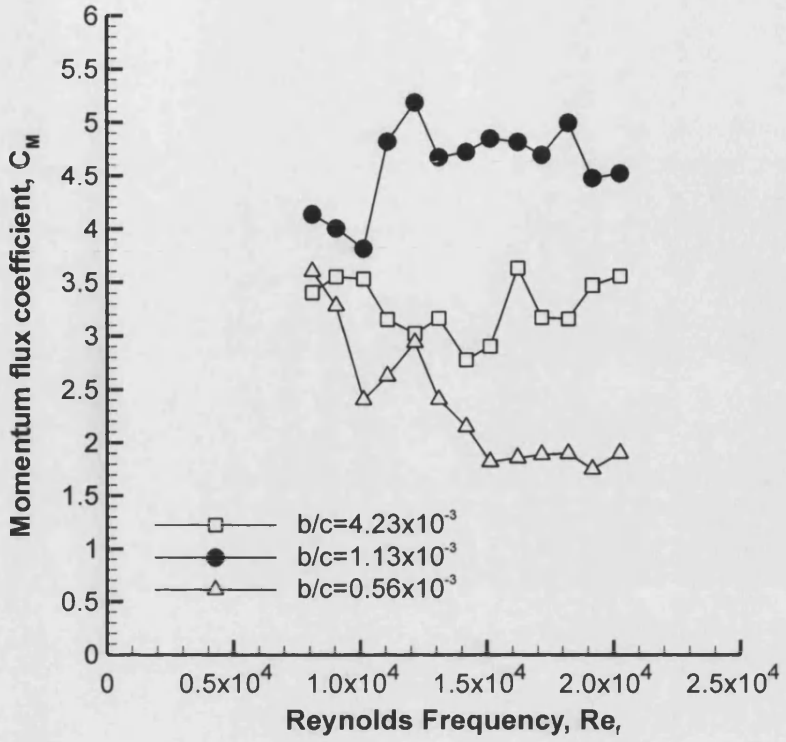

Figure 3.10: Momentum flux coefficient as a function of Reynolds frequency; h=0.194.

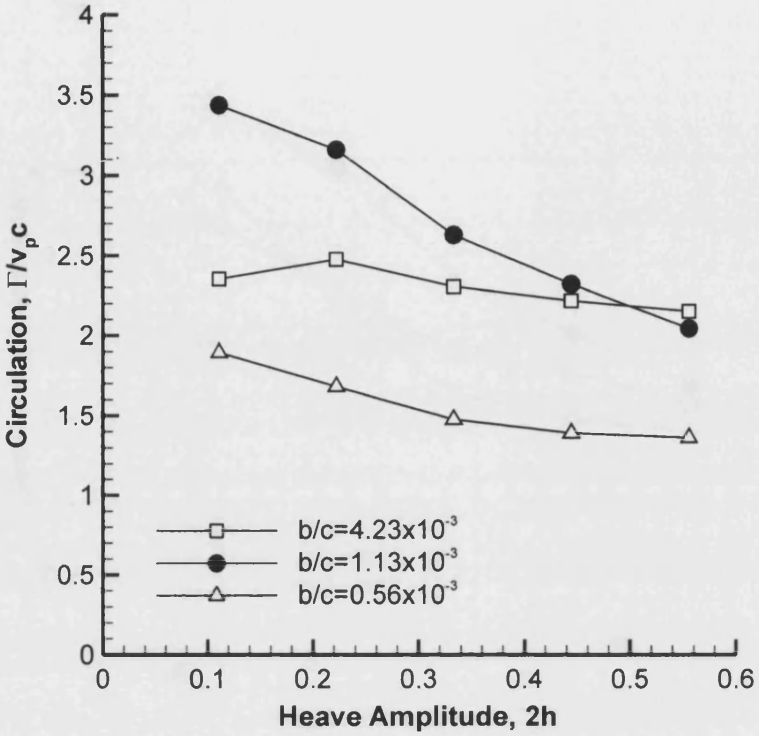

Figure 3.11: Variation of normalised circulation as a function of heave amplitude; Re_f=16,200.

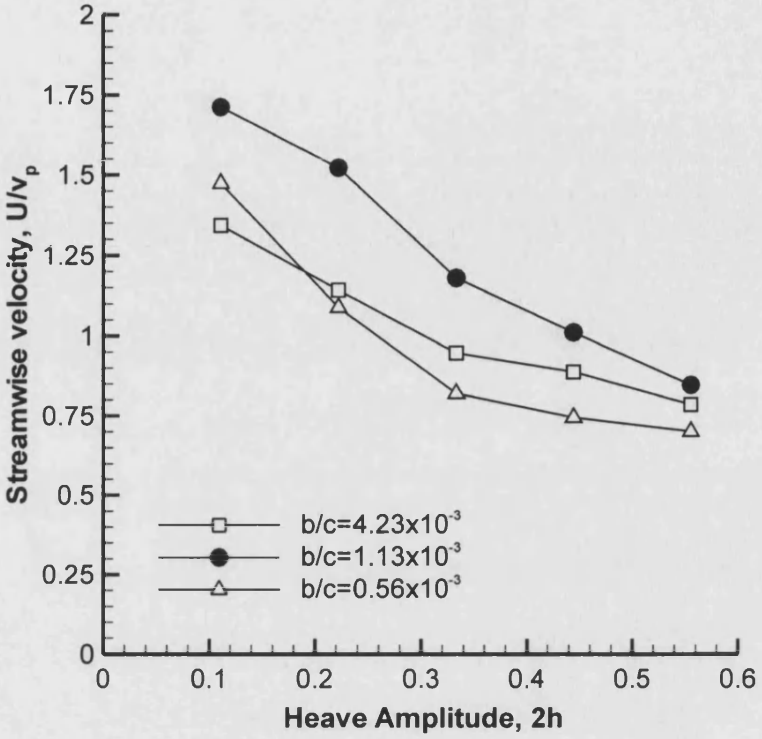

Figure 3.12: Variation of maximum time-averaged streamwise velocity as a function of heave amplitude; Re_f=16,200.

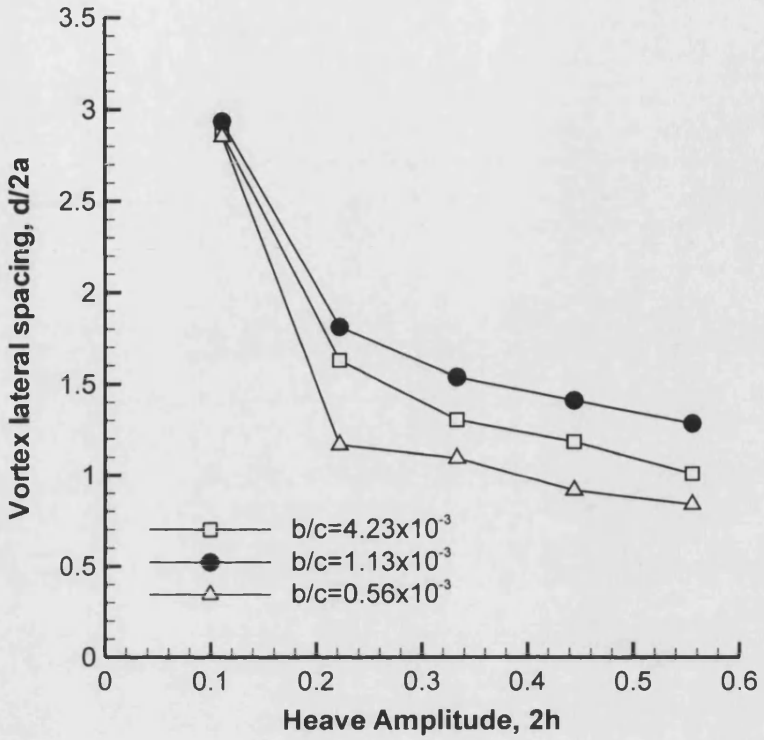

Figure 3.13: Variation of normalised lateral vortex spacing as a function of heave amplitude; Re_f=16,200.

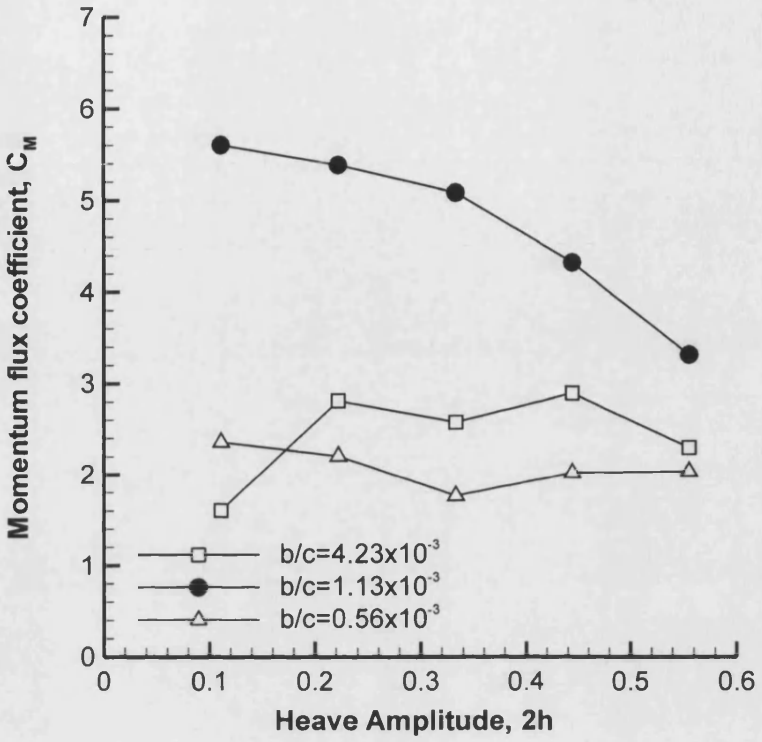

Figure 3.14: Momentum flux coefficient as a function of amplitude; Re_f=16,200.

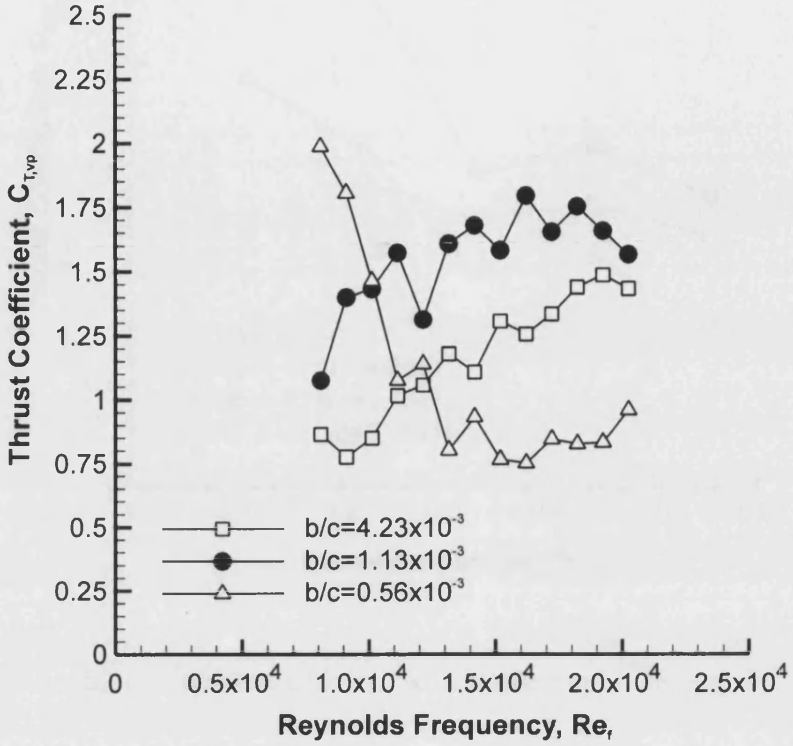

Figure 3.15: Variation of thrust coefficient with Reynolds frequency; h=0.194.

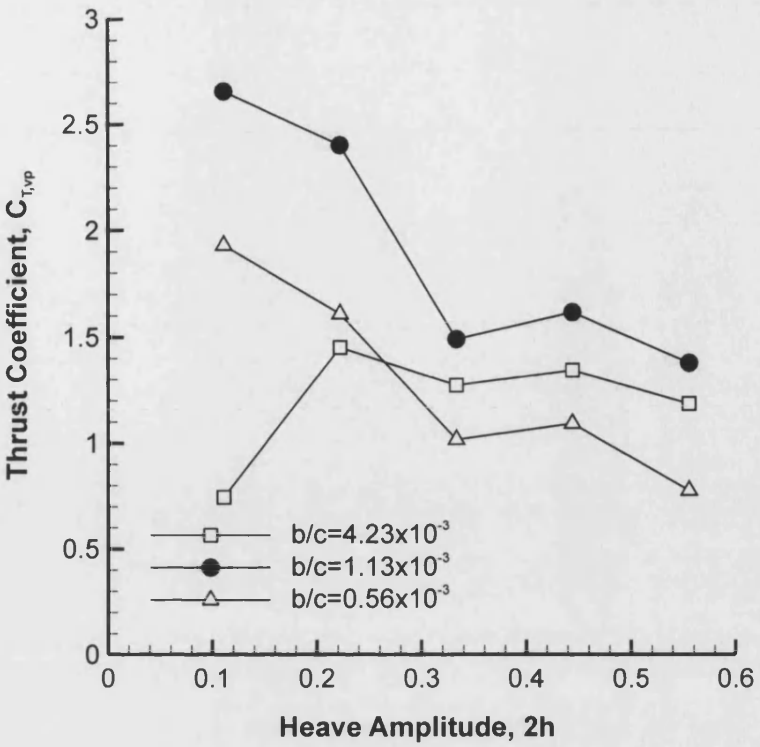

Figure 3.16: Variation of thrust coefficient with heave amplitude; Re_f=16,200.

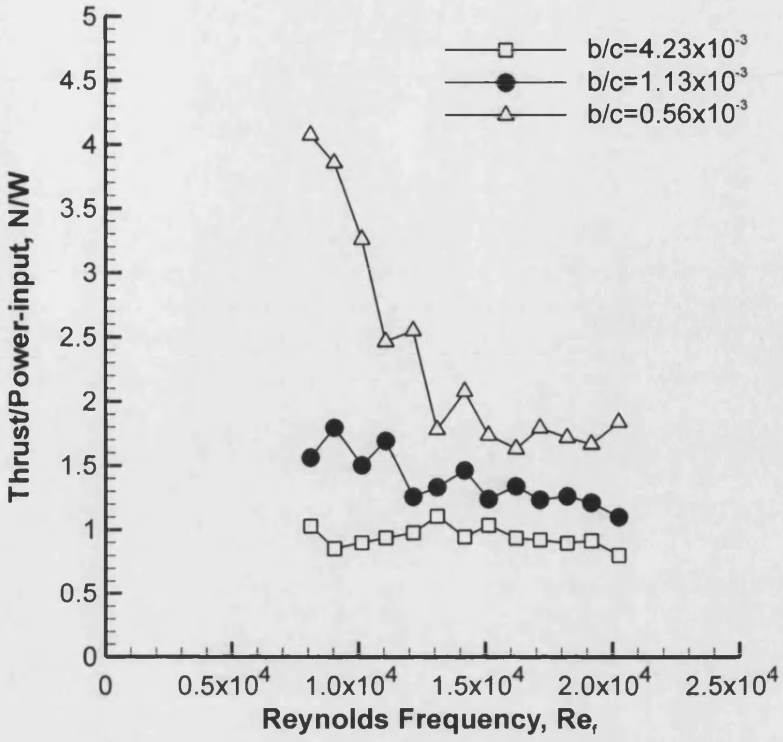

(a)

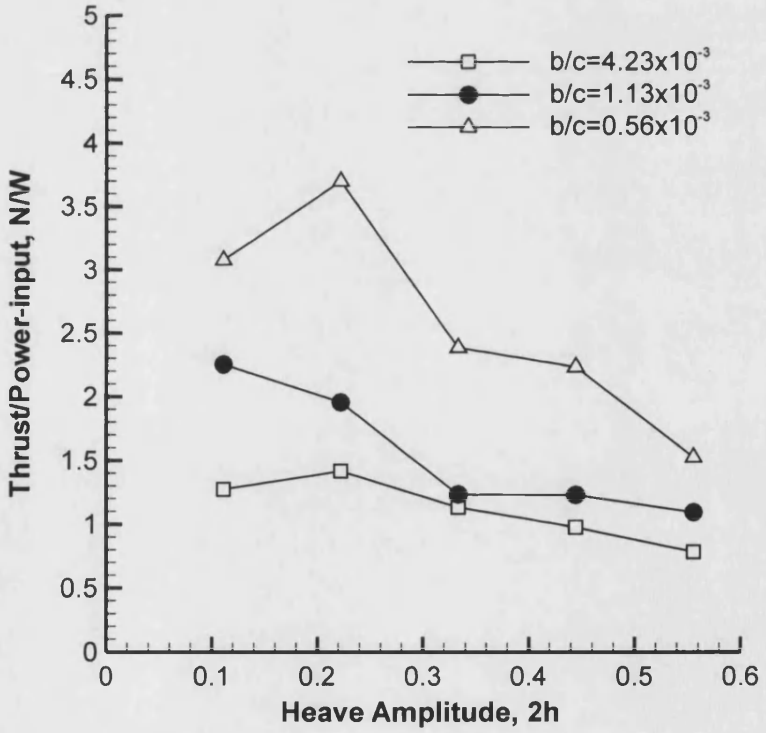

(b)

Figure 3.17: Thrust/power ratio as a function of (a) Reynolds frequency (h=0.194) and (b) amplitude (Re_f=16,200).

4 JET SWITCHING PHENOMENON

4.1 SUMMARY

An experimental investigation has been carried out on chordwise-flexible airfoils oscillating in still water and air. Both LDV and PIV measurements were taken over a range of airfoil flexibilities, heave frequencies and heave amplitudes. It was found that the vortex pairs generated by the oscillating airfoil move at an angle to the chordwise direction. The deflection angle of the induced jet was observed to change periodically in time. The switching period was found to increase with increasing airfoil stiffness and to decrease with heave frequency and amplitude. Over the range of frequency, amplitude and stiffness tested the switching period was found to be two orders of magnitude greater than the heave period. The development of the vorticity field for upward and downward deflected jets, as well as the transition between the two modes, was captured. Jet switching was still observed in experiments when the side walls were removed, indicating that wall effects are not responsible for the switching phenomenon. The deflection of the jet, and thus the jet switching effect, is found to diminish for non-zero freestream velocities. For Strouhal numbers less than 0.34, the deflections angles are found to be less than 6 degrees.

4.2 AIM

Lai and Platzer[24] found vortices from an airfoil in pure heave at high Strouhal numbers to be shed in pairs, and for axis of the vortex street to be inclined at an angle to the x-axis. Such *dual* modes had been observed twice before[13, 66] and have even been predicted in Navier-Stokes analyses of heaving airfoils[43]. Numerical analyses[13, 60, 67, 68] have suggested that whether the jet is inclined up or down

depends on the starting position of the airfoil. In their experiments, Jones, Dohring & Platzer[13] found the vortex street to, "alternate between modes somewhat randomly, suggesting that relatively small disturbances may trigger the switch." Jet switching has also been observed in Navier-Stokes simulations[17], although the frequency of the switching has not been discussed. The aim of this chapter is to present the findings of an experimental study of the jet switching phenomenon. With the exception of the final section, the experiments described in this chapter were carried out at zero freestream velocity, and therefore infinite Strouhal number.

4.3 RESULTS

4.3.1 LDV MEASUREMENTS

Figure 4.1 shows time history of normalised streamwise velocity for the $b/c=1.13x10^{-3}$ airfoil ($Re_f=18,225$, $h=0.11$). Since the freestream velocity is zero, the streamwise velocity is non-dimensionalised by dividing by the peak heave velocity. Measurements of streamwise velocity were taken at a point one chord length downstream and one half of one chord length above the x axis. Measurements were taken over 1200 oscillations. In Figure 4.1(a) the variation of streamwise velocity over the first 12 cycles is shown. In part (b) the variation of streamwise velocity over the first 12, and the following 108, cycles is shown. In part (c) the time axis spans all 1200 cycles.

Figure 4.1(a) shows that the streamwise velocity varies periodically for the first 12 cycles. The period of the variation in streamwise velocity is equal to the period of the heave motion. The peak in streamwise velocity is attributed to the passing of a single counter-clockwise vortex through the measurement location per heave cycle.

Figure 4.1(b) shows the first 120 cycles. The streamwise velocity is seen to oscillate with a period equal to that of the heave motion. However, it is seen that the pattern of Figure 4.1(a) does not continue beyond $t/T\approx17$: Both the amplitude and offset of the oscillation change with time. For example, at $t/T=10$ the amplitude is approximately 1 and the offset approximately 2. At $t/T=40$, the amplitude is approximately 0.1 and the offset approximately zero.

It will be seen later that at some times the axis of the row of vortices generated by the heaving airfoil is inclined at a positive angle to the x direction, and at other times a negative angle. At early times (t/T=0-17) the vortex cores must have passed close to the measurement point (x/c=1, y/c=0.5) whereas at later times (t/T=40-60) the vortex cores must have passed far away from the measurement point. The first condition corresponds to a positive jet deflection angle, the second to a negative jet deflection angle. The change in inclination of the jet from a heaving airfoil has been observed before[13, 24, 66]. In numerical simulations the direction of the jet has been shown to depend on the initial conditions (whether the airfoil first moved up or down). Water tunnel investigations have found that although the initial direction of the jet appears to be determined by the starting motion of the airfoil, the jet direction switches at random thereafter. Figure 4.1(c) shows the variation of streamwise velocity over a long time period. The time axis spans all 1200 oscillations of the airfoil. The peaks corresponding to the passage of individual vortices are very closely spaced and are not visible. It is seen that the moving-average velocity changes periodically, with a period two orders of magnitude greater than the period of the heave motion. This suggests that the angle of the jet changes sign periodically. This behaviour does not appear to have been observed before, either in experimental or numerical studies.

The experiment that yielded the data of Figure 4.1 was repeated for five heave frequencies and two heave amplitudes. Velocity measurements were taken over 1200 cycles. Periodic jet switching was observed in each case. The normalised switching frequency is plotted against Reynolds frequency for h=0.11 and h=0.22 in Figure 4.2. The figure shows that the switching frequency increases with increasing heave frequency and amplitude.

4.3.2 PIV MEASUREMENTS

Figure 4.3 shows six instantaneous velocity fields obtained from PIV measurements (Re_f=16,200, h=0.194). Parts (a) and (b) show the b/c=4.23x10^{-3} airfoil velocity field, parts (c) and (d) the b/c=1.13x10^{-3} airfoil velocity field and parts (e) and (f) the b/c=0.56x10^{-3} airfoil velocity field. In each case the airfoil is in its centre position (s=0) and moving downwards ($v=v_p$). The horizontal lines adjacent to the leading-

edge indicate, from bottom to top, the positions y=-a, y=0 and y=+a. In all cases, two vortices are shed per heave cycle. The velocity fields in parts (a), (c) and (e) were captured when the axis of the vortex street was inclined at a negative angle to the x axis. The velocity fields in parts (b), (d) and (f) were captured at a later time, when the axis of the vortex street was inclined at a positive angle to the x axis. It is seen that, for the $b/c=4.23x10^{-3}$ and $b/c=1.13x10^{-3}$ airfoils, a single vortex is present at the trailing-edge when the angle of the jet is negative, whereas a vortex pair is present at the trailing-edge of the airfoil when the angle of the jet is positive. In summary, it is seen that the jets from all three airfoils are in general deflected, and that the angle of the jet changes with time.

In order to study the time evolution of the vortices, two further sets of PIV experiments were carried out: phase-locked and phase-incremented.

Phase-locked PIV measurements

For each airfoil, and for a single Reynolds frequency (Re_f =16,200) and amplitude (h=0.194), two-hundred phase-locked velocity measurements were taken. The origin of time, t/T=0, was chosen to be the point at which the leading-edge of the airfoil moves through the mid point of the down stroke (as in Figure 4.3). The coordinates of the [upper] counter-clockwise and [lower] clockwise vortices are plotted against time in Figure 4.4 ($b/c=4.23x10^{-3}$ airfoil), Figure 4.5 ($b/c=1.13x10^{-3}$ airfoil) and Figure 4.6 ($0.56x10^{-3}$ airfoil). In part (a) the crosswise and streamwise location of the first counter-clockwise vortex is plotted as a function of time. In part (b) the crosswise and streamwise location of the first clockwise vortex is plotted as a function of time. In part (c) the location of both vortices is plotted in the x-y plane. The direction of increasing time is shown with arrows. The location of the trailing-edge of the airfoil is marked by the symbol 'x'. The trailing-edge of the $b/c=4.23x10^{-3}$ airfoil coincides with the origin of the coordinate system. The position of sequential counter-clockwise vortices is such that they trace a loop. Figure 4.4 may be interpreted as showing the existence of two vortex-shedding modes. In mode 1, which persists from t/T=80 to t/T=150, a single counter-clockwise vortex is present 0.2 chord lengths above the trailing-edge of the airfoil. A clockwise vortex is present below the x axis and approximately one chord length downstream. The jet is deflected down; a typical velocity field is shown in Figure 4.3(a). In mode 2, which persists from t/T=0 to

t/T=70, a vortex pair is present approximately 0.3 chord lengths downstream of the trailing-edge. The jet is deflected up; a typical velocity field is shown in Figure 4.3(b). The transition from one mode to the other occurs relatively quickly, over approximately 7 heave cycles.

Equivalent plots for the $b/c=1.13x10^{-3}$ airfoil are shown in Figure 4.5. Unlike the $b/c=4.23x10^{-3}$ airfoil case, the trailing-edge of the $b/c=1.13x10^{-3}$ airfoil is not coincident with the origin. Again, two modes are observed. In mode 1, a single vortex is present at the trailing-edge, and a second vortex much further downstream and approximately one half of a chord length below the x axis. The jet is deflected down; Figure 4.3(c) shows a typical velocity field. In mode 2, a vortex pair is present at the trailing-edge and the jet is deflected up; Figure 4.3(d) shows a typical velocity field. Whereas the period of the switch was around 150 heave cycles for the $b/c=4.23x10^{-3}$ airfoil, the period is nearly 80 cycles for the $b/c=1.13x10^{-3}$ airfoil. Because the switch cycle is shorter, it is possible to observe the periodicity of the switching. A second difference is that the transition between mode 1 and mode 2 and vice versa occurs more gradually. It is more difficult to say at which point the transition occurs. Whereas in the case of the $b/c=4.23x10^{-3}$ airfoil the clockwise vortex circumscribes a loop once over 200 oscillations (Figure 4.4(c)), two complete orbits are made in the case of the $b/c=1.13x10^{-3}$ airfoil (Figure 4.5(c)).

Similar behaviour is observed for the $0.56x10^{-3}$ airfoil (Figure 4.6). The period of the switch is similar to that of the $b/c=1.13x10^{-3}$ airfoil. There is a near sinusoidal variation in the streamwise position of the clockwise vortex, and for this reason it is more difficult to distinguish between mode 1 and mode 2.

Phase-incremented PIV measurements

In the second set of PIV measurements, measurements were taken at t/T = 0, $1\frac{1}{20}$, $2\frac{2}{20}$, $3\frac{3}{20}$... 21. Vorticity contours are shown in Figure 4.7, Figure 4.8, Figure 4.9, Figure 4.10, and Figure 4.11 (Re_f =16,200, h=0.194). In Figure 4.7, the vorticity field at normalised time intervals of $1\frac{1}{20}$ is shown. In this way a pseudo time history of the vortex formation and convection process is constructed. Regions of negative vorticity (counter-clockwise vortices) are shown black, zero vorticity is shown grey and

positive vorticity (clockwise vortices) is shown white. It is seen that mode 1 is characterised by the formation of a single vortex on the down stroke, followed by the formation of a vortex of opposite sign on the upstroke. Near the end of the cycle the vortex pair moves downstream and produces a downward deflected jet.

Figure 4.8 shows the vorticity field for mode 2. It is seen that a clockwise vortex is already present at the trailing-edge at the beginning of the down stroke. During the down stroke an counter-clockwise vortex forms. Near the end of the down stroke the vortex pair moves downstream. A single vortex forms on the upstroke. It is seen that the down stroke in mode 2 is the mirror image of the upstroke in mode 1. Up to this point, mode 1 has been described as the mode in which a single vortex exists at the trailing-edge during the down stroke, and mode 2 the one in which a vortex pair exists. It is seen that a better description is as follows: mode 1 is the mode in which a single vortex exists at the trailing-edge during the down stroke; mode 2 is the mode in which a single vortex exists at the trailing-edge during the upstroke. In this way it is seen that mode 2 is the mirror image of mode 1.

The transition from mode 1 to mode 2 is shown in Figure 4.9. Those in Figure 4.9 link the sequences of images in Figure 4.7 and Figure 4.8: the first frame in Figure 4.9 is the last frame in Figure 4.7, and the last frame in Figure 4.9 is the first frame in Figure 4.8.

Figure 4.10 and Figure 4.11 show abridged sequences for each airfoil. The leading-edge of the airfoil is shown in five consecutive positions: s=+a, s=0, s=-a, s=0, s=+a. Figure 4.10 shows mode 1 vorticity fields. It is seen that the vortices form later in the cycle for the $b/c=1.13\times10^{-3}$ airfoil, and later still for the 0.56×10^{-3} airfoil. For example, the counter-clockwise vortex formed during the down stroke is only visible for the 0.56×10^{-3} airfoil when the leading-edge reaches s=-a, whereas for the $b/c=4.23\times10^{-3}$ airfoil it is visible from the beginning of the oscillation. It is seen that, as expected, the 0.56×10^{-3} plate deforms the most. The 0.56×10^{-3} plate is also curved at all points in the cycle, unlike the $b/c=1.13\times10^{-3}$ plate. For completeness, mode 2 is shown in Figure 4.11.

In order to establish whether the periodic switching phenomenon is due to wall effects, the tank was removed and the airfoil oscillated in air. The setup is shown schematically in Figure 2.3. With the exception of the four pillars of the test rig, there were no obstacles in the x-y plane for a distance of 40 chord lengths in any direction. Smoke was released two chord lengths upstream of the trailing-edge for the $b/c=4.23x10^{-3}$ airfoil. The axis of the pipe was parallel to the span of the airfoil, so that the streamwise velocity component of the smoke was zero. Smoke was observed to be drawn downstream and exhausted at the trailing-edge in columns. Two instantaneous photographs of the smoke pattern are shown in Figure 4.12. It is seen that the vortex jet in the top picture is deflected up, and that the vortex jet in the bottom picture is deflected down. The direction of the jet was observed to change periodically, suggesting that the switching phenomenon is not due to wall effects.

4.3.3 EFFECT OF FREESTREAM VELOCITY

In order to assess the effect of freestream velocity, PIV experiments were carried out in a water tunnel for Reynolds numbers of 9000, 18000, and 27000. Experiments were performed at a Reynolds frequency of $Re_f=15800$ (f=1.95Hz), giving rise to Strouhal numbers of St=0.68 (Re=9000), St=0.34 (Re=18000), and St=0.23 (Re=27000). The peak jet deflection angle is plotted in Figure 4.13 for the three airfoils. It is seen that the maximum angle of the jet falls rapidly with increasing freestream velocity. Also, the deflection angle is seen to be less for the flexible airfoils. The deflection angle is seen to be small (less than 6 degrees) for Strouhal numbers of 0.34 and 0.23. For comparison, Jones et al.[13], report deflected jets for a NACA0012 airfoil in pure heave to occur when the Strouhal number exceeds a value of approximately 0.35.

4.4 CONCLUSIONS

Series of LDV, PIV, and smoke flow visualisation experiments were carried out for three airfoils. One of the airfoils was rigid, the other two flexible. The airfoils were oscillated in heave in water (LDV and PIV experiments) and in air (smoke flow experiments).

The vortex street generated by an airfoil heaving in fluid at rest was found to generally lie at an angle to the chord (x) direction. The jet-deflected-up vortex formation process was observed to be the mirror image of the jet-deflected-down

vortex formation process. The angle of such deflected jets was observed to change periodically. Deflected jets have been observed before in experimental and numerical simulations. Random jet switching has been observed in previous experiments and a single change in direction has been reported in a Navier-Stokes simulation. It is believed that the periodic jet switching observed in the present experiment has not been reported previously in the literature. The switching period was found to depend on the heave frequency and amplitude and the stiffness of the airfoil; in general, the switching period increased with increasing airfoil stiffness and decreasing heave frequency and heave amplitude. Over the ranges of stiffness, frequency and amplitude tested, the switching period was found to be two orders of magnitude greater than the heave period. Jet switching was still observed in pseudo 2D open-air smoke flow visualisation experiments, indicating that wall effects are not responsible for the switching phenomenon. The deflection of the jet, and thus the jet switching effect, is found to diminish for non-zero freestream velocities. For Strouhal numbers less than 0.34, the deflections angles are found to be less than 6 degrees.

4.5 FIGURES

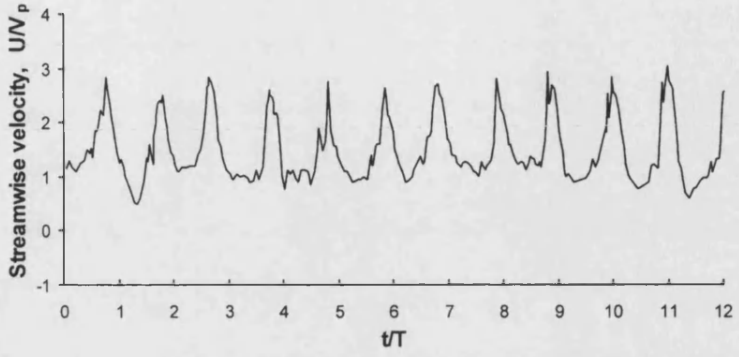

(a)

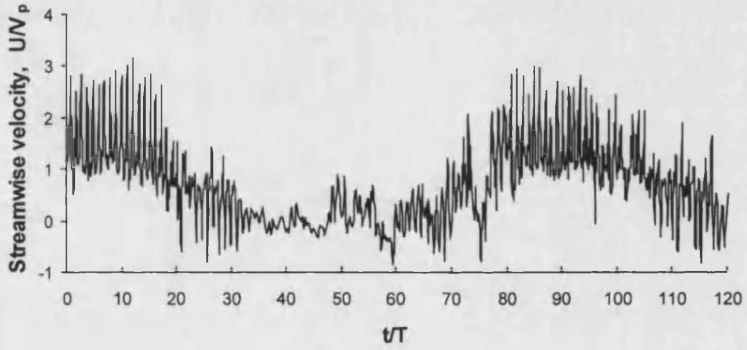

(b)

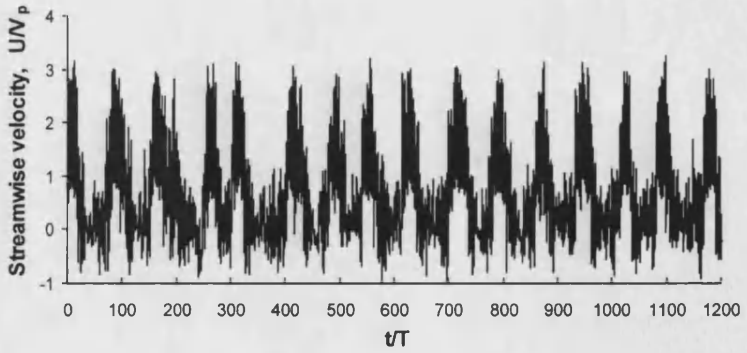

(c)

Figure 4.1: Time history of streamwise velocity component; b/c=1.13x10^{-3}, Re_f=18,225, h=0.11, x/c=1, y/c=0.5. (a) First 12 cycles; (b) First 120 cycles; (c) All 1200 cycles.

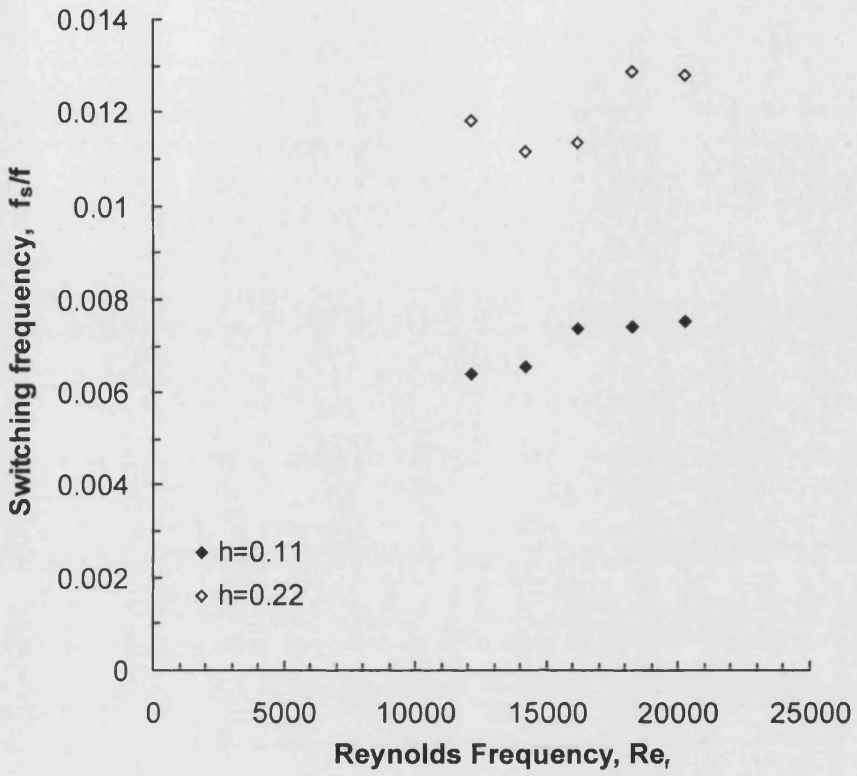

Figure 4.2: Jet switching frequency as a function of Reynolds frequency; $b/c=1.13x10^{-3}$.

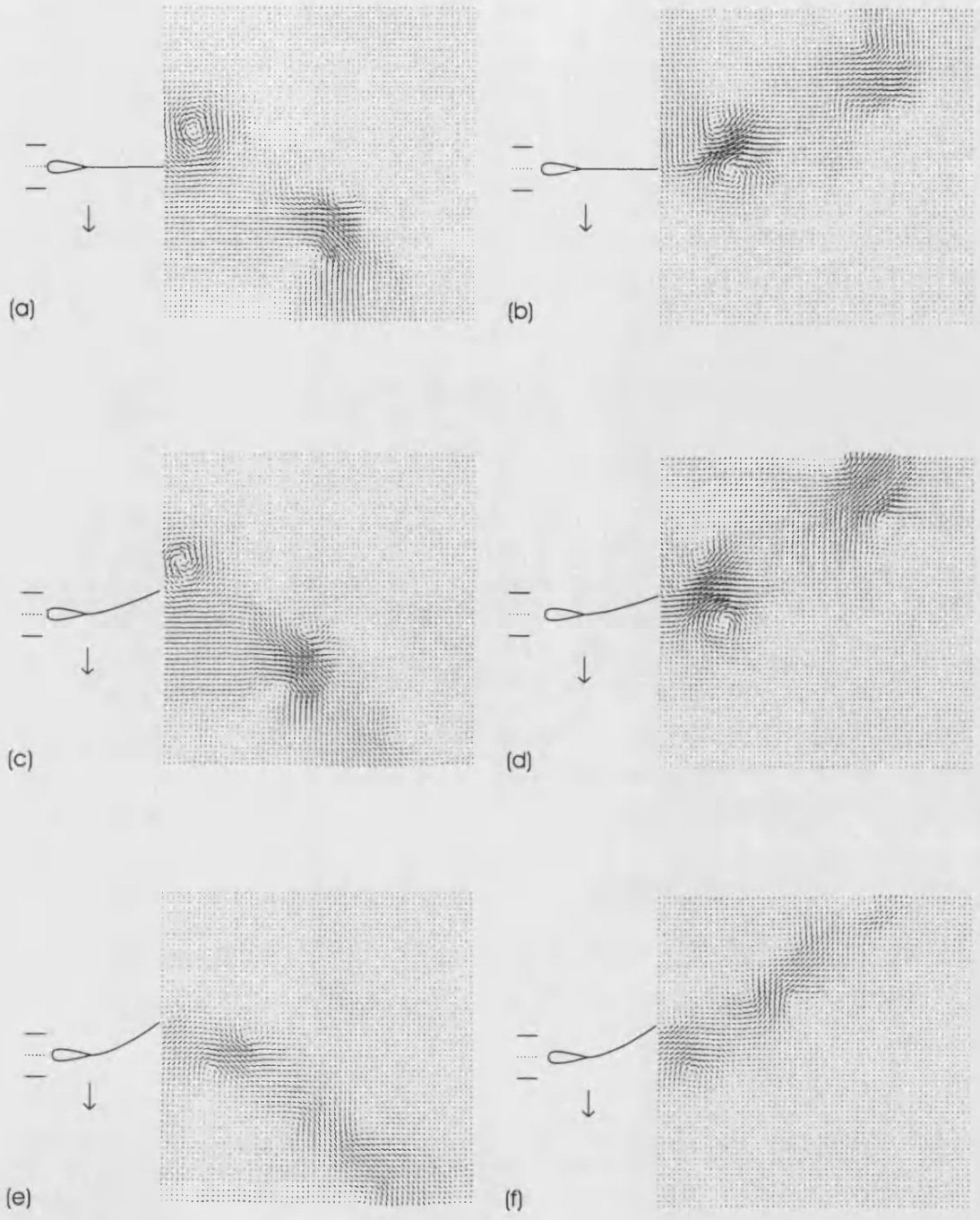

Figure 4.3: Instantaneous velocity fields; Re_f=16,200, h=0.194. (a) b/c=4.23x10^{-3}, jet deflected down; (b) b/c=4.23x10^{-3}, jet deflected up; (c) b/c=1.13x10^{-3}, jet deflected down (d) b/c=1.13x10^{-3}, jet deflected up; (e) b/c=0.56x10^{-3}, jet deflected down (f) b/c=0.56x10^{-3}, jet deflected up.

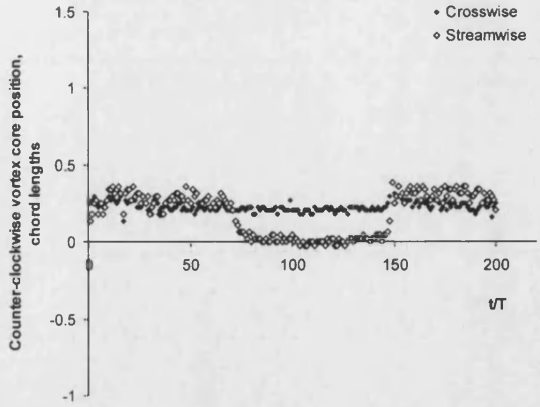

(a)

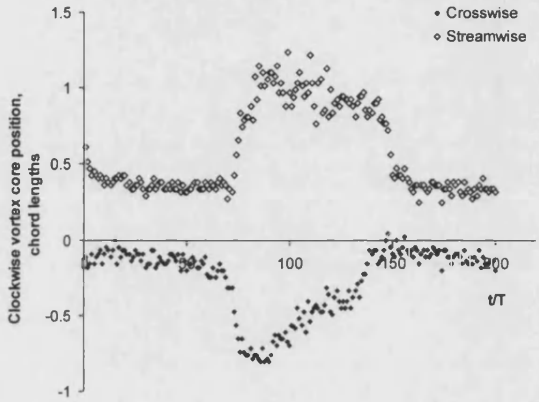

(b)

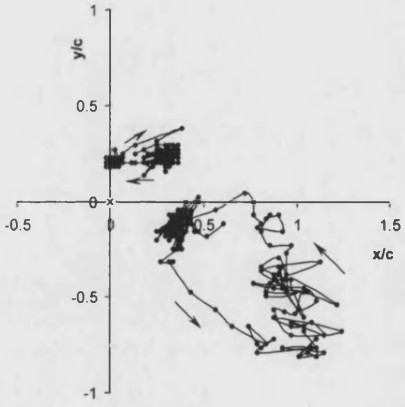

(c)

Figure 4.4: The location of the first two vortices at consecutive times at which the b/c=4.23x10^{-3} airfoil moves through the centre point of the down stroke; Re_f=16,200, h=0.194. (a) Coordinates of the first counter-clockwise vortex as a function of time; (b) Coordinates of the first clockwise vortex as a function of time; (c) Position of the core of the counter-clockwise vortex (top), and of the clockwise vortex (bottom) plotted in the x-y plane. The direction of time is shown by the arrows.

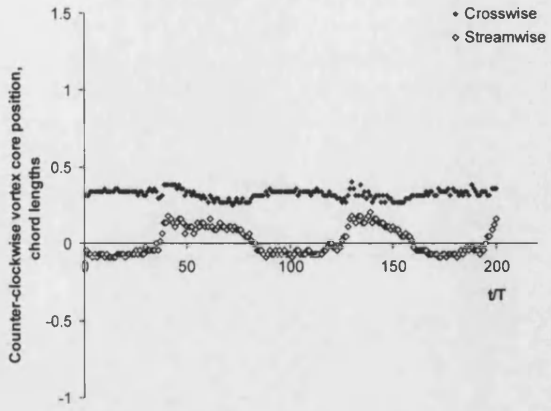

(a)

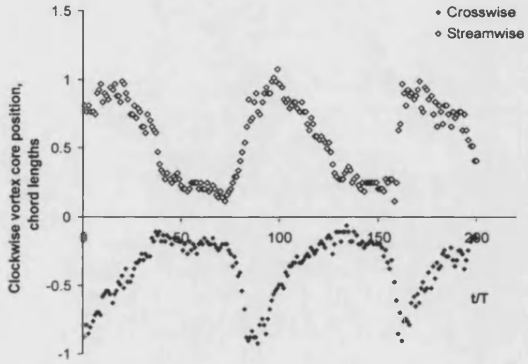

(b)

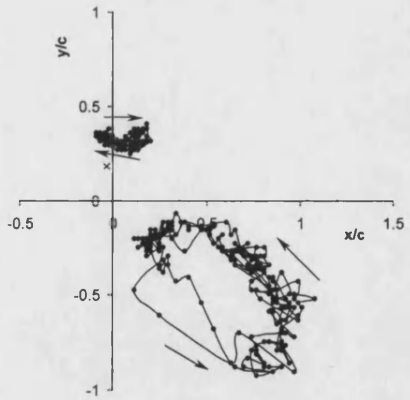

(c)

Figure 4.5: The location of the first two vortices at consecutive times at which the b/c=1.13x10^{-3} airfoil moves through the centre point of the down stroke; Re_f=16,200, h=0.194. (a) Coordinates of the first counter-clockwise vortex as a function of time; (b) Coordinates of the first clockwise vortex as a function of time; (c) Position of the core of the counter-clockwise vortex (top), and of the clockwise vortex (bottom) plotted in the x-y plane.

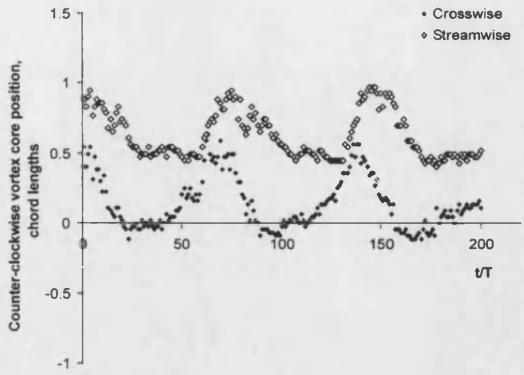

(a)

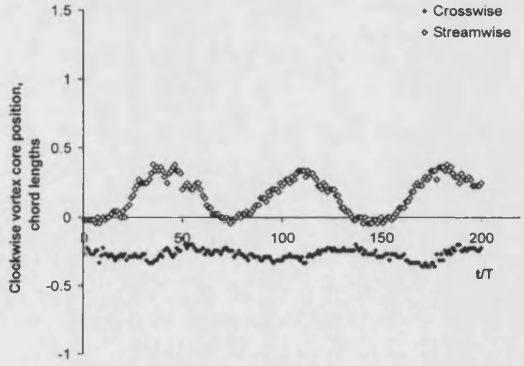

(b)

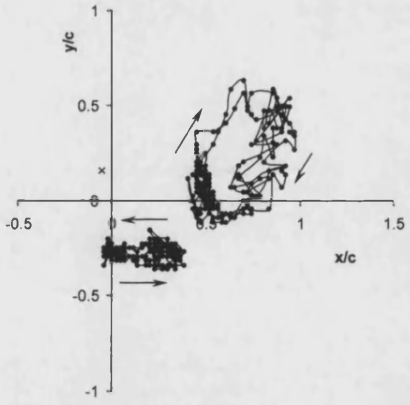

(c)

Figure 4.6: The location of the first two vortices at consecutive times at which the b/c=0.56x10^{-3} airfoil moves through the centre point of the down stroke; Re_f=16,200, h=0.194. (a) Coordinates of the first counter-clockwise vortex as a function of time; (b) Coordinates of the first clockwise vortex as a function of time; (c) Position of the core of the counter-clockwise vortex (top), and of the clockwise vortex (bottom) plotted in the x-y plane.

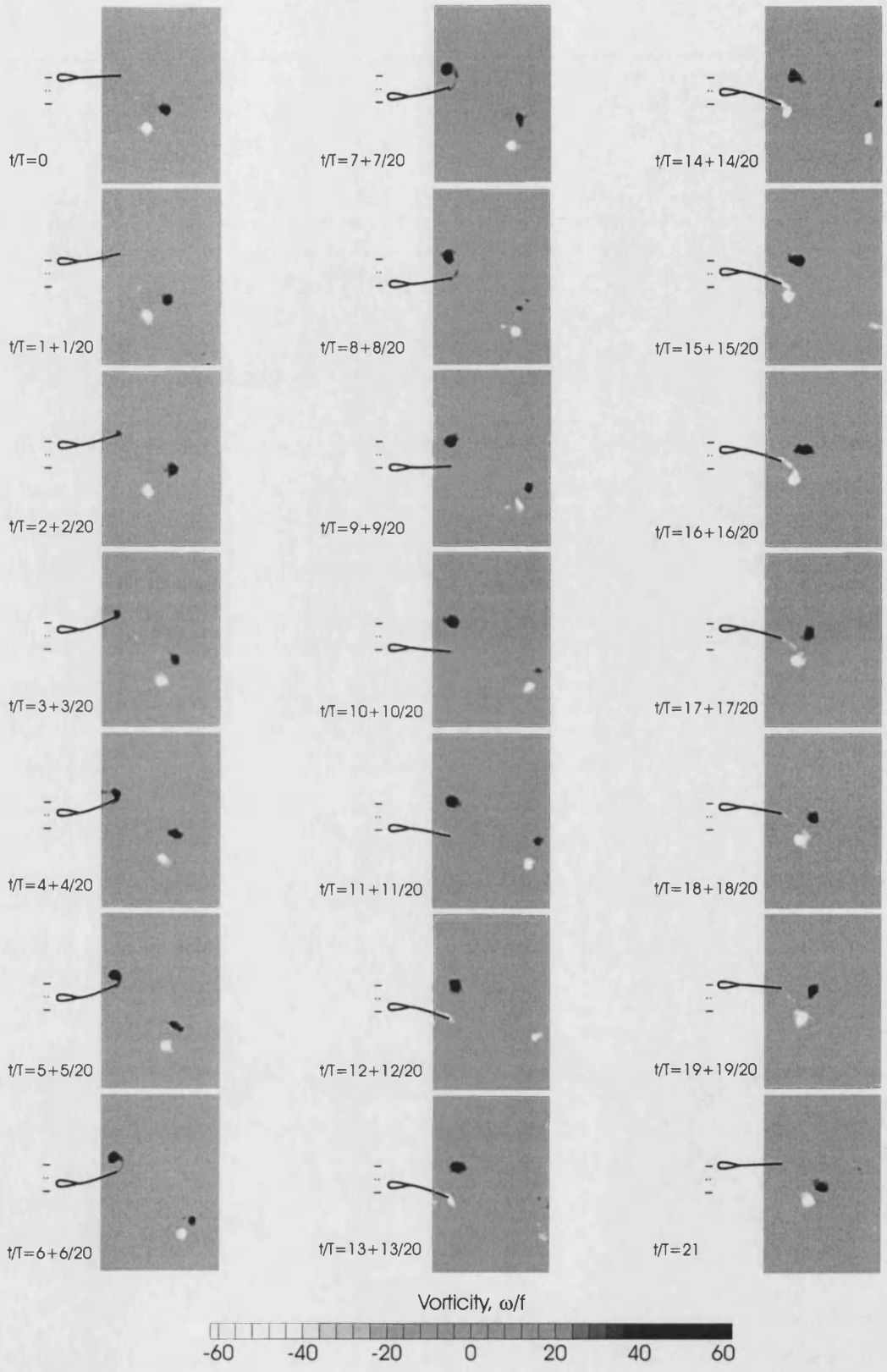

Figure 4.7: Time evolution of the mode 1 vorticity field; $b/c=1.13\times10^{-3}$, $Re_f=16{,}200$, $h=0.194$.

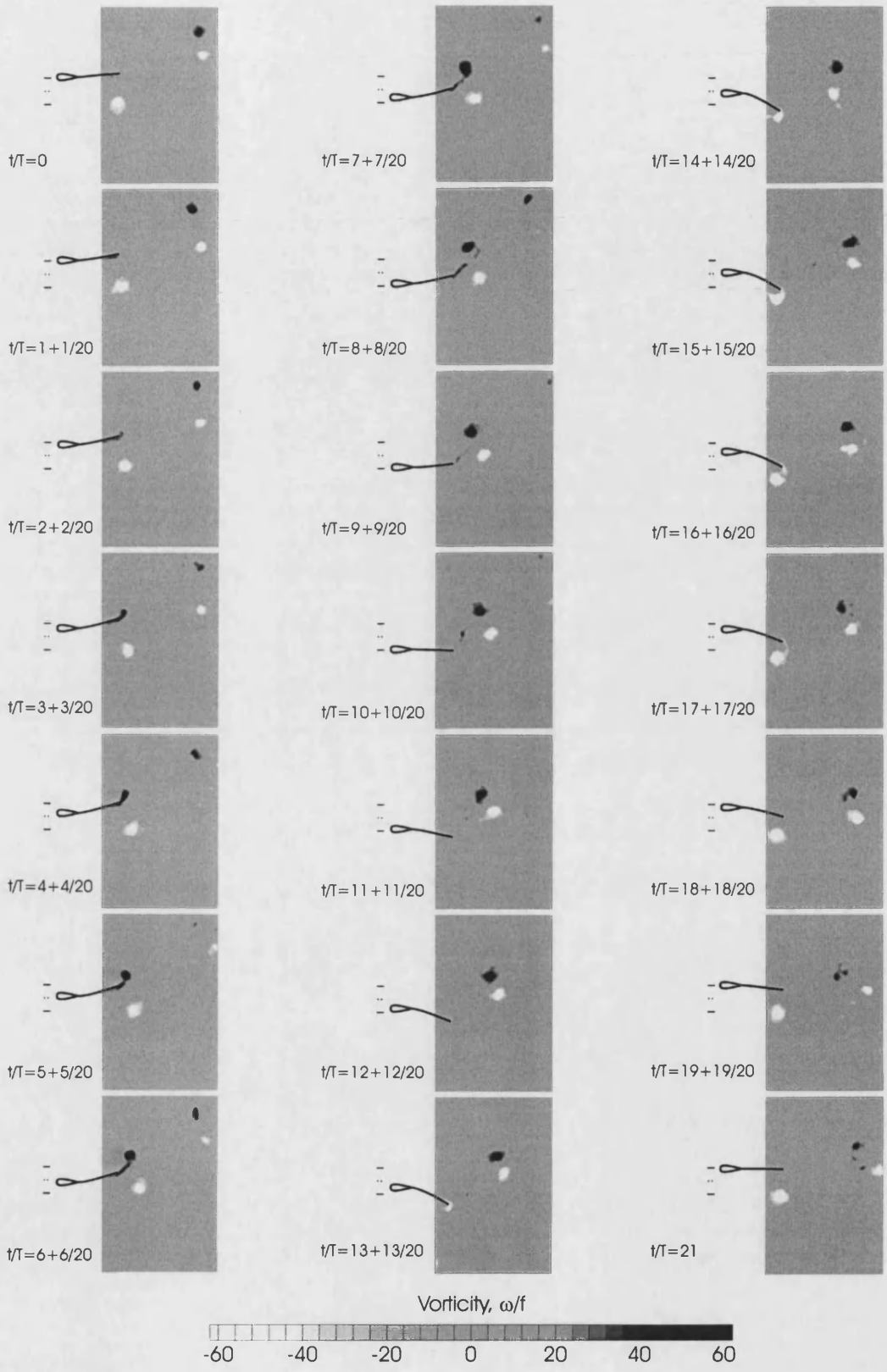

Figure 4.8: Time evolution of the mode 2 vorticity field; $b/c=1.13\times10^{-3}$, $Re_f=16{,}200$, $h=0.194$.

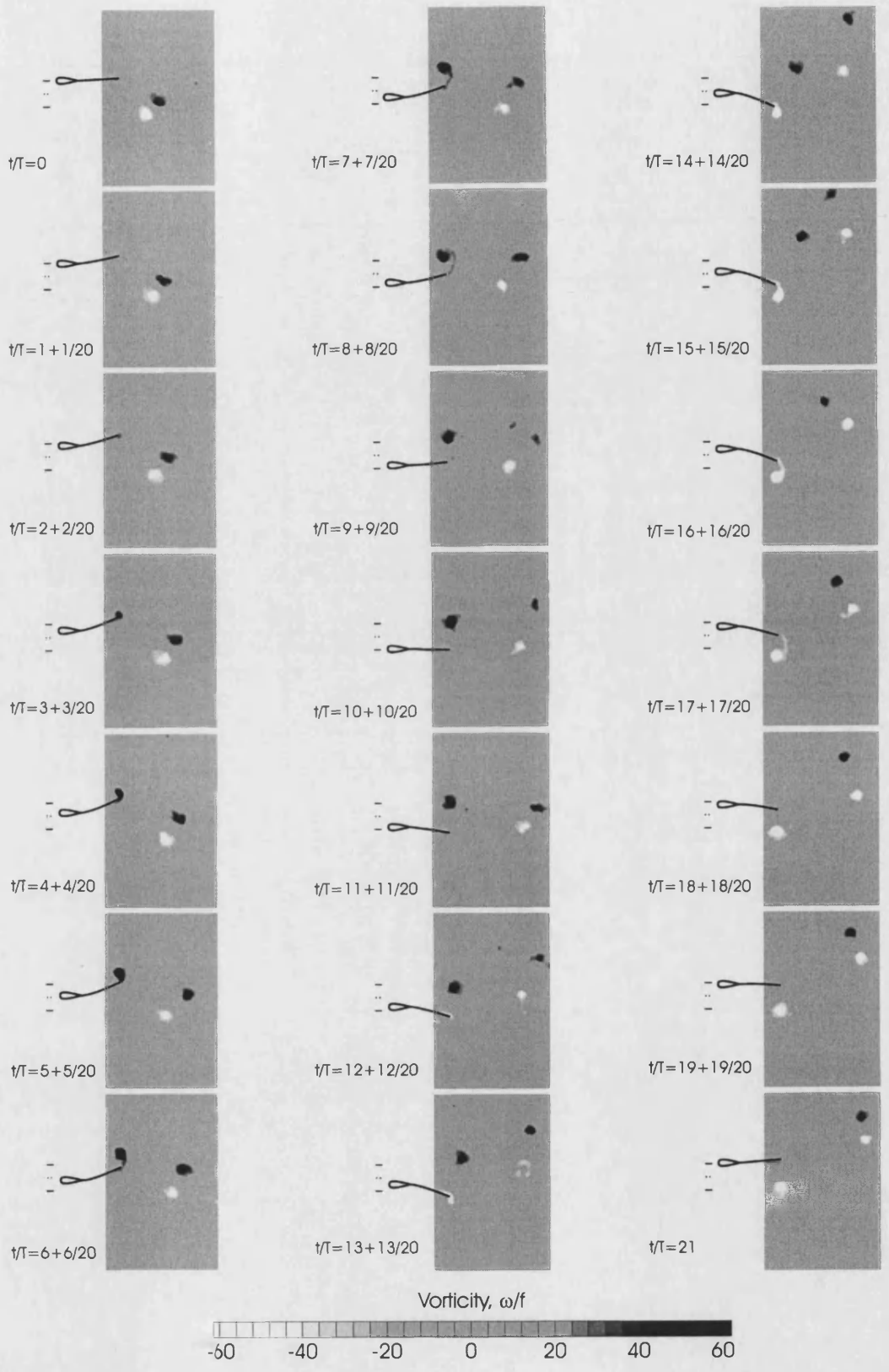

Figure 4.9: Transition from mode 1 to mode 2; b/c=1.13x10^{-3}, Re_f=16,200, h=0.194.

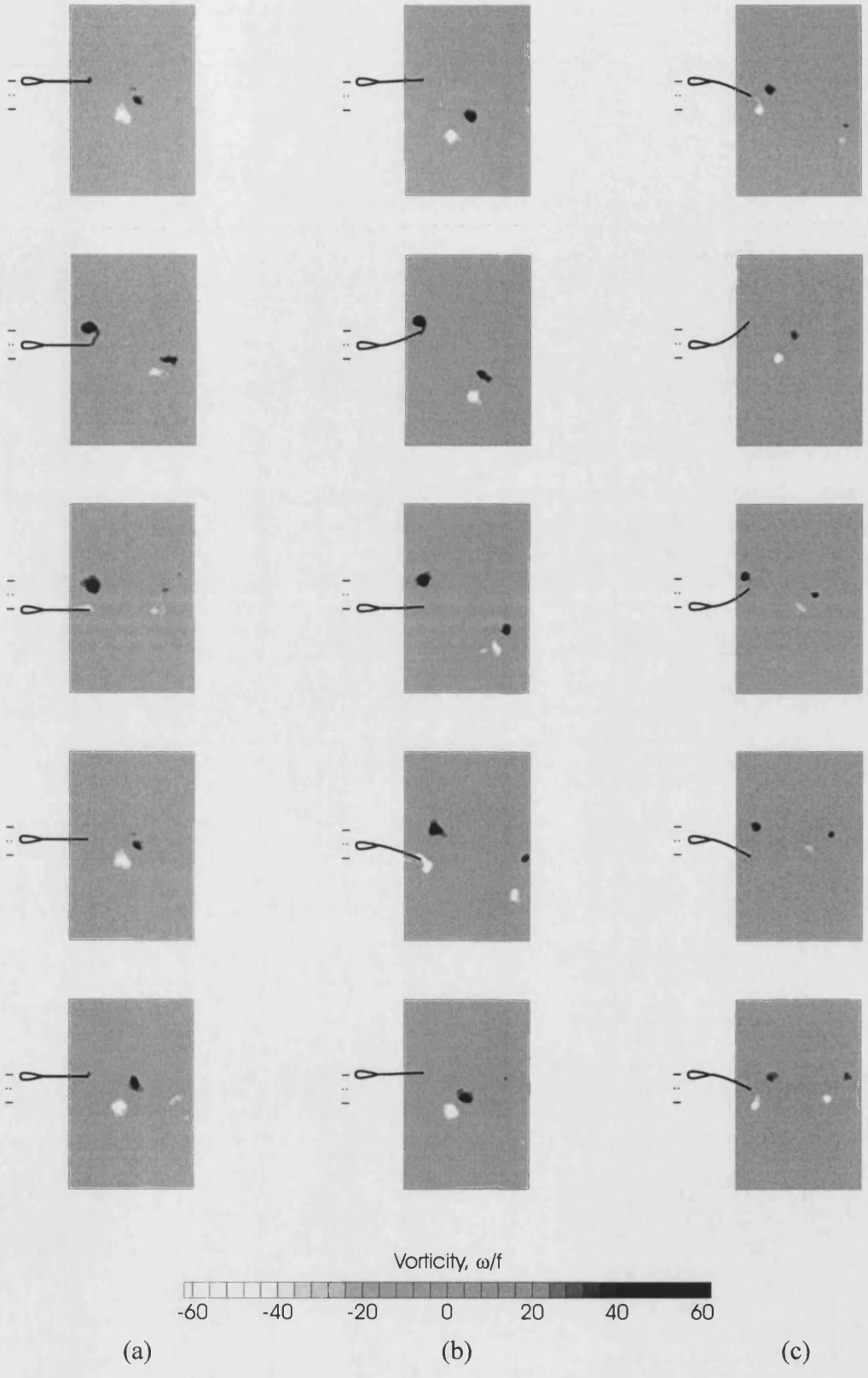

Figure 4.10: Abridged mode 1 vorticity fields; Re_f=16,200, h=0.194; (a) b/c=4.23x10^{-3}; (b) b/c=1.13x10^{-3}; (c) b/c=0.56x10^{-3}.

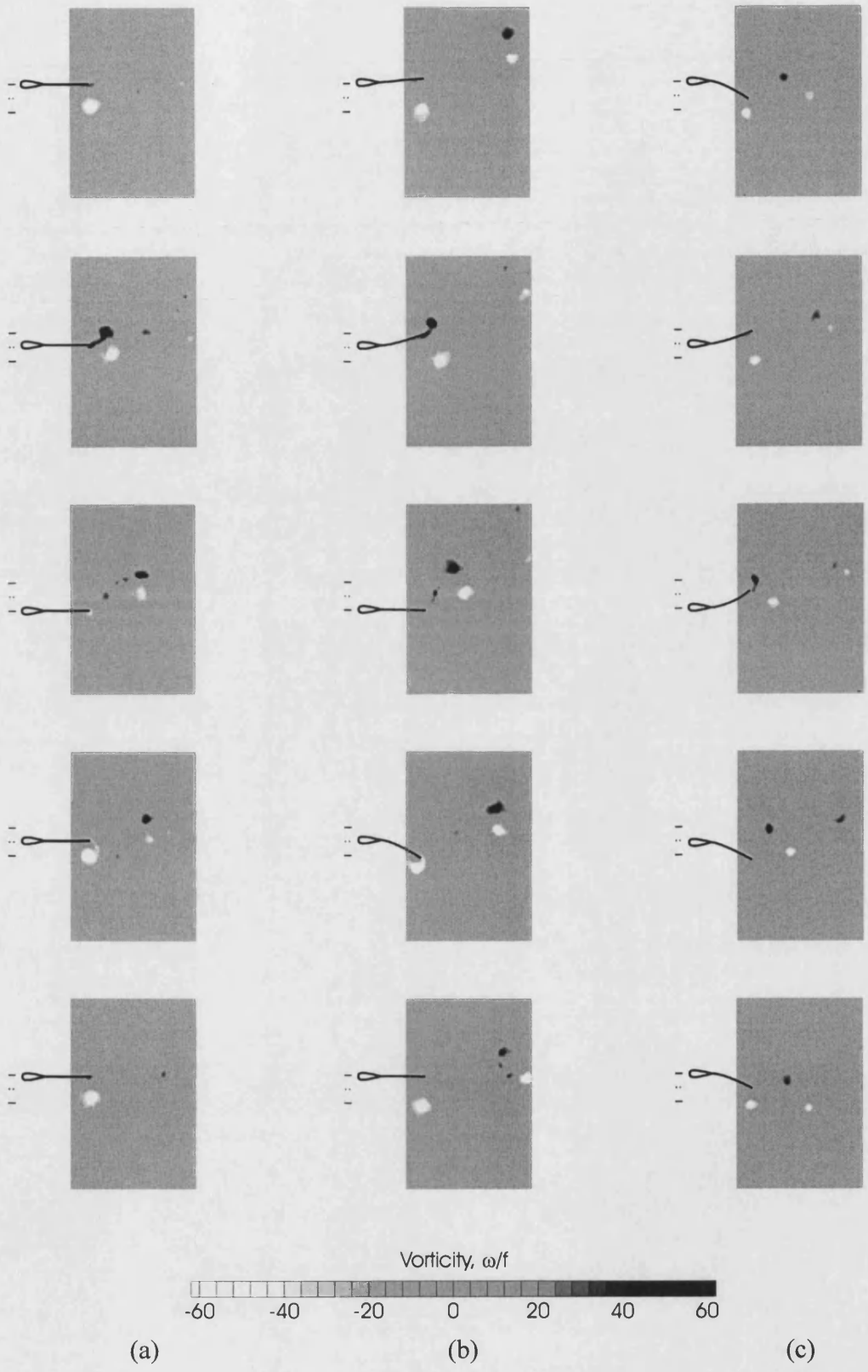

Figure 4.11: Abridged mode 2 vorticity fields; Re_f=16,200, h=0.194; (a) b/c=4.23x10^{-3}; (b) b/c=1.13x10^{-3}; (c) b/c=0.56x10^{-3}.

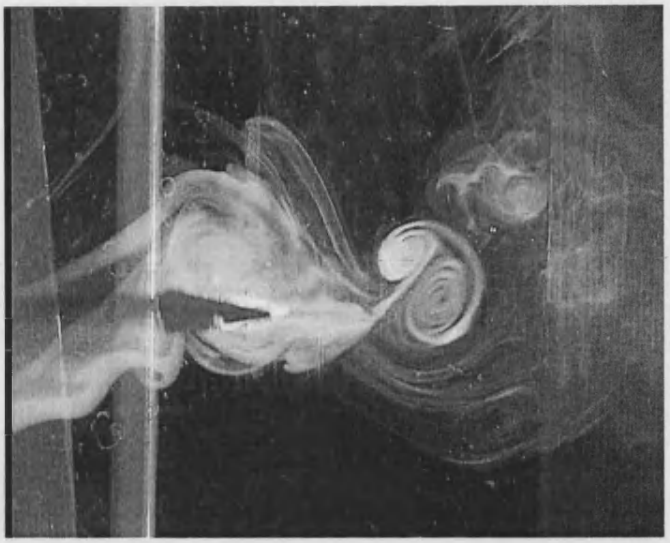

(a)

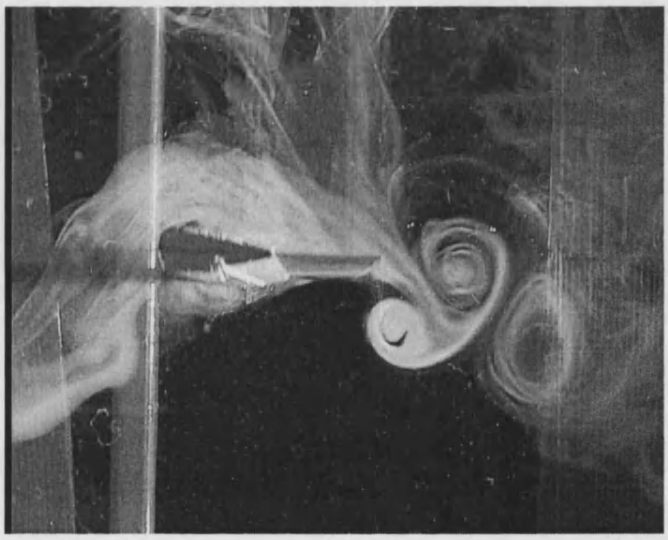

(b)

Figure 4.12: Smoke flow visualisation photographs for a rigid airfoil in heave in air. The vortex jet in frame (a) is deflected up. At a later time, frame (b), it is deflected down.

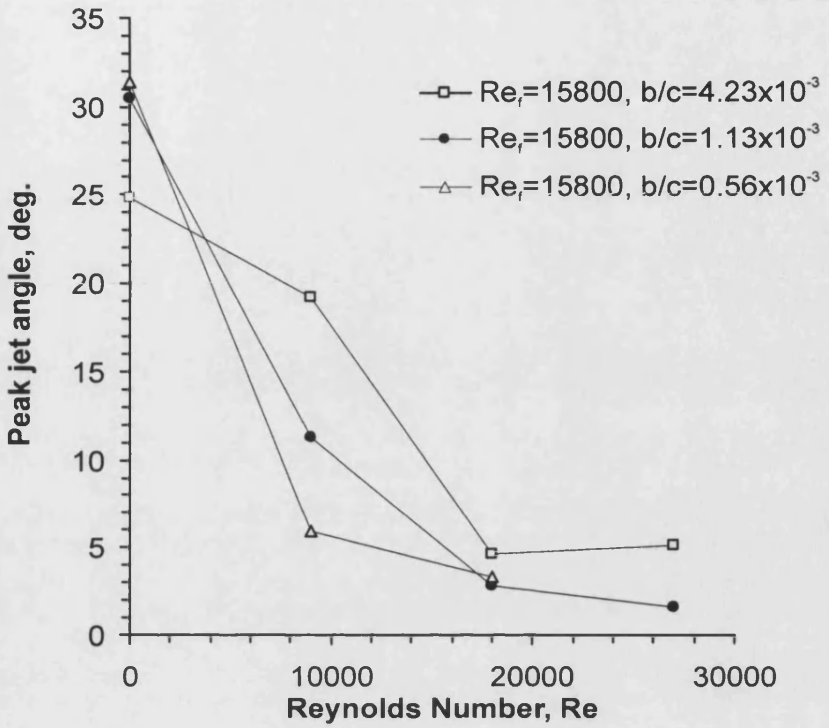

Figure 4.13: Variation of peak jet deflection angle with Reynolds number.

5 EFFECT OF CHORDWISE FLEXIBILITY AT LOW REYNOLDS NUMBERS

5.1 SUMMARY

Water tunnel experiments on chordwise-flexible airfoils heaving with constant amplitude have been carried out for Reynolds numbers of 9000 to 27000. Introducing a degree of flexibility was found to yield increases in both thrust coefficient and propulsive efficiency. By analogy to a rigid airfoil in coupled heave and pitch, thrust coefficient and propulsive efficiency were found to be functions of the Strouhal number and pitch phase angle. Contour plots of efficiency in the Strouhal number-pitch phase angle plane showed a distinct peak for a pitch phase angle of 95-100 degrees, (consistent with experimental and Navier-Stokes analyses of rigid airfoils in coupled heave and pitch, and with the value found in nature for fish) and a Strouhal number of 0.29, which lies in the middle of the range observed in nature. Contours of thrust coefficient showed thrust to peak for pitch phase angles in the region of 110-120 degrees, consistent with studies in the literature. Studies of the flow field near the surface of the airfoil and downstream of the trailing-edge revealed stronger vortices corresponding to higher thrust coefficients, and weaker leading-edge vortices corresponding to higher efficiencies. The results suggest the effect of chordwise flexibility is beneficial for purely heaving airfoils at low Reynolds numbers.

5.2 AIM

Numerical models have indicated higher efficiencies for flexible airfoils in non-zero freestream cases[34-36], though the computational complexity of the situation

requires assumptions either of inviscid flow[34] or of a pre-defined flexing motion[36]. Experimentally, there are findings of higher efficiency at non-zero Reynolds numbers[41], though a systematic study of the effect of airfoil deformation on the flow field and force coefficients is absent from the literature. The aim of this chapter is to find the relationship between the deformation, flow pattern, thrust coefficient, and efficiency of a flexible 2D airfoil oscillating in heave at low Reynolds numbers.

Four appropriate parameters are the Reynolds number, 'Re', dimensionless heave amplitude, 'h', Strouhal number, 'St', and bending stiffness, 'λ'. The Strouhal number, $St=2fa/U_0$, is based on the peak-peak amplitude of the leading-edge. The Strouhal numbers of insects, birds, bats, and fish are observed to lie within a narrow range[42] of $0.2<St<0.4$.

5.3 RESULTS

The following sections present the results for the chordwise-flexible airfoil, where the effect of airfoil stiffness is investigated. Thrust coefficient and efficiency are studied firstly as functions of plate thickness, Strouhal number and Reynolds number and then, following analysis of the deformation characteristics of the airfoil, as functions of pitch phase angle, Strouhal number and Reynolds number. Optimum pitch phase angles for thrust and efficiency are found, and compared to those in the literature. Flow fields are shown throughout, to illustrate how trends in thrust and efficiency relate to changes in the flow pattern. In this chapter, the quantity 'C_T/St^2' will be plotted rather than 'C_T', for reasons discussed in Chapter 1.

5.3.1 THRUST - EFFECT OF AIRFOIL STIFFNESS

The remainder of this chapter focuses on the effect of chordwise flexibility. All experimental results from this point forwards are for the chordwise flexible airfoil shown in Figure 2.5. The variation of thrust coefficient divided by the square of the Strouhal number, C_T/St^2, with plate thickness is plotted in Figure 5.1. Plots are shown for (a) Re=9,000, (b) Re=18,000 and (c) Re=27,000. Measurements are taken for seven plates of different thickness. For each Reynolds number, and for each Strouhal number, a peak in the thrust coefficient is observed. The peak moves to higher values

of plate thickness with increasing Strouhal number. For high Strouhal numbers, the optimum thickness may be exceeded without a severe degradation in performance, although a sharp decline in thrust coefficient occurs if the airfoil is too thin. The results indicate that flexibility improves the thrust performance of the airfoil at low Reynolds numbers. Note that, although the Strouhal number range decreases with increasing Reynolds number, the oscillation frequencies, in Hertz, are the same for parts (a), (b), and (c).

The features of the wake for rigid and flexible airfoils may be illustrated with example velocity and vorticity fields for Re=9000, Re=18000 and Re=27000. Three velocity fields are shown in Figure 5.2 for Re=9000. The outline of the airfoil is drawn, and velocity vectors in the plane of the mid-span of the airfoil are shown. The position of the leading-edge in each part, s=+a, corresponds to a time t/T=0. The three parts in Figure 5.2 correspond to three different plate thicknesses in the St=0.56 line of Figure 5.1a. Differences exist between parts (a) (b) and (c) in the shape of the airfoil and in the velocity field. In the case of the stiffest plate (Figure 5.2a), the *pitch angle*, θ, of the airfoil, defined by the angle between the freestream and a chord-line drawn from the leading-edge to the trailing-edge, is less than 1 degree; the airfoil is essentially rigid. The *pitch amplitudes* of the intermediate (part (b)) and highly flexible airfoil (part (c)) are 6 degrees and 17 degrees respectively. As expected, the pitch amplitude increases with plate flexibility. A more subtle difference exists between the airfoils in parts (b) and (c): whereas for the case of intermediate stiffness the airfoil pitches down at t/T=0, the reverse is true of the most flexible airfoil. In this way it is seen that the stiffness of the plate affects both the pitch amplitude and the *pitch phase angle*. It is seen later that a relationship exists between pitch phase and pitch amplitude. Since the pitch amplitude of the stiffest plate is very small, it is not possible to determine the pitch phase angle accurately. The thrust coefficient is greatest for the airfoil of intermediate flexibility (Figure 5.2b) (see also Figure 5.1a); the vortices from this airfoil are stronger, and further apart in the lateral (y) direction. It is noted that vortex pairs are observed for the stiffest and intermediate airfoils.

Time-averaged velocity magnitude contours for the three airfoils are shown in Figure 5.3. The average is over four complete oscillations of the airfoil (64 captures per

oscillation). The peak jet velocity and jet width are seen to be highest for the airfoil of intermediate plate thickness, consistent with the force data. The jets from the intermediate and greatest stiffness airfoils lie at an angle to the freestream direction. The vortices in these two cases are shed in pairs. Such deflected jets have been found to occur when the Strouhal number exceeds a critical value[13].

Vorticity fields for three airfoils of different plate thickness are shown in Figure 5.4 for Re=18000. The leading-edge of the airfoil is moving upwards through the origin (t/T=3/4). Each *phase-averaged* vorticity field was calculated from a series of 200 velocity fields, each captured at the same point in the oscillation. Clockwise vorticity is shown white, counter-clockwise vorticity black. It is noted that, whereas vortex pairs were observed in the Re=9000 case, a reverse vortex street, parallel to the freestream, is observed in the present case. This is attributed to the lower Strouhal number. The highest thrust coefficient occurs for the airfoil of intermediate stiffness (part (b)). It is seen that the vortices from the intermediate airfoil are stronger, and spaced further apart in the lateral direction than those from the stiffest airfoil. Although a large distance in the lateral direction separates the vortices from the least stiff airfoil, their strength is considerably lower than for either of the other two airfoils.

Velocity magnitude and vorticity contour fields for the three airfoils are shown in Figure 5.5 for Re=27000. Again, the leading-edge is moving upwards through the origin. Grey levels indicate velocity magnitude; white lines indicate contours of vorticity (solid for clockwise flow, dotted for counter-clockwise flow). The highest thrust coefficient occurs for the airfoil of intermediate stiffness (part (b)). In this case it is seen that a large lateral distance separates the regions of opposite vorticity. It is noted that the vortices from the most flexible airfoil are shed almost in a line. The measured thrust coefficient, C_T=0.04, is correspondingly small.

5.3.2 THRUST - EFFECT OF OSCILLATION FREQUENCY

Plots of thrust coefficient against Strouhal number are shown in Figure 5.6 for five plate thicknesses. Plots are shown for (a) Re=9000, (b) Re=18000, and (c) Re=27000. With the appropriate choice of airfoil, benefits to flexibility are observed over the

complete Reynolds and Strouhal number range. Peaks in thrust coefficient are observed in some cases, although not as markedly as in the plots of thrust coefficient against plate thickness. The peaks are seen to move to higher Strouhal numbers with increasing plate stiffness. For all Reynolds numbers, a transition from drag to thrust occurs for the stiffest, essentially rigid, airfoil, at a Strouhal number St=0.17, and earlier for the flexible airfoils.

Instantaneous vorticity contour plots corresponding to the $b/c=0.85x10^{-3}$ curve in Figure 5.6a are shown in Figure 5.7. The stiffness of the airfoil is the same for each plot, and the frequency is incremented from part (a) to part (c). The leading-edge is moving upwards through the origin in each part. As expected, the pitch angle of the airfoil at this instant increases with increasing Strouhal number. The pitch angle of the airfoil undergoing the lowest frequency oscillation is around 1 degree. The vortices in the intermediate frequency case (maximum thrust coefficient) are seen to be stronger, and separated by a greater lateral distance, than the vortices of the low frequency case. In the high frequency case (Figure 5.7c), vortices are shed in pairs. This is commensurate with the higher Strouhal number effects[13]. It is seen that the jet is deflected slightly away from the freestream direction.

Time-averaged velocity magnitude plots for the three Strouhal numbers in Figure 5.7 are shown in Figure 5.8 parts (b), (d) and (f). Additional frequencies are plotted in parts (a), (c) and (e). The plots were obtained by averaging over 70 captures. The shading indicates the velocity magnitude normalised by the peak leading-edge heave velocity. The strength of the jet is seen to grow with frequency, reach a maximum around part (c), and then decay. The frequency for which the strongest jet is observed corresponds to the peak in thrust coefficient (Figure 5.8d). In parts (e) and (f), a deflected jet (seen in the instantaneous vorticity field of Figure 5.7c) is characteristic of the high Strouhal number effects mentioned earlier.

5.3.3 EFFICIENCY

Propulsive efficiency is plotted as a function of Strouhal number in Figure 5.9 for (a)Re=9000, (b)Re=18000, and (c)Re=27000. Cases of negative efficiency (drag) are not shown. Curves for five plate thicknesses are shown to illustrate the effect of airfoil

stiffness. It is seen that the efficiency of the flexible airfoils is significantly higher than the efficiency of the stiffest, essentially rigid airfoil. Hence flexibility is seen to offer significant efficiency benefits, in addition to increases in thrust. For the Re=9000 case, the propulsive efficiency at low Strouhal numbers increases with increasing flexibility. It is possible that a still more flexible airfoil may yield even higher efficiencies. At the highest Strouhal number, it is one of the intermediate stiffnesses which yields the greatest efficiency. This trend is observed for all Reynolds numbers. A further trend is for the efficiency to move from positive to negative for the rigid airfoil at a Strouhal number of approximately 0.17 for each Reynolds number (consistent with the change from negative to positive thrust), and for the transition to positive efficiency to occur earlier for the flexible airfoils.

As discussed earlier, the efficiency of oscillating airfoils is closely related to the flow near the leading-edge. Flow separation has been shown to lead to significantly reduced propulsive efficiencies. It is therefore of interest to study the flow at the leading-edge of the tear-drop/plate airfoil, and to make a comparison between the rigid and flexible cases. The flow pattern over the airfoil for one complete oscillation is shown in Figure 5.10 for times t/T=0,1/4,1/2,3/4. The method is of dye flow visualisation, and dye is released into the flow one chord-length upstream of the leading-edge. It is noted that the Reynolds number in Figure 5.10 is chosen to yield the clear flow visualisation images, and is lower than the Reynolds number of the thrust and efficiency measurements. However, the Strouhal number is typical of those in the force measurements. The airfoil is moving upwards through the origin in part (a), reaches the highest displacement in part (b), returns through the origin in part (c), and reaches the lowest displacement in part (d). The formation of both leading-edge and trailing-edge vortices is visible. Leading-edge vortices are observed to be shed in pairs, to convect downstream and be swept into the trailing-edge vortex pattern. Similar vortex shedding patterns have been simulated numerically by Lewin and Haj-Hariri[17], who found that although leading-edge vortices may be shed in pairs, the vortices of the pair tend to be unequal in strength. The manner in which the leading-edge vortices affect the efficiency has been explained in terms of the perturbation to the pressure distribution over the surface of the airfoil[44] and the disturbance they cause to the trailing-edge vortex system[17]. It has been shown that minimising the strength of the leading-edge vortices is necessary in order to achieve high efficiency,

and this is achieved through minimising the effective angle of attack[15, 18, 28]. However, such small angles of attack tend to yield low thrust coefficients and a balance may therefore be sought between high efficiency and high thrust[18, 28, 69]. For a given Reynolds number and Strouhal number, it is interesting to compare the vortex shedding patterns for the airfoil stiffness which maximises efficiency with the stiffness which maximises thrust coefficient. Such a comparison is made in Figure 5.11, where the vorticity patterns of two airfoils are shown over one heave cycle, for Re=9000, St=0.34. The two columns of images show vorticity magnitude fields at the same points in the cycle as Figure 5.10. The first column of images is for the airfoil which experiences the greatest thrust coefficient. The second column of images is for a more flexible airfoil, which experiences the greatest efficiency. The formation and shedding of leading-edge vortices is visible in both cases, although those of the more flexible airfoil (column II) are observed to be weaker, both at the point of formation and further downstream where they are swept into the trailing-edge vortex pattern. This is consistent with the higher efficiency. In contrast, the trailing-edge vortex pattern is moderately stronger for the stiffer airfoil (column I). It is also noted that, as observed in the simulations of Lewin and Haj-Hariri[17], leading-edge vortices may be shed in pairs, with one dominant in strength.

5.3.4 AIRFOIL SHAPE CHARACTERISTICS

A possibly more physically meaningful approach is to plot thrust coefficient against a shape characteristic of the airfoil, rather than against plate thickness. Pitch amplitude, pitch phase angle and trailing-edge amplitude are possible parameters. A displacement–time plot for the single case Re=9000, $b/c=0.56\times10^{-3}$, St=0.34 is plotted in Figure 5.12. The 'y' coordinates (see Figure 2.5) of the leading and trailing-edges, and of the difference between them, s_{LE}-s_{TE} , are plotted as functions of time. It is seen that the trailing-edge trails the leading-edge in phase, whereas s_{LE}-s_{TE} is seen to lead the leading-edge. From Figure 2.5, it is seen that the tangent of the pitch angle is equal to s_{LE}-s_{TE} divided by the streamwise separation of the leading and trailing-edges. The pitch phase angle is found by finding the phase of this new quantity relative to the leading-edge. In the particular case illustrated in Figure 5.12, the pitch phase angle is found to be 92.2 degrees. The finding of a pitch phase angle of this

value is of interest because phase angles of 90 degrees have been found in the literature to optimise efficiency[15, 18].

Pitch amplitude, pitch phase angle and trailing-edge amplitude are plotted against Strouhal number in Figure 5.13. In addition to the specific case just discussed (Re=9000, $b/c=0.56\times10^{-3}$), curves are also drawn for $b/c=0.85\times10^{-3}$, $b/c=1.13\times10^{-3}$, and $b/c=1.41\times10^{-3}$. It is seen from Figure 5.13a that, as a consequence of the inertia of the fluid, the pitch amplitude increases with increasing oscillation frequency and increasing flexibility. Pitch phase angle is plotted in Figure 5.13b. It is seen that the pitch phase angle is always positive, indicating that the pitching motion of the airfoil always leads the heaving motion. The pitch phase angle is seen to increase with increasing plate flexibility. The amplitude of the trailing-edge is plotted against oscillation frequency in Figure 5.13c. Trailing-edge amplitude is not an independent quantity, but is a function of pitch amplitude and pitch phase angle. With reference to Figure 2.5, a pitch phase angle of zero degrees gives maximum positive ($s_{TE}<s_{LE}$) pitch angle when $s_{LE}=+a$. A pitch phase angle of 180 degrees gives maximum negative pitch angle when $s_{LE}=+a$. A 180 degree pitch phase angle is therefore favourable if a high trailing-edge amplitude is sought. At low Strouhal numbers the pitch phase angle is favourable. However, the pitch amplitude is very small, leading to a trailing-edge amplitude approximately equal to the leading-edge amplitude. At high Strouhal numbers the pitch amplitude is favourable and the pitch phase angle is unfavourable. Peaks in trailing-edge amplitude are observed at intermediate Strouhal numbers.

As stated above, the thrust coefficient may be plotted against a shape characteristic of the airfoil, rather than against plate thickness. It appears at first that three possibilities exist: pitch amplitude, pitch phase angle and trailing-edge amplitude. When these quantities are plotted against each other an interesting pattern emerges. Pitch amplitude is plotted against pitch phase angle in Figure 5.14a. Data for airfoils with $b/c=0.56\times10^{-3}$, 0.85×10^{-3}, 1.13×10^{-3}, 1.41×10^{-3} and 4.23×10^{-3} are plotted for Re=9000, 18000, and 27000, and for all Strouhal numbers. The direction of increasing flexibility and oscillation frequency is indicated. It is seen that pitch amplitude and pitch phase angle are dependent. Pitch amplitude varies almost linearly with pitch phase, with a gradient of -0.18±0.2. The limiting value of the pitch phase angle as the

amplitude tends to zero is 150±15 degrees. It is noted that the experimental scatter is greatest in the small pitch-amplitude region. This is because of the difficulty in measuring the phase of small amplitude oscillations accurately. The trailing-edge amplitude is plotted against pitch phase angle in Figure 5.14b. It is seen that the two quantities are dependent. For high pitch phase angles the pitch amplitude is very small (Figure 5.14a), and the trailing-edge amplitude tends to the limit of unity. At low pitch phase angles the pitch amplitude is high but the phase is such that the airfoil pitches most steeply at an unfavourable point in the cycle; the trailing-edge amplitude is low again. At an intermediate pitch phase, of approximately 100 degrees, the trailing-edge amplitude reaches a peak. In summary, it is seen that the three quantities - pitch amplitude, pitch phase angle and trailing-edge amplitude - are dependent.

The question arises as to which parameter is most suitable to replace the plate thickness. Of the three possibilities, pitch phase angle has been found throughout the literature to be of consistent significance. Furthermore, the value of the pitch phase angle which maximises efficiency has been found across a broad range of studies to lie in the region of 90 degrees. For example, the Navier-Stokes analyses of Tuncer and Kaya[18], Isogai et al.[15], Tuncer et al.[70], Ramamurti and Sandberg[71], and Pedro et al.[28] predict optimum pitch phase angles of 86, 90, 90, 90-100, and 90-110 degrees respectively; in nature it is observed that pitch oscillations of the fin lead the heave motion by an angle close to 90 degrees[72]; experimentally, Anderson[22] found high efficiencies for pitch phase angles of 75 and 90 degrees, while Read et al.[73] found high efficiencies in the region of 90-100 degrees. The common finding in the Navier-Stokes studies is that pitch phase angles in this range tend to lower the effective angle of attack amplitude, thus lessening the degree of leading-edge flow separation. Propulsive efficiency curves from a selection of these analyses, as well as the prediction of Garrick theory and a panel method from Jones[43], are plotted in Figure 5.15. Note that, although the Reynolds number, Strouhal number, and amplitudes differ greatly, the optimum pitch phase angle is around 90 degrees for each data set. Also shown in the figure is a curve from the present set of data, where each data point corresponds to a different plate thickness. The similarity of the shape of the efficiency curve for the present data set to those of the studies of rigid airfoils in coupled heave and pitch, and the closeness of the optimum pitch phase angle to those in the other studies, suggests that the pitch phase angle is a suitable alternative

parameter to the plate thickness. The performance of the airfoil may now be analysed in terms of the Strouhal number and pitch phase angle.

5.3.5 EFFECT OF PITCH PHASE ANGLE AND STROUHAL NUMBER

When thrust coefficient and propulsive efficiency are plotted against pitch phase angle an interesting pattern emerges: curves of constant Strouhal number tend to fall onto each other. Example plots are shown in Figure 5.16. In part (a), thrust coefficient curves for St=0.33 and St=0.49 are drawn; efficiency curves are shown in part (b). It is seen that the effect of Reynolds number is small, as seen earlier for the NACA0012 airfoil.

The complete data set is represented as contour plots in Figure 5.17 for thrust coefficient (part (a)) and efficiency (part (b)). Contours of thrust coefficient are drawn on a Pitch Phase Angle – Strouhal Number plane in part (a). The white curve indicates the optimum pitch phase angle (in terms of thrust) for a given Strouhal number. For a Strouhal number of St=0.29, for example, the optimum pitch phase angle is 110±4 degrees. An airfoil of this flexibility would experience a higher thrust coefficient than a less flexible airfoil (the region to the right of the white curve), or a more flexible airfoil (the area to the left). The optimum pitch phase angle is observed to decrease as the Strouhal number increases. From a design aspect, the plot indicates the optimum pitch phase angle for a given flight Strouhal number. The optimum pitch phase angle may be compared with values from the literature. Tuncer and Kaya[18], Pedro et al.[28], Ramamurti and Sandberg[71], and Isogai et al.[15] observed optimum (in terms of thrust) pitch phase angles of 100, 115, 120, and 120 degrees respectively. It is seen from Figure 5.17(a) that these values are in agreement with those found in the present experiment. The corresponding plot for propulsive efficiency is shown in Figure 5.17(b). The contour map exhibits a peak in efficiency at a Strouhal number of St=0.29. It is noted that this lies within the range of Strouhal numbers of $0.2<St<0.4$ found in nature[42]. It may also be compared to the optimum Strouhal number, St=0.30, found experimentally by Anderson[22]. The reason for the decrease in efficiency for lower or higher Strouhal numbers may be attributed to the increase in flow separation at higher Strouhal numbers (higher effective angles of attack), and a transition to drag at lower Strouhal numbers. The optimum pitch phase angle is seen

from Figure 5.17(b) to be 100±4 degrees, consistent with the values found in studies of rigid airfoils in coupled heave and pitch, and those found in nature (see above). It is noted that the angles found to optimise the thrust coefficient, both in the literature and in the present study, are higher than those found to maximise the efficiency. This is consistent with the observation[18] that it is not generally possible to achieve maximum thrust and efficiency simultaneously.

5.4 CONCLUSIONS

Water tunnel experiments on chordwise-flexible airfoils heaving with constant amplitude have been carried out for Reynolds numbers of 9000 to 27000. Peaks in thrust coefficient were found for intermediate stiffness (constant Strouhal number), and intermediate Strouhal number (fixed stiffness). These results suggested that a degree of flexibility is beneficial from a thrust aspect. The instantaneous flow fields showed stronger vortices in the cases of higher thrust. The time-averaged flow fields showed a stronger jet. At high Strouhal numbers, the jet was observed to be deflected, a finding consistent with previous studies in the literature.

Efficiency benefits were observed over a broad range of flexibility, with the optimum efficiency exceeding the efficiency of the inflexible airfoil by approximately 15%. Flow visualisation experiments revealed weaker leading-edge vortices in the cases of optimum efficiency.

An analogy was made between a flexible airfoil oscillating in heave and a rigid airfoil oscillating in pitch and heave. The three shape characteristics - pitch phase angle, pitch amplitude and trailing-edge amplitude - were found to be interdependent. Points from measurements for all Reynolds numbers, plate thicknesses, and heave frequencies, were found to lie on a line (pitch amplitude vs pitch phase angle) or a curve (trailing-edge amplitude vs pitch phase angle). The phase angle of the "pitch" was found to lead the heaving motion.

Thrust coefficient and propulsive efficiency were found to be functions of Strouhal number and pitch phase angle. Contour plots of efficiency in the Strouhal number-pitch phase angle plane showed a distinct peak for a pitch phase angle of 95-100 degrees (consistent with experimental and Navier-Stokes analyses of rigid airfoils in

coupled heave and pitch), and a Strouhal number of 0.29 (within the range $0.2<St<0.4$ observed in nature). Contours of thrust coefficient showed thrust to peak for pitch phase angles in the region of 110-120 degrees (consistent with studies of rigid airfoils in coupled heave and pitch in the literature). The results suggest the effect of chordwise flexibility is beneficial for purely heaving airfoils at low Reynolds numbers.

5.5 FIGURES

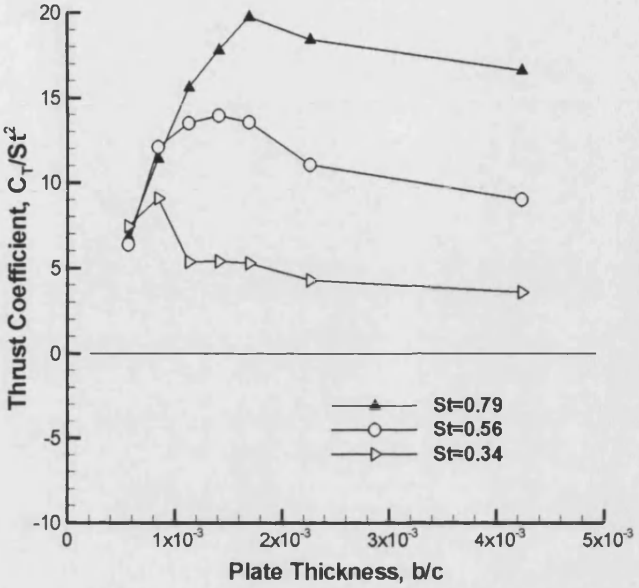

(a)

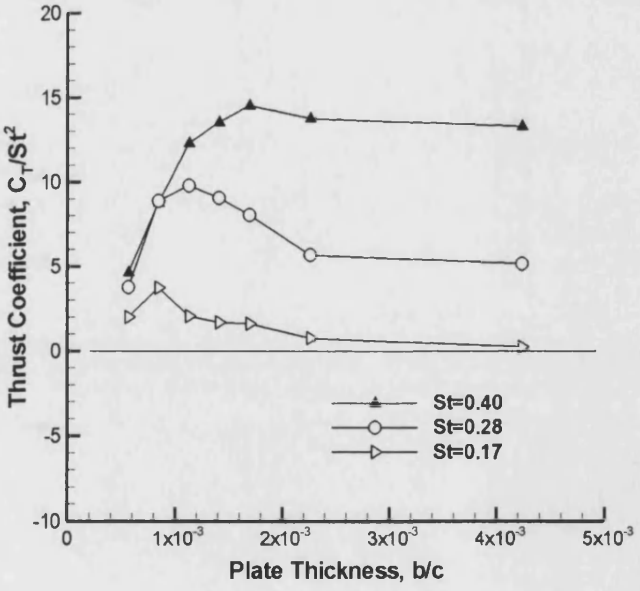

(b)

Figure 5.1: Thrust coefficient as a function of dimensionless plate thickness; (a) Re=9000; (b) Re=18000; (c) Re=27000.

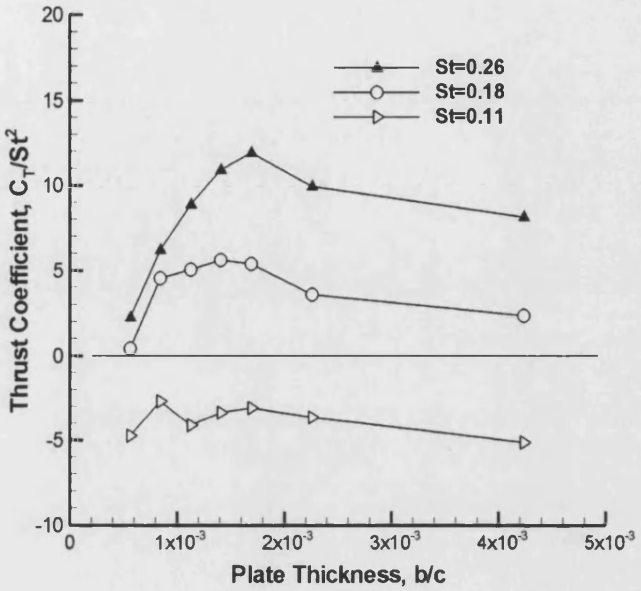

(c)

Figure 5.1 Cont.

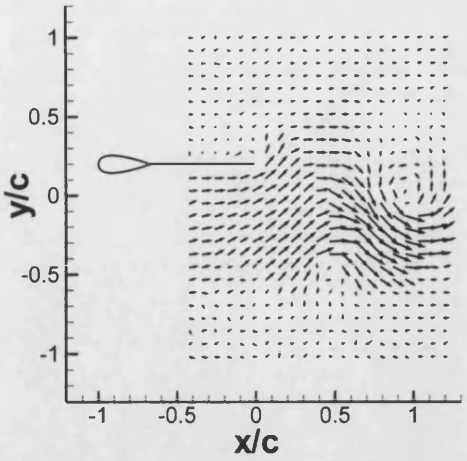

(a)

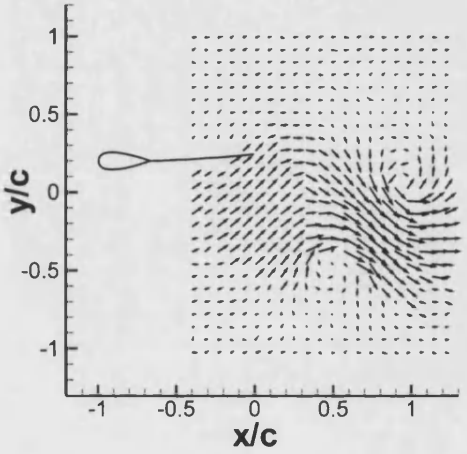

(b)

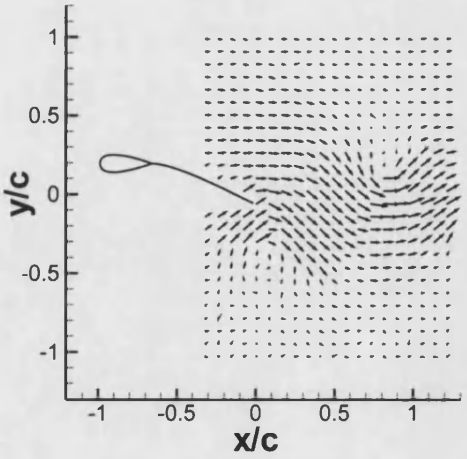

(c)

Figure 5.2: Instantaneous velocity fields at t/T=0 for Re=9000, St=0.56; (a) $b/c=4.23\times10^{-3}$; (b) $b/c=1.41\times10^{-3}$; (c) $b/c=0.56\times10^{-3}$. The time-averaged thrust coefficient is greatest in part (b).

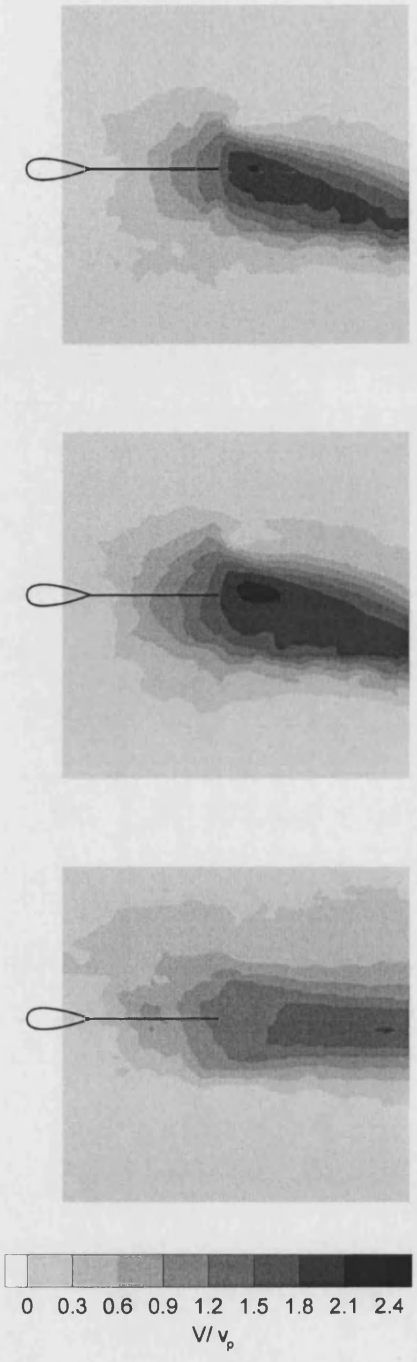

Figure 5.3: Time-averaged velocity fields corresponding to Figure 5.2; average over 4 cycles, rate of 64 captures/cycle.

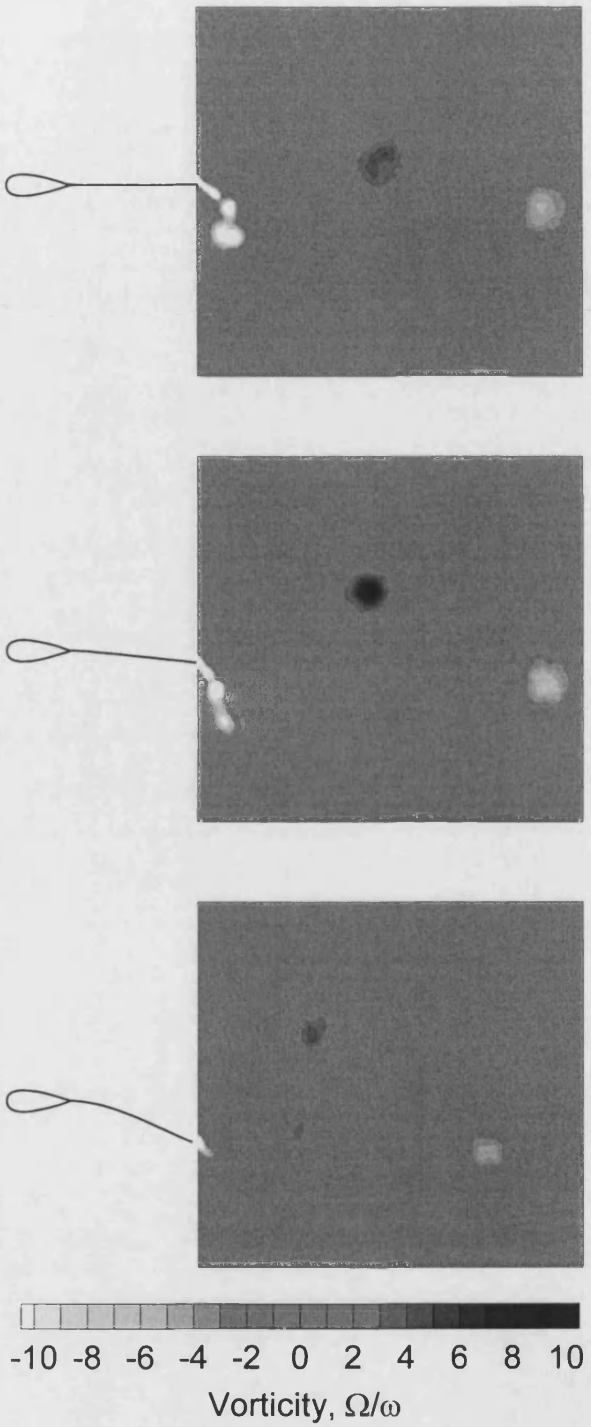

Figure 5.4: Phase-averaged vorticity fields for three airfoils; Re=18000, St=0.26, 200 capture average; (a) $b/c=4.23x10^{-3}$; (b) $b/c=1.13x10^{-3}$; (c) $b/c=0.56x10^{-3}$. The thrust coefficient is greatest in part (b).

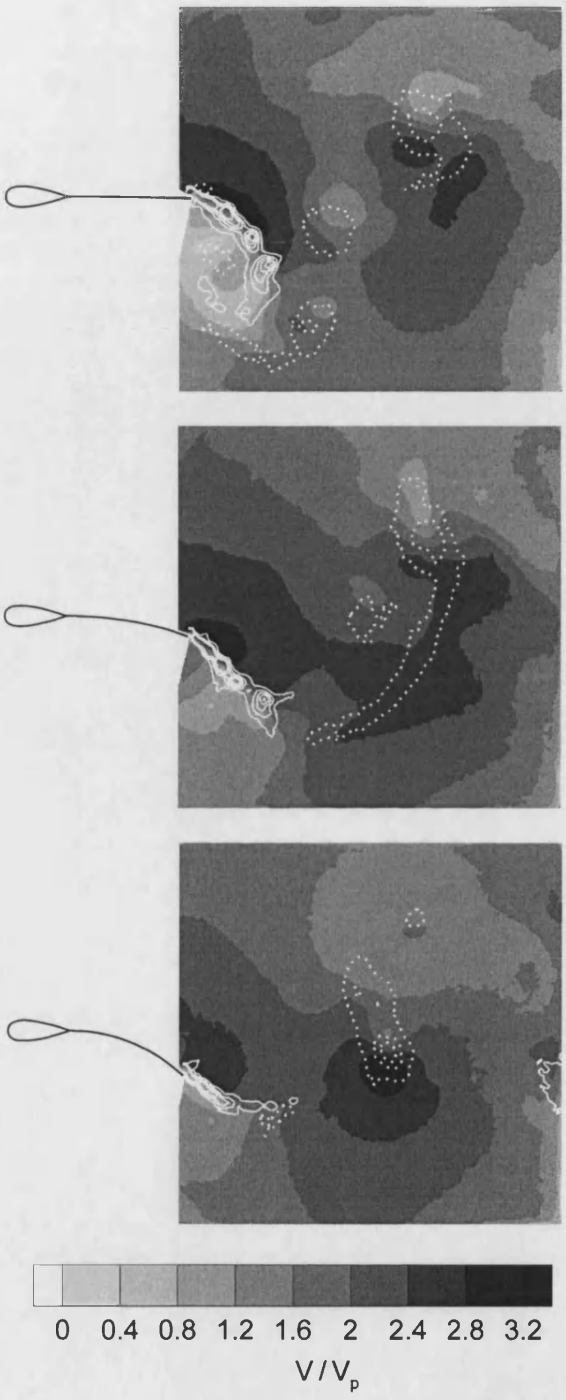

Figure 5.5: Phase-averaged velocity magnitude (greyscale) and vorticity (clockwise: solid white lines; counter-clockwise: dotted white lines) fields for three airfoils; Re=27000, St=0.17, 200 capture average; (a) $b/c=4.23\times10^{-3}$; (b) $b/c=1.13\times10^{-3}$; (c) $b/c=0.56\times10^{-3}$. The thrust coefficient is greatest in part (b).

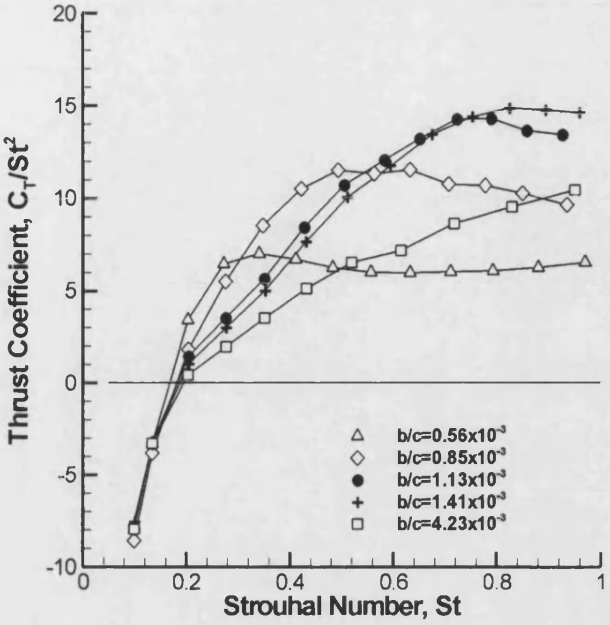

(a)

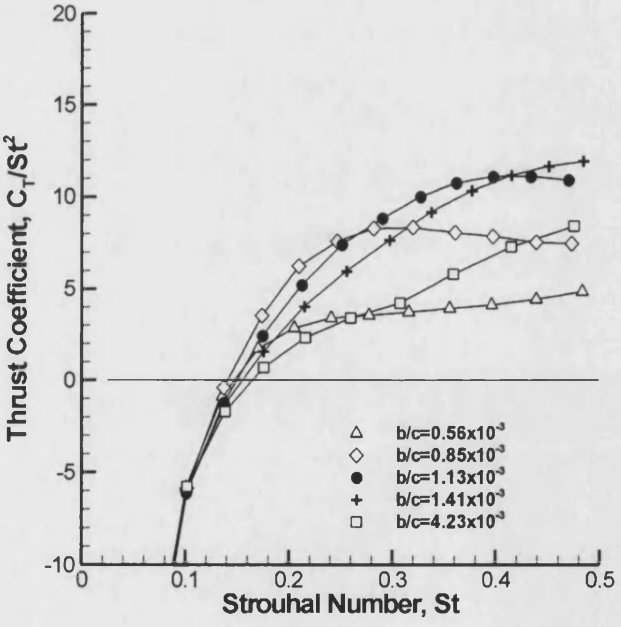

(b)

Figure 5.6: Thrust coefficient as a function of Strouhal number;(a) Re=9000; (b) Re=18000; (c) Re=27000.

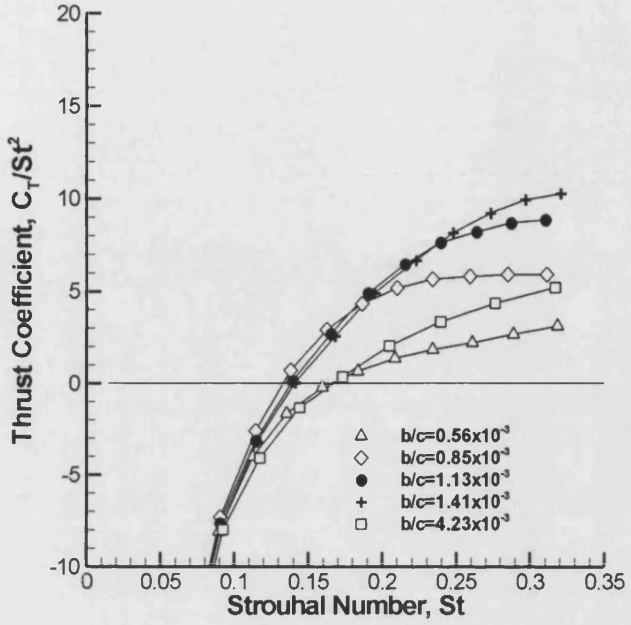

(c)

Figure 5.6 Cont.

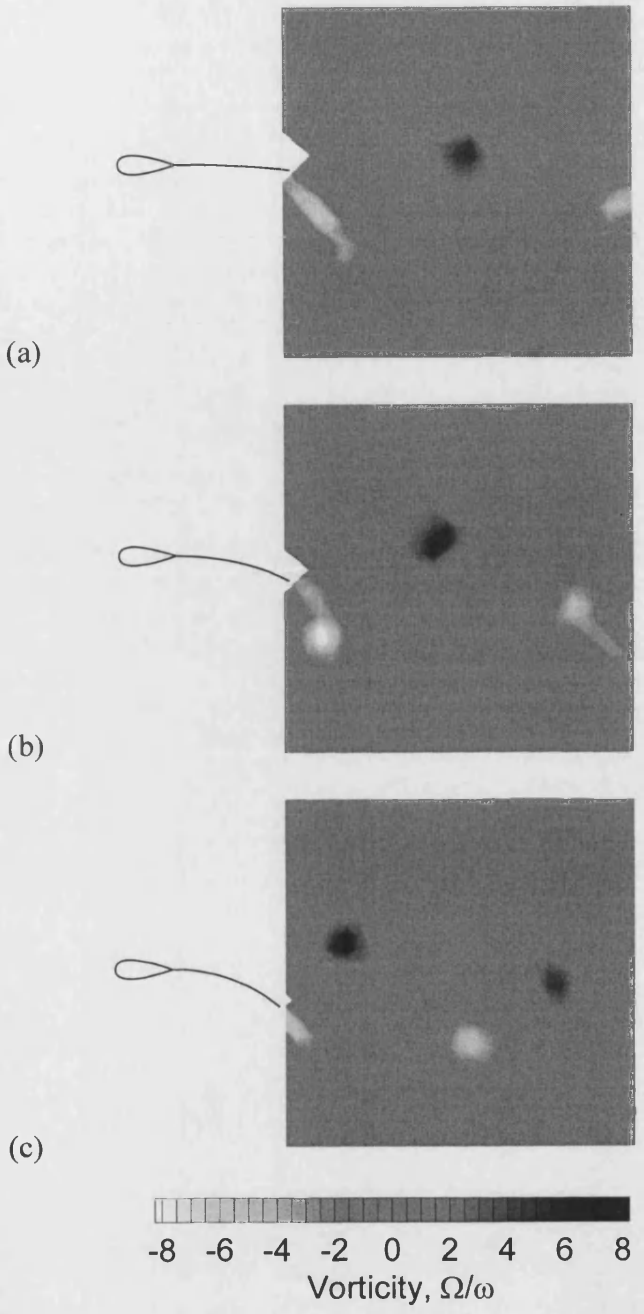

Figure 5.7: Instantaneous vorticity fields for an airfoil oscillating at three frequencies; Re=9000, b/c=0.85x10^{-3}; (a) St=0.27; (b) St=0.48; (c) St=0.97. The thrust coefficient is greatest in part (b).

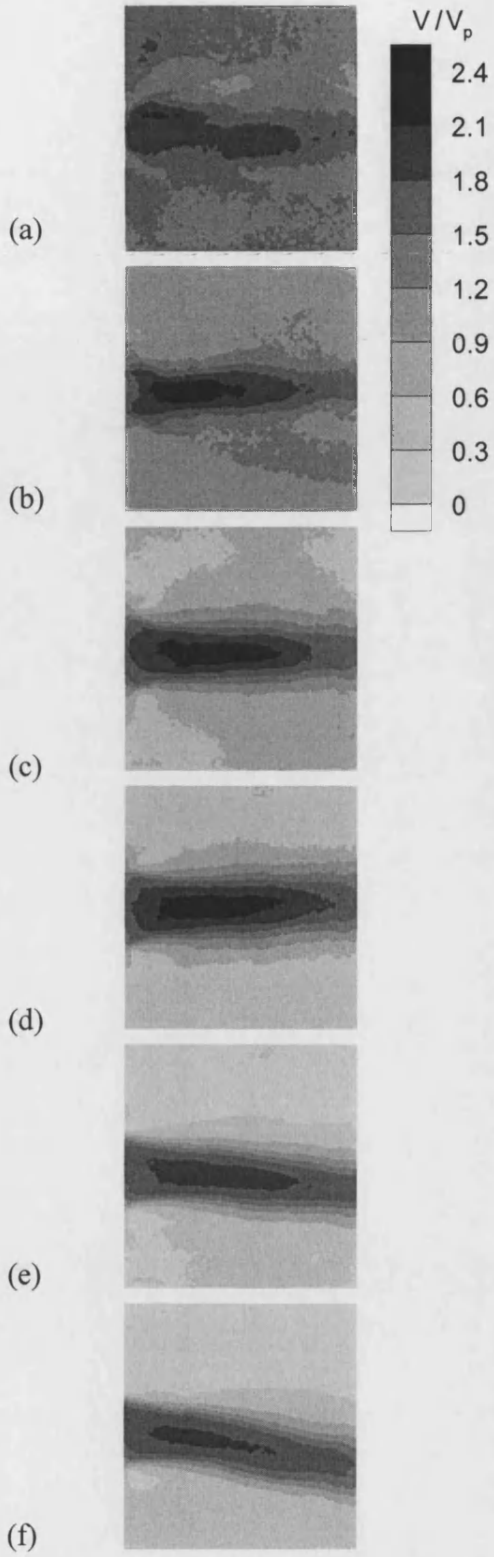

Figure 5.8: Time-averaged velocity fields for a single-stiffness airfoil oscillating at six frequencies; Re=9000, b/c=0.85x10^{-3}; (a) St=0.20; (b) St=0.27; (c) St=0.41; (d) St=0.48; (e) St=0.88; (f) St=0.97.

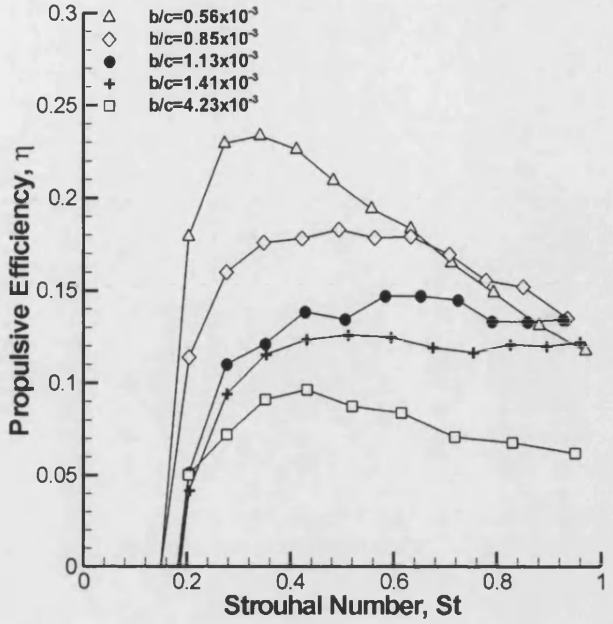

(a)

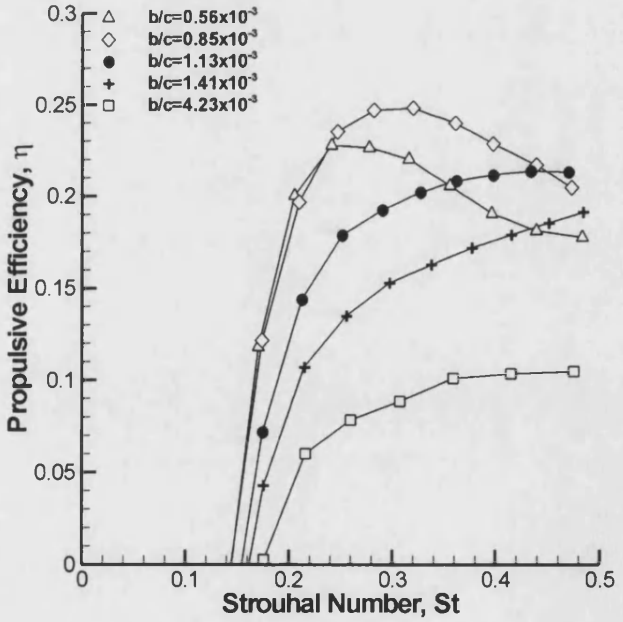

(b)

Figure 5.9: Propulsive efficiency as a function of Strouhal number; (a) Re=9000; (b) Re=18000; (c) Re=27000.

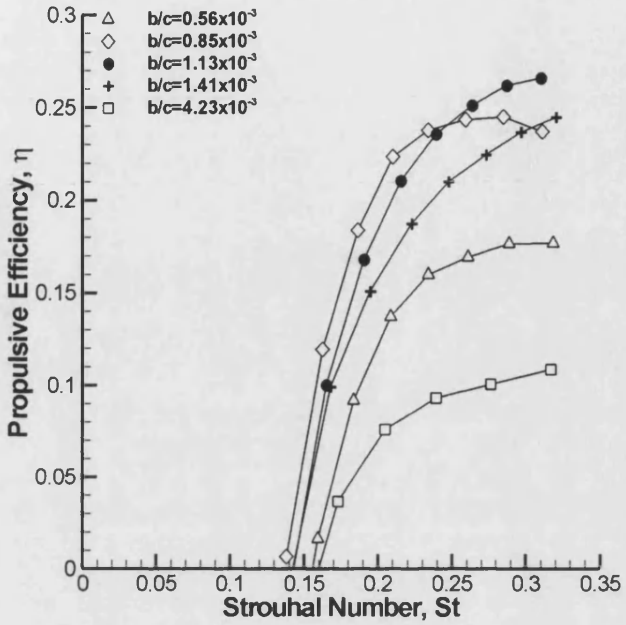

(c)

Figure 5.9 Cont.

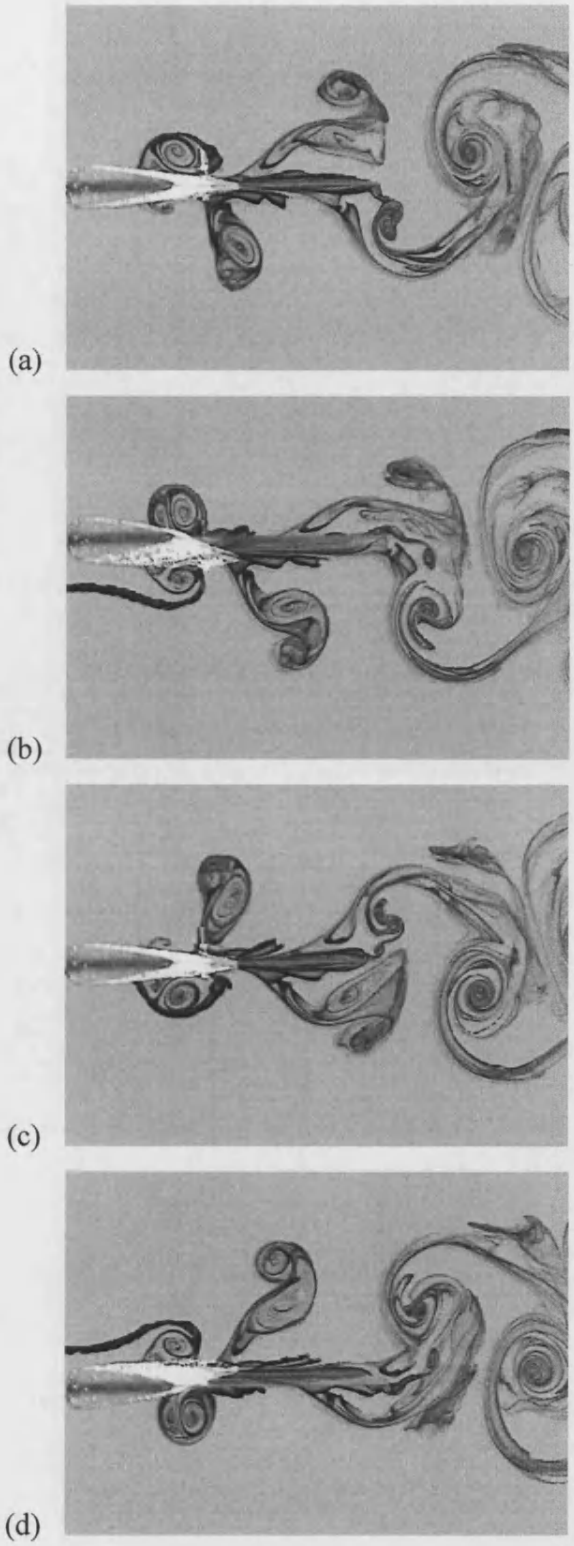

Figure 5.10: Leading-edge vortex dye flow visualisation; Re=1800, St=0.29, b/c=4.23x10^{-3}; (a)t/T=0, (b)t/T=1/4, (c)t/T=1/2, (d)t/T=3/4. Note that the flat plate element is difficult to see.

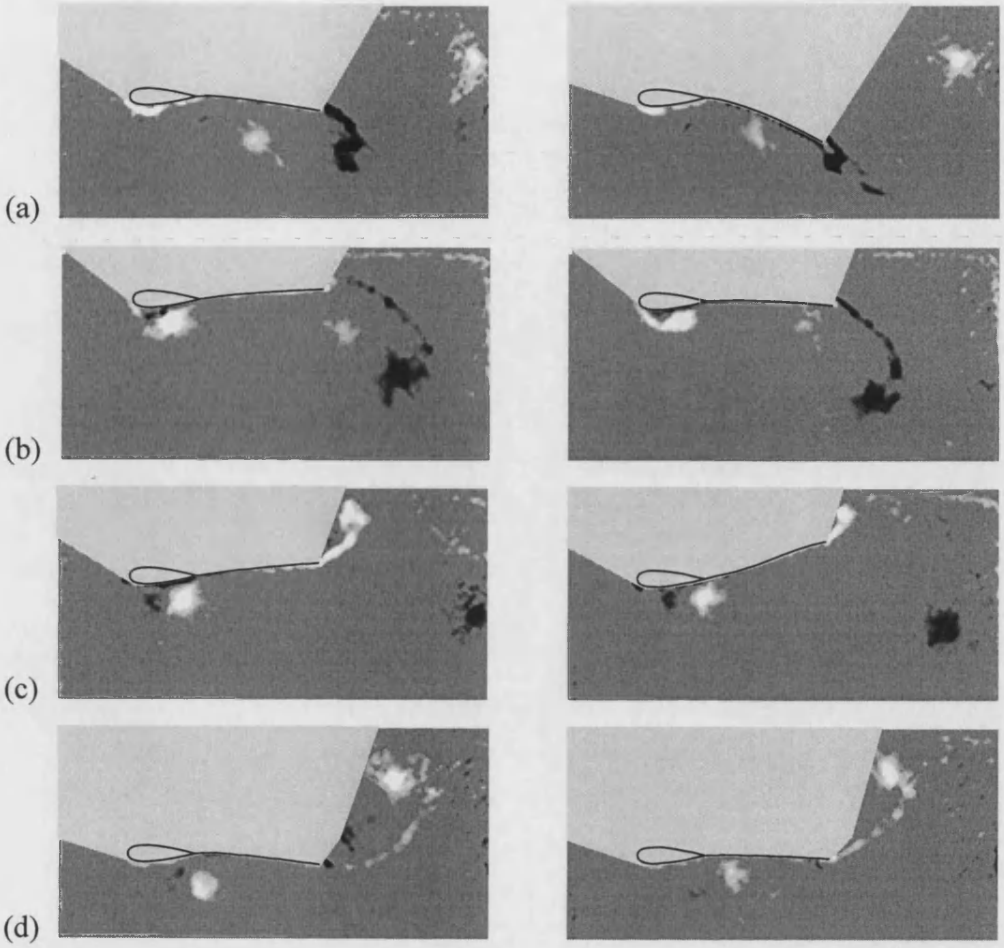

Figure 5.11: Instantaneous leading-edge vortex PIV flow visualisation; Re=9000, St=0.34; (I)b/c=0.85x10^{-3} – maximises thrust (II)b/c=0.56x10^{-3} – maximises efficiency (a)t/T=0, (b)t/T=1/4, (c)t/T=1/2, (d)t/T=3/4.

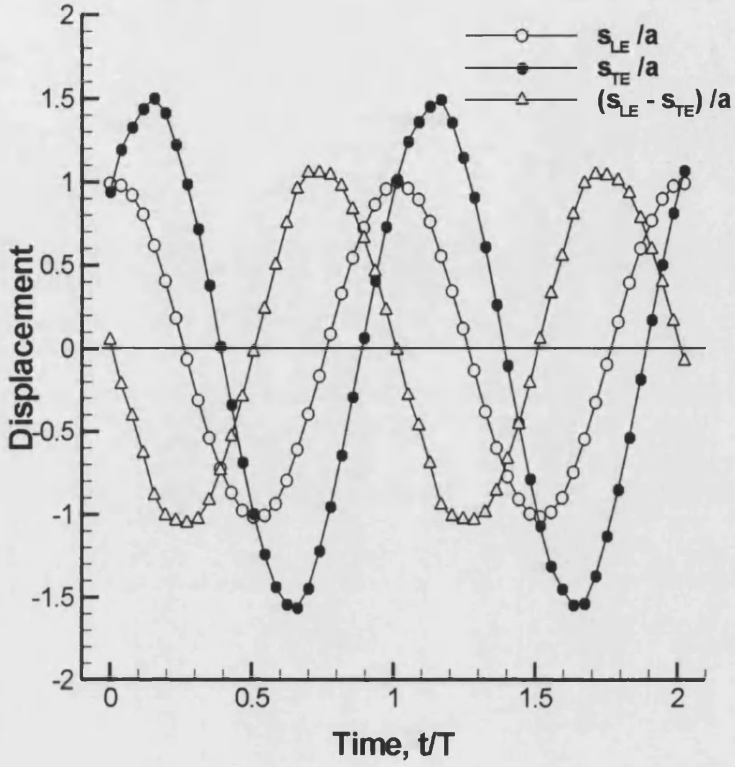

Figure 5.12: Leading-edge displacement, trailing-edge displacement, and deformation as a function of time; Re=9000, b/c=0.56x10^{-3}, St=0.34.

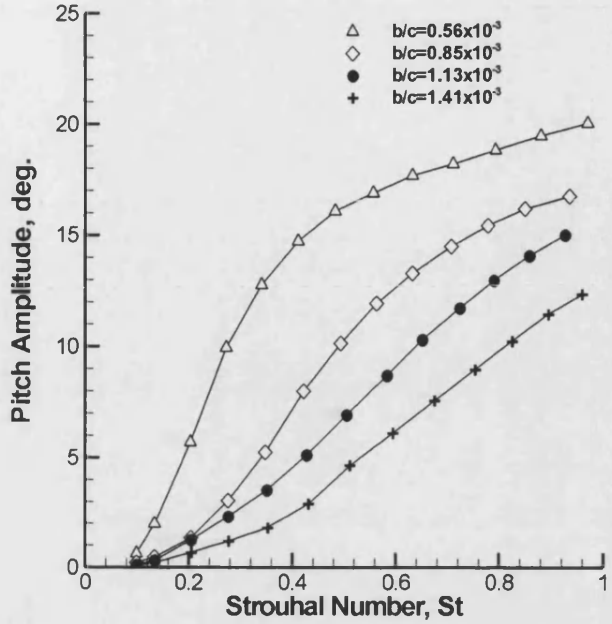

(a)

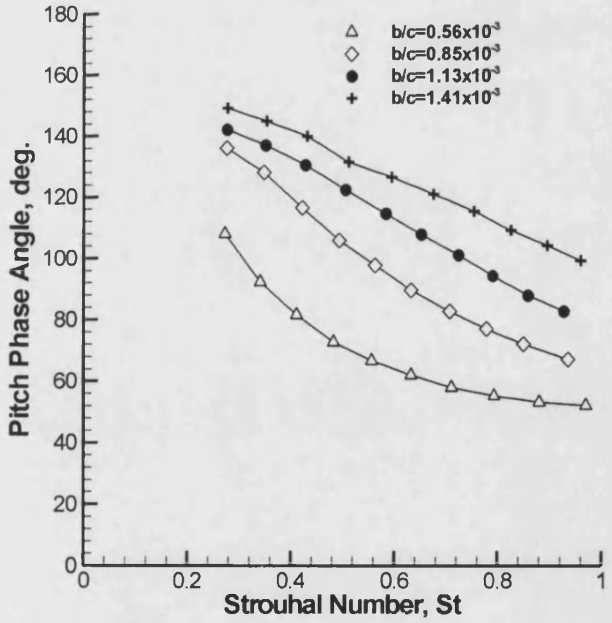

(b)

Figure 5.13: The variation with Strouhal number of (a) Pitch amplitude, (b) Pitch phase angle, and (c) Tailing-edge amplitude. Re=9000.

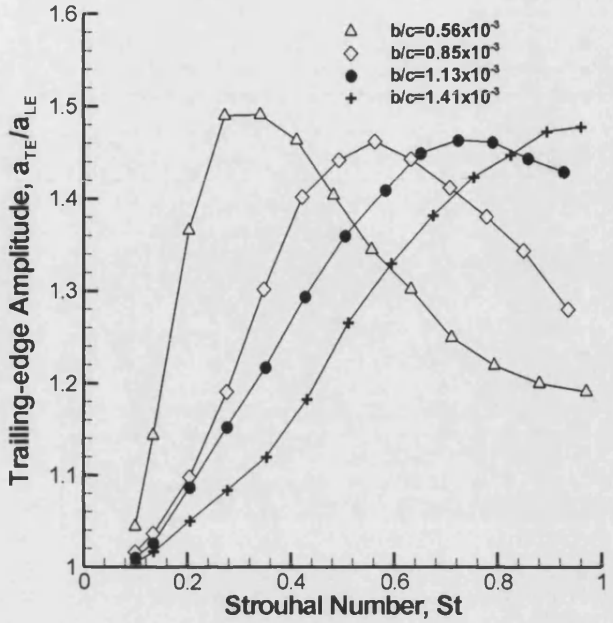

(c)

Figure 5.13 Cont.

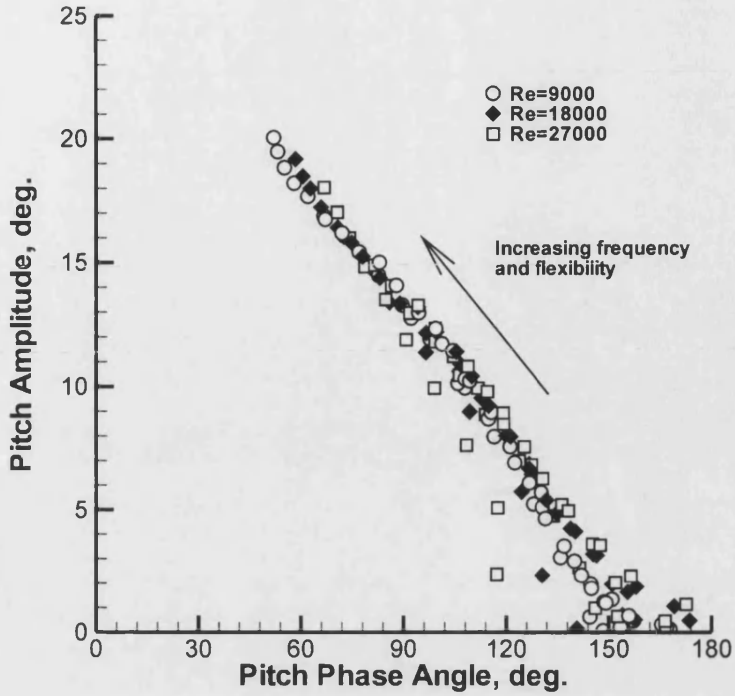

(a)

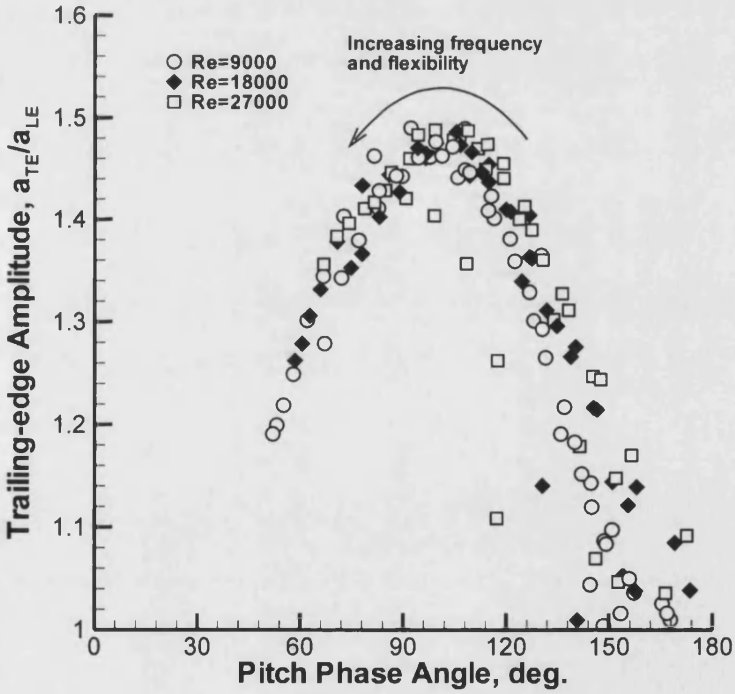

(b)

Figure 5.14: (a) Pitch amplitude as a function of pitch phase angle for the complete data set. The data points for all Reynolds numbers, airfoil thicknesses and oscillation frequencies fall onto a line. (b) Trailing-edge amplitude as a function of pitch phase angle. The data points fall onto a curve.

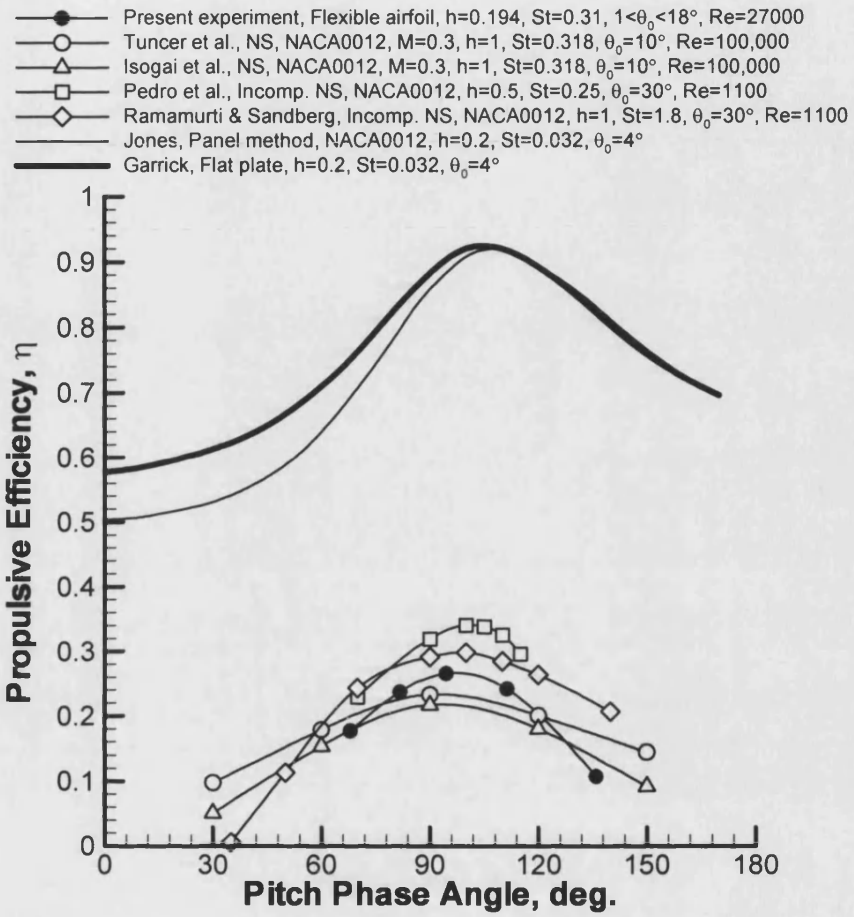

Figure 5.15: Propulsive efficiency as a function of pitch phase angle. Comparison of present experimental results with linear theory, panel method and both compressible and incompressible Navier-Stokes codes. The pitch amplitude, θ_0, is variable for the present experiment, and fixed for all other data series. Optimum phase angles in the vicinity of 90 degrees are found over a wide range of techniques and parametric values. Tuncer et al.[70], Isogai et al.[15], Pedro et al.[28], Ramamurti & Sandberg[71], Jones et al.[43], Garrick[9].

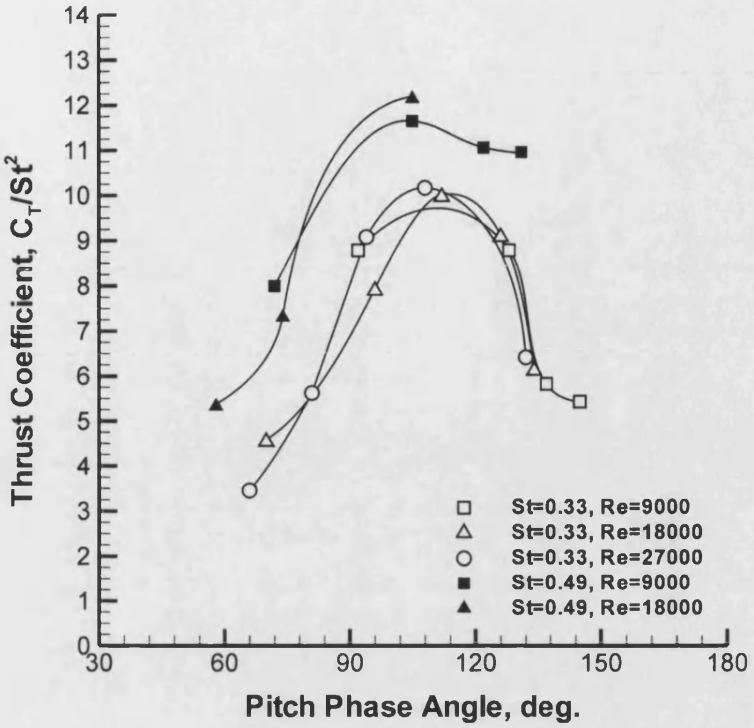

(a)

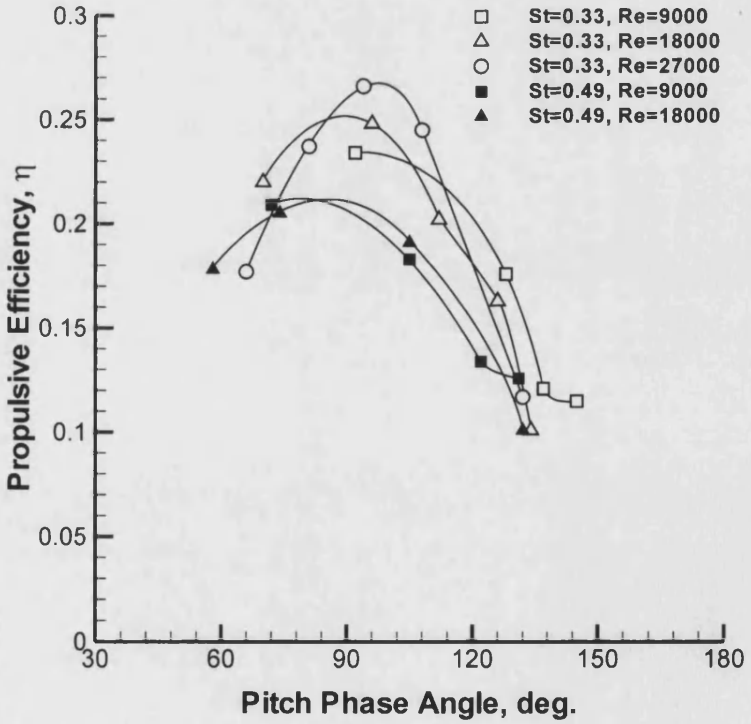

(b)

Figure 5.16: The variation with pitch phase angle of (a) Thrust coefficient and (b) Propulsive efficiency. Curves are shown for St=0.33 (open symbols) and St=0.49 (closed symbols). The effect of Reynolds number is observed to be small.

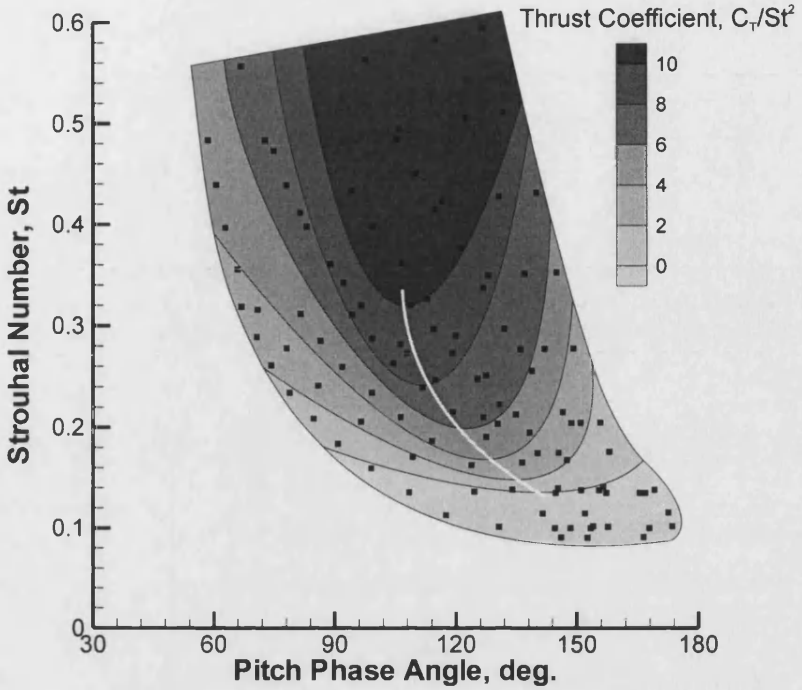

(a)

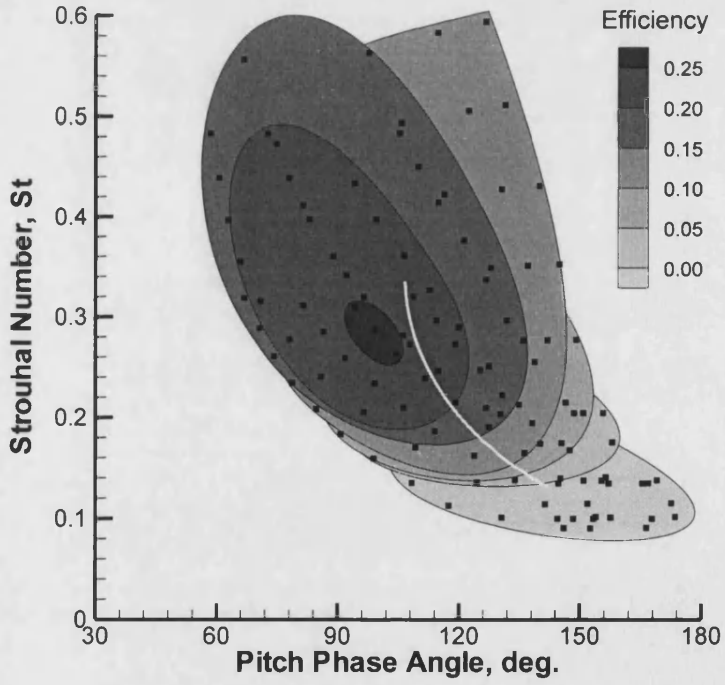

(b)

Figure 5.17: Contours of (a) Thrust coefficient and (b) Propulsive Efficiency, in the Strouhal Number – Pitch Phase Angle plane. Black dots indicate experimental data points. The complete set of data is plotted (all stiffnesses, frequencies and Reynolds numbers). The solid white line indicates the peak thrust coefficient for a given Strouhal number.

6 EFFECT OF SPANWISE FLEXIBILITY ON FLAPPING WING PROPULSION

6.1 SUMMARY

A water tunnel study of three heaving rectangular NACA0012 wings of varying spanwise flexibility has been carried out. Measurements of thrust and efficiency were obtained with a force balance. For the same oscillation amplitude and frequency, the wing of intermediate stiffness is found to experience a significantly greater thrust than the inflexible wing. When a Strouhal number is defined based on the heave amplitude one half-span from the root, a peak in efficiency is observed for St≈0.2. For Strouhal numbers greater than 0.2, the efficiency of the wing of intermediate stiffness exceeds the efficiency of the inflexible wing, indicating an efficiency benefit to flexibility. (Strouhal numbers for birds, bats, insects and aquatic mammals range from 0.2 to 0.4.) The origin of the efficiency benefit is found to be a marginally higher thrust, and marginally lower power requirement. The highly flexible wing experiences a low thrust and efficiency. In this case, the tip and root displacements are observed to be out of phase. From a design aspect, flexibility may benefit flapping wing Micro Air Vehicles both aerodynamically and in the inherent lightness of flexible structures.

6.2 AIM

The effect of chordwise flexibility for an airfoil in heave at low Reynolds numbers has been studied in the previous chapters. The progression to a study of spanwise flexibility follows naturally. The aim of this chapter is to measure the effect of spanwise flexibility on the thrust and efficiency characteristics of a rectangular

NACA0012 wing oscillated in heave. The heave amplitude, 'h', where $h=a_{ROOT}/c=0.175$, is constant for all experiments. Three additional dimensionless parameters arise: the Reynolds number, reduced frequency, k_G, and Strouhal number based on the amplitude of the mid span.

Since in all experiments the bending mode was observed to be first order, the deformation of the wing is described by the tip amplitude and tip phase, relative to the amplitude and phase of the root.

6.3 RESULTS

The current section falls broadly into two parts. One discusses the effect of the Strouhal and Reynolds numbers and one, with the aim of bringing physical insight, discusses a single case (Re=30,000, $k_G=1.82$).

6.3.1 DEFORMATION – SINGLE CASE

The shape response of the three wings for the single case of Re=30,000, $k_G=1.82$ is represented in Figure 6.1. In Figure 6.1(a) the trailing-edge of the wing is shown at equal time intervals. For each of the Inflexible, Flexible and Highly Flexible wings, the downstroke is shown (T=0 to T=1/2) and then the upstroke (T=1/2 to T=1). The direction from root to tip is left to right. The path of the root is identical in each diagram ($s_{ROOT}=a_{ROOT}Cos(\omega t)$); the path of the wing tip ($s_{TIP}\approx a_{TIP}Cos(\omega t+\varphi)$) depends on the flexibility of the wing. It is seen in Figure 6.1(a)(i) that the stiffest of the three wings bends relatively little ($a_{TIP}/a_{ROOT}=1.13$, $\varphi=-4^o$). The wing tip moves in the same direction as the wing root for 98% of the cycle. The Flexible wing (part (ii)) is seen to curve more, and the tip amplitude is visibly greater than the root amplitude ($a_{TIP}/a_{ROOT}=1.64$, $\varphi=-25^o$). The wing tip moves in the same direction as the wing root for 86% of the cycle. The highly flexible wing (part iii) is seen to curve relatively steeply ($a_{TIP}/a_{ROOT}=1.76$, phase delay=117°). The wing tip moves in the same direction as the wing root for only 35% of the cycle. For the majority of the cycle the root and tip move in opposite directions. The tip amplitudes and phase angles for the three flexibilities are summarised in Table 6-1.

In Figure 6.1(b) the tip displacements of the three wings are plotted over a period of two cycles. Symbols represent experimental data points. Cosine wave fits for the three wing tips, and for the root are drawn. The cosine fit is seen to be a good approximation to the displacement of the tip, indicating the suitability of representing the tip displacement in the form $a_{TIP}Cos(\omega t+\varphi)$. The wing tip curves lie to the right of the root displacement curve, indicating a negative value of the tip phase angle 'φ'. The plot illustrates the steep increase in tip amplitude moving from the Inflexible to the Flexible wing, with only a small increase in tip phase lag, and the slight increase in tip amplitude moving from the Flexible to the Highly Flexible wing, with a large increase in tip phase lag.

Wing	k_G	St	a_{TIP}/a_{ROOT}	φ	C_T	C_P	η
Inflexible	1.82	0.234	1.13	-4.2°	0.21	1.23	0.17
Flexible	1.82	0.280	1.64	-25.1°	0.32	1.88	0.17
Highly Flexible	1.82	0.162	1.76	-117°	0.11	0.79	0.14

Table 6-1: Statistics for the three wings; Re=30,000.

6.3.2 DEFORMATION – PARAMETRIC STUDY

The variation of the shape response with Reynolds number and frequency is presented in Figure 6.2. In Figure 6.2(a) the variation of tip amplitude with frequency is shown for a single Reynolds number. The variation of tip phase with frequency is plotted in Figure 6.2(b) for the same Reynolds number. In part (c) the frequency parameter is eliminated: tip amplitude is plotted against tip phase. Each data point corresponds to a test at a different frequency; the direction of increasing frequency is indicated. It is noted that the case of Figure 6.1 (Re=30,000, k_G=1.82) corresponds to the right-most data point on the k_G axes of Figure 6.2(a) and Figure 6.2(b), and of the right-most data point on the phase axis of Figure 6.2(c). It is seen in Figure 6.2(a) that the tip amplitude of all three wings tends to unity as the frequency approaches zero. It is also seen that the tip amplitude of both the Inflexible and Flexible wings increases with oscillation frequency over the whole frequency range. The rate of increase is initially small, but increases with frequency. The tip amplitude of the Highly Flexible wing increases moderately quickly for low frequencies, and rapidly at intermediate frequencies. At higher frequencies the tip amplitude reaches a maximum and then

decays. The reason for the peak in tip amplitude may be seen with reference to Figure 6.2(b), in which the tip phase angle is plotted against frequency. The Highly Flexible wing is observed to behave strikingly differently to the Inflexible and Flexible wings: the tip phase is far higher throughout the whole frequency range. The rapidly increasing tip phase lag is responsible for the peak in tip amplitude seen in the Figure 6.2(a): with increasing frequency the curvature of the wing increases (favourable in terms of the tip amplitude) but the point in the cycle at which the greatest curvature occurs becomes rapidly unfavourable. The difference between the Highly Flexible wing and the Inflexible and Flexible wings is further illustrated with reference to Figure 6.2(c). The Inflexible and Flexible wing data lie on a line (the Inflexible data points are obscured by the Flexible ones). The Highly Flexible data points lie on three curves, which generally lie to the right of the line (there is a small degree of overlap). It is also seen that, for the Highly Flexible wing, two tip phase angles may yield the same tip amplitude.

6.3.3 THRUST FORCE – SINGLE CASE

Instantaneous thrust coefficient curves for the case Re=30,000, k_G=1.82, are shown in Figure 6.3 for a period of two oscillations. Two peaks in thrust are observed per oscillation for the Inflexible and Flexible wings, one for the upstroke and one for the downstroke. This is consistent with the shedding of two vortices per cycle (see Chapter 4). It is seen that the thrust coefficient of the Flexible wing is greater than that of the Inflexible wing, indicating that introducing a degree of spanwise flexibility increases the thrust coefficient for this Reynolds number and frequency. It is also seen that the thrust coefficient of the Highly Flexible wing is the lowest of the three. Two interesting features are observed for the Highly Flexible wing. Firstly, multiple peaks in thrust are observed and, secondly, the instantaneous thrust coefficient is always positive. The high curvature of the wing, and the different velocities (and hence effective angles of attack) along the span, may create an interesting vortex shedding pattern. The time-averaged thrust coefficients are shown in Table 6-1. Compared to the Inflexible wing, the Flexible wing experiences a 50% thrust benefit, whereas the Highly Flexible wing experiences a 50% deficit.

In summary, the flexibility of a wing is seen to greatly affect the thrust characteristics of the wing. The tip phase angle is seen to be an important parameter: despite the tip amplitude being approximately equal for the Flexible and Highly Flexible wings, the forces differ by a factor of three.

6.3.4 FORCE – PARAMETRIC STUDY

In order to establish whether the Flexible wing experiences greater thrust over a range of Reynolds numbers and frequencies, a parametric study was carried out. The complete set of thrust coefficient data for Re=30,000 is plotted in Figure 6.4(a). Again, the single case discussed above corresponds to the highest frequency in Figure 6.4(a). It is seen that the benefit in thrust for the Flexible wing over the Inflexible wing persists to lower frequencies, and likewise for the detriment in thrust for the Highly Flexible wing. At the lowest frequencies the wings experience drag. In the limiting case (stationary wing) the thrust coefficient is C_T=-0.024.

An alternative to the Garrick frequency parameter 'k_G' is the Strouhal number, 'St'. With the concept of effective amplitude, the characteristic length chosen here is the amplitude of the mid span, giving $St=2fa_{MID}/U_0$. It is noted that the quantity is closely related to the peak effective angle of attack at the mid span, $\tan^{-1}(2\pi fa_{MID}/U_0)$. From here on, the Strouhal number will supersede the Garrick frequency. For high tip phase lags the physical meaning of the Strouhal number expires (for out of phase motions the amplitude of the mid point may be very small, but the amplitude of the root and tip may be large). For this reason, data for which the tip phase angle exceeds 60 degrees is omitted.

In Figure 6.4(b), thrust coefficient is plotted against Strouhal number. A striking feature is that the thrust coefficient curves for the Inflexible and Flexible wings collapse. This indicates the appropriateness of the Strouhal number for characterising the thrust coefficient of stiff to moderately flexible wings undergoing pure heave oscillations. Plots for all Reynolds numbers are shown in Figure 6.4(c). Near collapse of the data is seen for the Inflexible and Flexible wings. The Flexible wing is observed to experience a marginally higher thrust coefficient for high Strouhal numbers. Only a very weak Reynolds number dependence is observed, consistent

with the findings of the previous chapter. The Highly Flexible wing is seen to deviate from the Inflexible and Flexible data. The divergence is greatest for the highest tip phase lags.

In summary, the thrust coefficient is found to be a function of Strouhal number based on the amplitude of the mid span of the wing, and to be a very weak function of Reynolds number.

6.3.5 POWER INPUT

Power input coefficient is plotted as a function of Strouhal number for Re=30,000 in Figure 6.5(a). Near complete data collapse is observed for all wings, showing that the Strouhal number is appropriate for characterising the power requirements of the heave motion, as well as the thrust characteristics. A marginally higher power coefficient for the Inflexible wing at high Strouhal numbers is observed. In Figure 6.5(b) the power input coefficient is plotted for all Reynolds numbers. Data collapse is observed: power coefficient is seen to be entirely independent of Reynolds number. Again, a marginally higher power coefficient for the Inflexible wing at high Strouhal numbers is noted.

6.3.6 EFFICIENCY

Propulsive efficiency, 'η', is plotted as a function of Strouhal number in Figure 6.6. The shape of the curve is typical of those found in experimental studies. The general trend is for efficiency to fall with increasing Strouhal number (also consistent with inviscid theory[9]). At low Strouhal numbers the efficiency falls rapidly due to viscous drag. A peak in efficiency occurs at a Strouhal number of approximately 0.2, consistent with experimental studies in the literature[33], and equal to those found for birds, bats and insects[42]. The Strouhal numbers of fish and aquatic mammals[42] range from 0.2 to 0.4. The effect of Reynolds number is small. The efficiency increases slightly with Reynolds number, consistent with diminishing viscous effects. The trend originates from slightly higher thrust coefficient for higher Reynolds numbers.

Around the peak in efficiency the Inflexible and Flexible wings perform similarly. The Highly Flexible wing performs poorly, a consequence of a low thrust characteristic. At higher Strouhal numbers, the Flexible wing has the highest thrust coefficient. The origin is a slightly higher thrust, and moderately lower power requirement. It is noted that the range of Strouhal numbers over which a degree of flexibility is beneficial is equal to the Strouhal number range of birds, bats, insects, fish and aquatic mammals. This suggests that wing flexibility may be beneficial to bird flight aerodynamically. It is also of relevance to the design of Micro Air Vehicles.

6.3.7 FURTHER COMPARISONS

A thrust coefficient comparison of two and three dimensional cases is plotted in Figure 6.7. The two-dimensional case is for a wing similar to the three-dimensional wing but with a span of 400mm rather than of 300mm, and with end plates at both ends. The data is seen to fall onto two distinct curves, one for the two-dimensional case (higher thrust) and one for the three-dimensional case. Mirroring the thrust coefficients, the efficiency (not shown) of the two-dimensional case is found to exceed the efficiency of the three-dimensional case for all Strouhal numbers. The peak efficiency is 28% for the two-dimensional case and 21% for the three-dimensional case.

A further interesting comparison is between the efficiency of the Inflexible two-dimensional case and the Flexible three-dimensional case. The two sets of curves are shown in Figure 6.8. The two-dimensional Inflexible wing efficiency is greater for Strouhal numbers in the vicinity of the optimum. At higher Strouhal numbers, however, the efficiency of the Flexible 3D wing reaches that of the two-dimensional case.

6.4 CONCLUSIONS

A study of the effect of Reynolds number and Strouhal number on the thrust, lift and propulsive efficiency of a flexible flapping wing has been performed. The wing has an aspect ratio of 3, NACA0012 profile, rectangular planform and is oscillated in heave at one end. An end plate near the root gives an effective aspect ratio of 6. Experiments

were carried out in a water tunnel over a Reynolds number range of 10,000 to 30,000. A two component force balance was used to obtain the thrust and efficiency characteristics of the wing. A set of validation tests yielded results in close agreement with existing experimental and numerical data. Three wings of varying spanwise stiffness were tested. All were rigid in the chordwise direction.

Introducing a degree of flexibility in the spanwise direction was found to increase the effective heave amplitude. When thrust coefficient is plotted against reduced frequency, a limited degree of flexibility is observed to be greatly beneficial. A thrust benefit of 50% is observed for a wing of intermediate flexibility. For a highly flexible wing, however, the tip is observed to move out of phase with the root, and a diminished thrust coefficient is recorded.

When the thrust coefficient is plotted against a Strouhal number based on the amplitude of the mid-span, the data collapses for stiff to moderately flexible wings. A slight deviation is observed at high Strouhal numbers, where the thrust coefficient of the flexible wing is slightly higher. A very weak dependence on Reynolds number is observed. The plots of power input against Strouhal number are found to collapse for all wings and all Reynolds numbers. A slight deviation is observed at high Strouhal numbers, where the power requirements of the intermediate wing are slightly lower. The efficiency of stiff to moderately flexible wings was found to be similar in the region of peak efficiency. The Strouhal number corresponding to the peak in efficiency, St=0.2, is consistent with experimental findings in the literature. A degree of flexibility is found to increase efficiency for Strouhal numbers greater than 0.2. Strikingly, this range coincides with the range of Strouhal numbers found in nature. The overly flexible wing is characterised by large tip phase lags, and performs relatively poorly. A slight increase in efficiency with Reynolds number is observed, consistent with declining viscous effects.

The findings of this chapter suggest that birds, bats and insects may benefit aerodynamically from the flexibility of their wings. From a design aspect, flexibility may benefit MAVs both aerodynamically and in the inherent lightness of flexible structures.

6.5 FIGURES

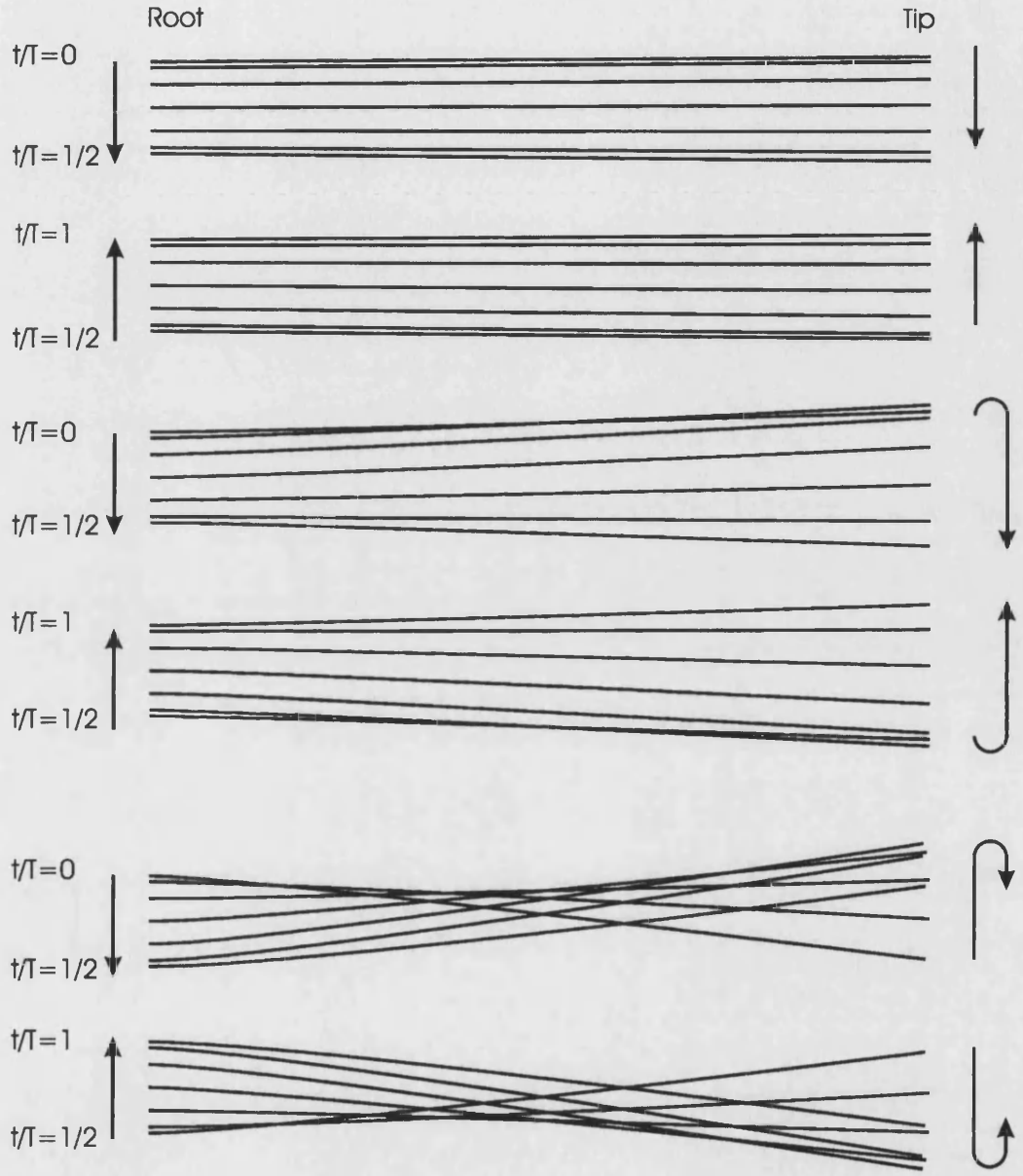

(a)

Figure 6.1: (a): Visualisation of the spanwise deformation for the Inflexible (Top), Flexible (Middle), and Highly Flexible (Bottom) wings during the downstroke ($0<t/T<0.5$) and the upstroke ($0.5<t/T<1$). The arrows indicate the direction of motion of the root (left hand side) and tip (right hand side); Re=30,000, k_G=1.82. (b): Tip displacements as a function of time; Re=30,000, k_G=1.82.

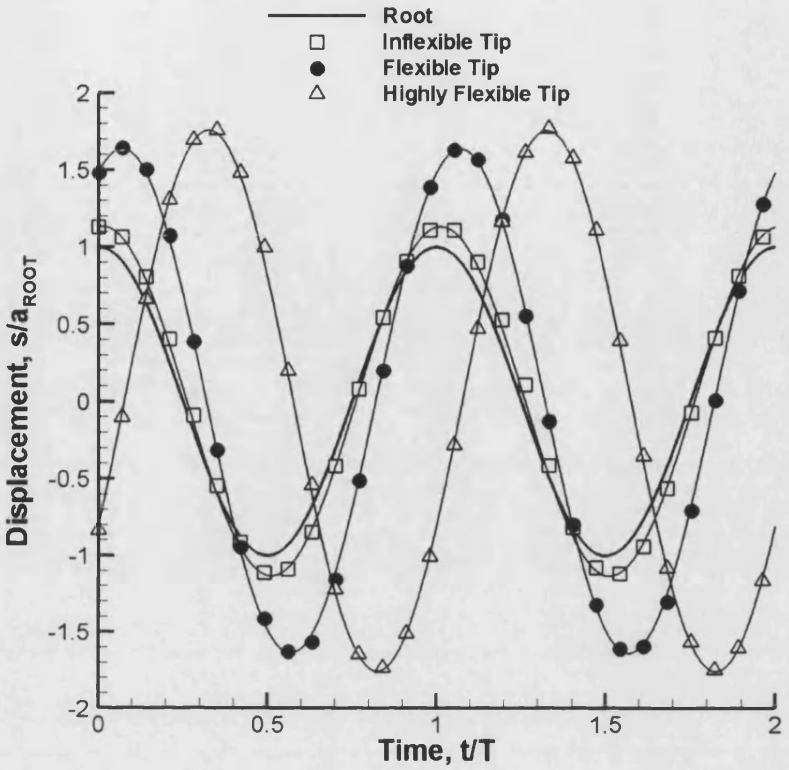

(b)

Figure 6.1 Cont.

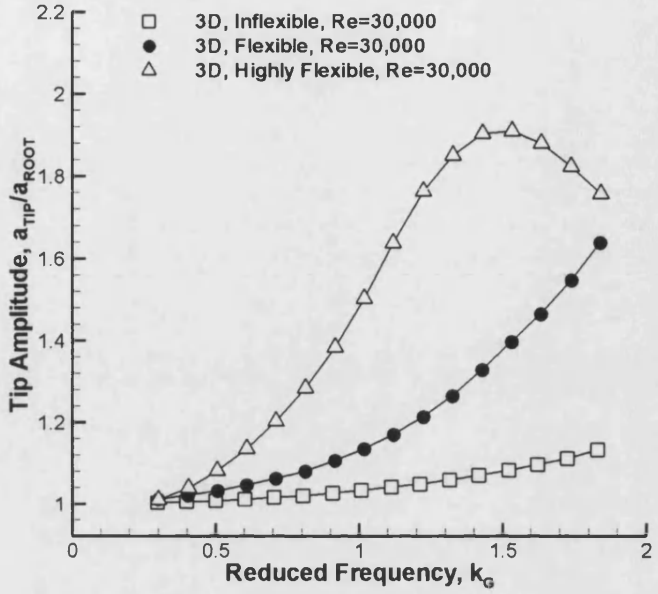

(a)

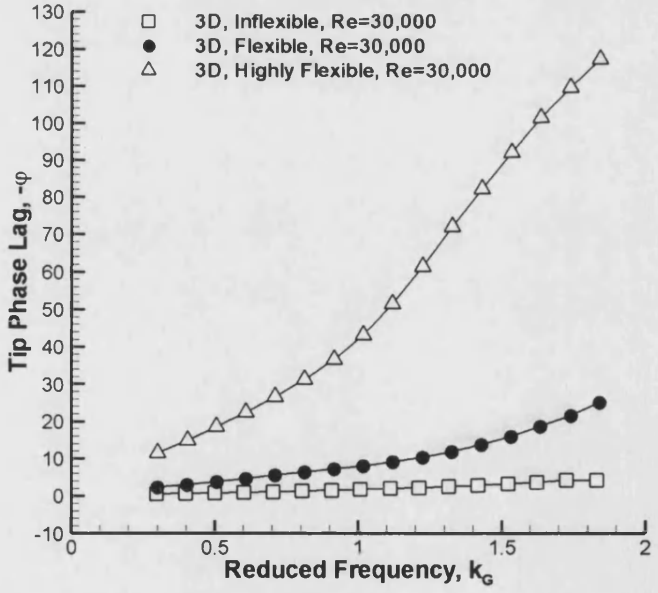

(b)

Figure 6.2: (a): Tip amplitude as a function of Garrick frequency; Re=30,000. (b): Tip phase lag as a function of Garrick frequency; Re=30,000. (c): Tip amplitude as a function of tip phase lag. Each data point represents a test at a different frequency.

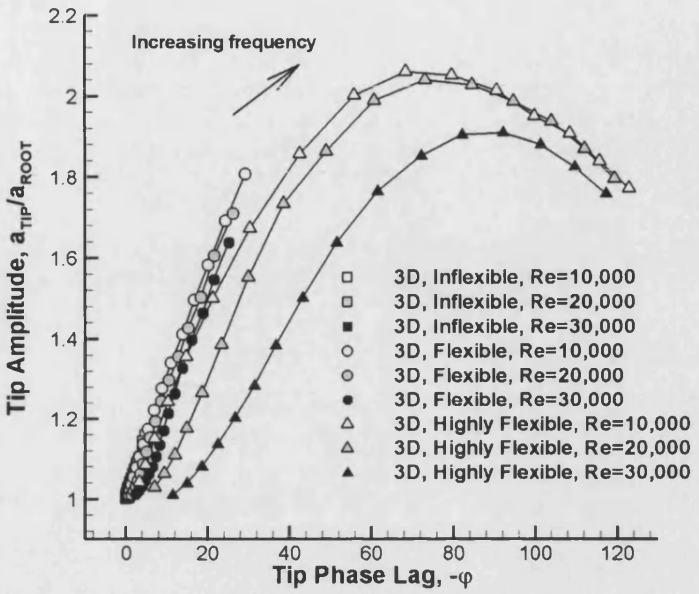

(c)

Figure 6.2 Cont.

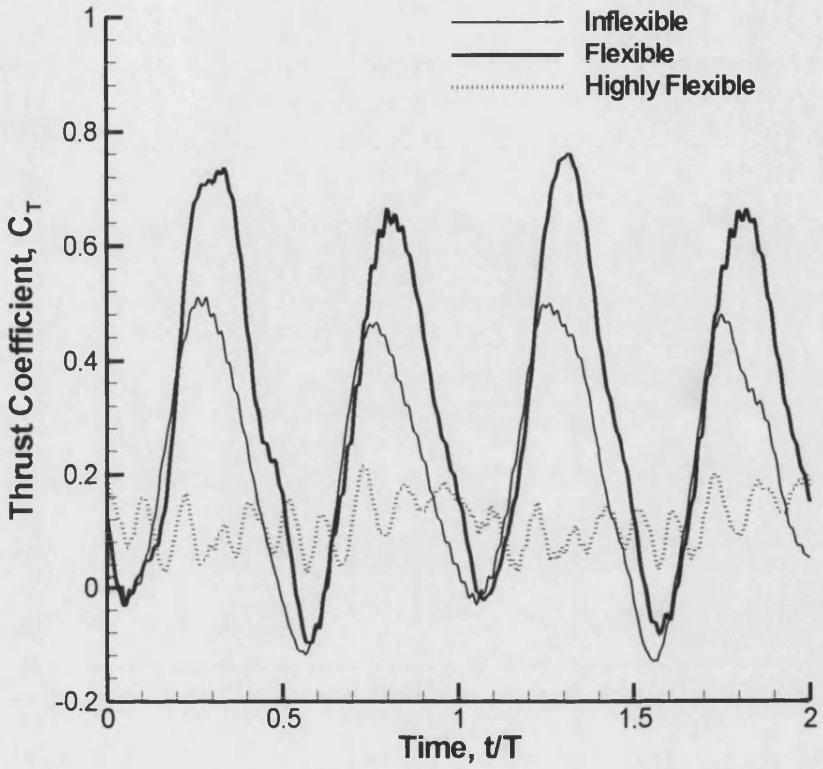

Figure 6.3: Instantaneous thrust coefficient as a function of time over two heave cycles; 3D, Re=30,000, k_G=1.82.

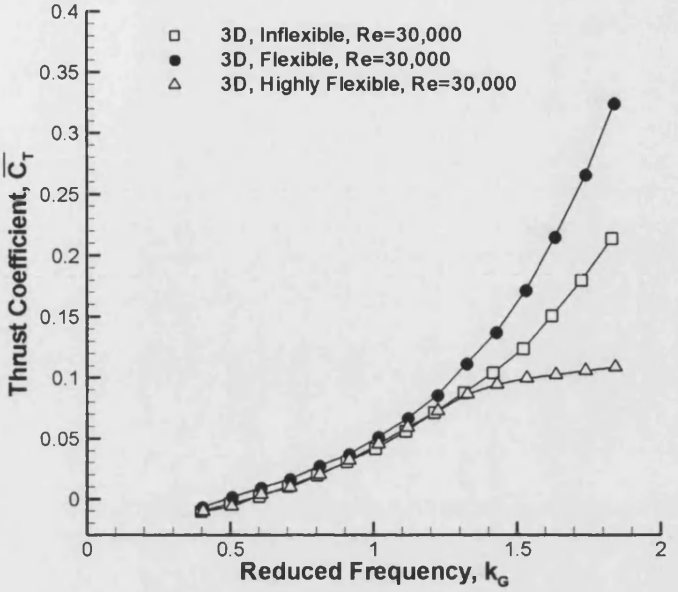

(a)

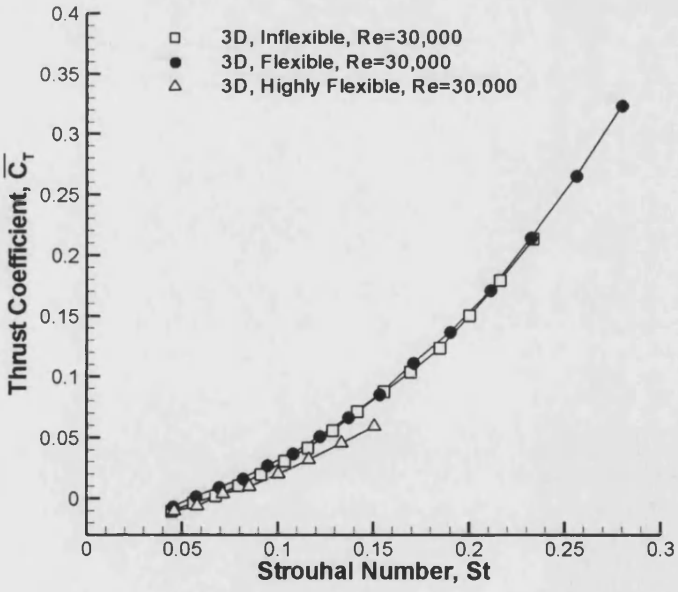

(b)

Figure 6.4: (a): Average thrust coefficient as a function of Garrick frequency; Re=30,000. (b): Average thrust coefficient as a function of Strouhal number based on the excursion of the mid span; Re=30,000. (c): Average thrust coefficient as a function of Strouhal number. All Reynolds numbers.

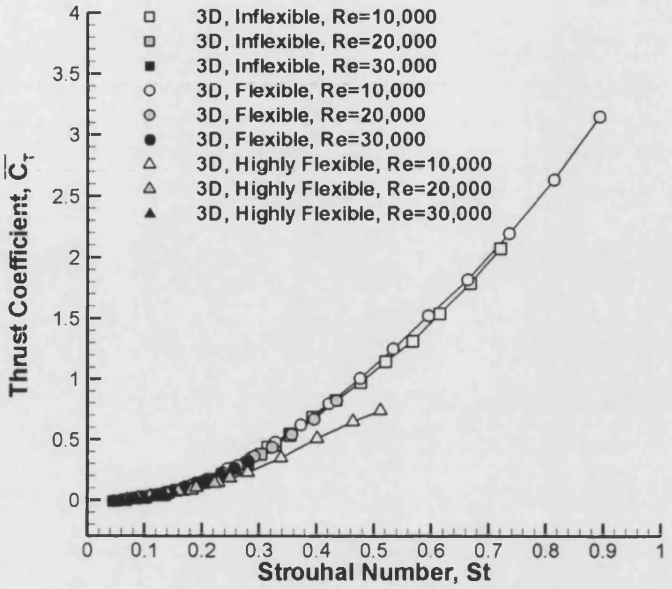

(c)

Figure 6.4 Cont.

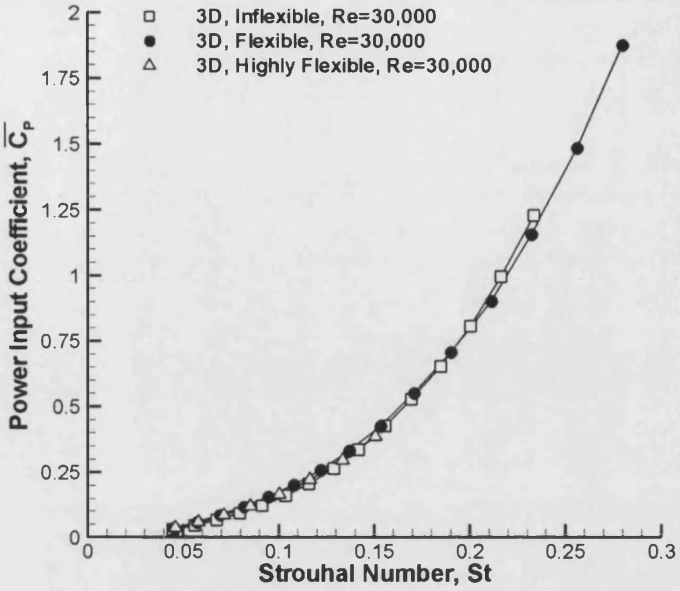

(a)

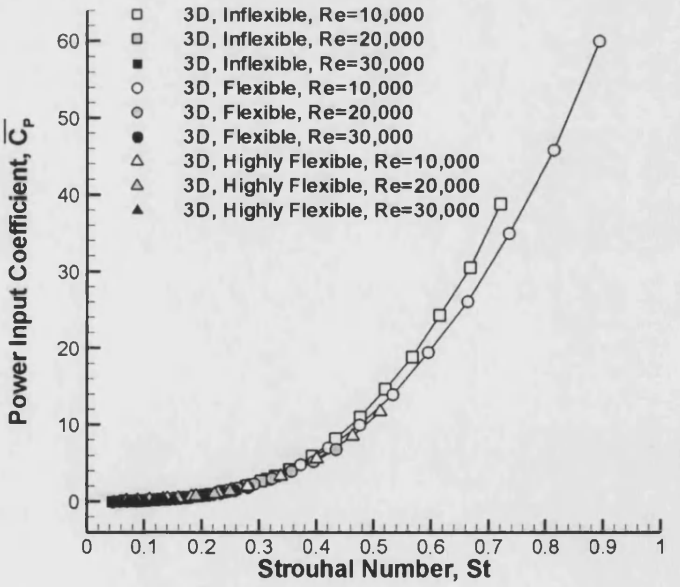

(b)

Figure 6.5: (a): Average power input coefficient as a function of Strouhal number; Re=30,000. (b): Average power input coefficient as a function of Strouhal number. All Reynolds numbers.

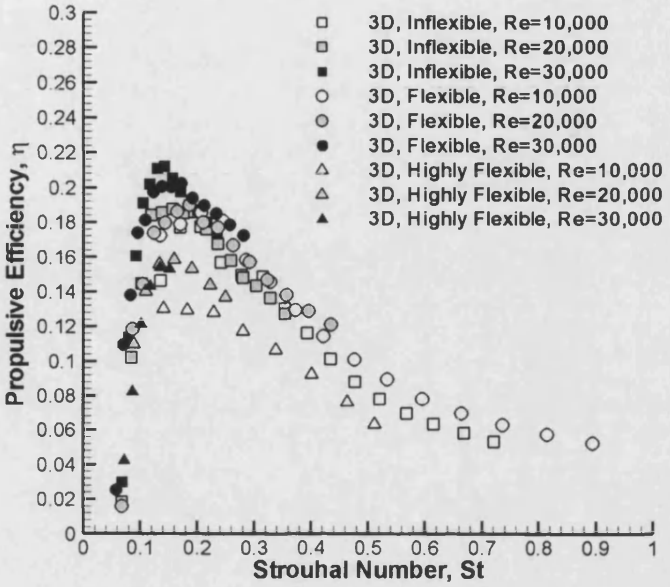

Figure 6.6: Propulsive efficiency as a function of Strouhal number.

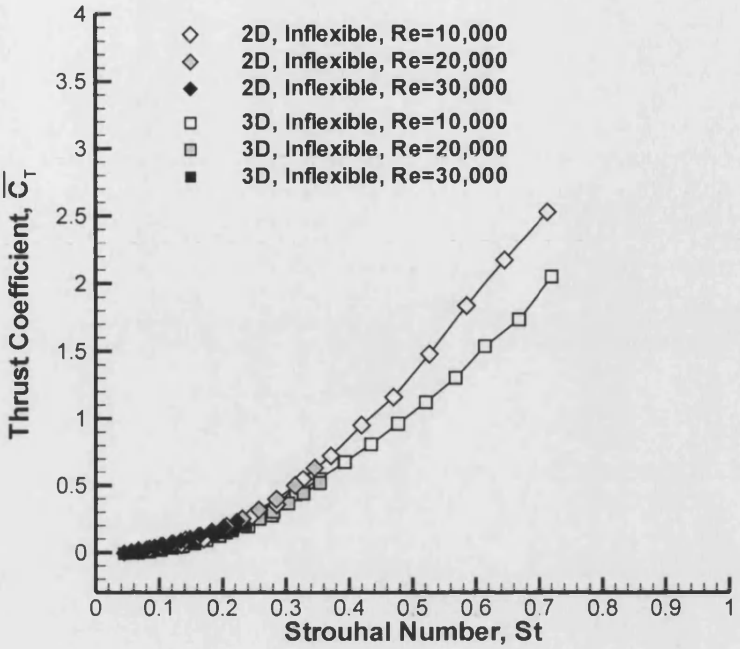

Figure 6.7: Average thrust coefficient as a function of Strouhal number. Comparison between 2D and 3D.

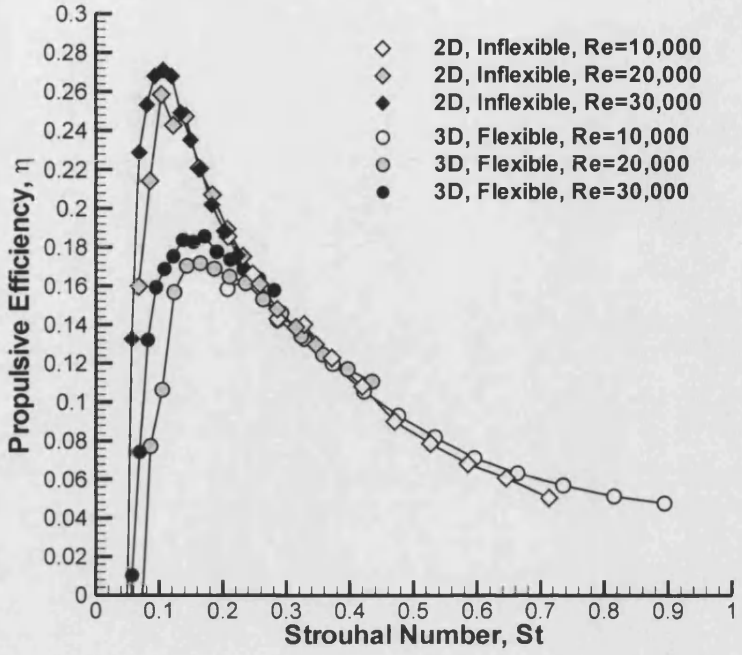

Figure 6.8: Propulsive efficiency as a function of Strouhal number. Comparison of 2D Inflexible and 3D flexible cases.

7 CONCLUSIONS

The findings of the four chapters of results are reviewed in this section.

7.1 ZERO FREESTREAM VELOCITY

The aim of the first chapter of results was to establish whether chordwise flexibility provided any aerodynamic benefit for a two-dimensional airfoil in the case of zero freestream velocity. The case of zero freestream velocity corresponds in nature to hovering flight. Experiments were carried out in a water tank for three chordwise-flexible airfoils: one essentially inflexible, one of intermediate flexibility, and one exceptionally flexible. The flow field was studied with PIV apparatus, and measurements of the thrust force were obtained with a strain gauge force balance. The deformation of the flexible airfoils was found to increase with oscillation frequency, both in terms of the deformation amplitude and phase. The phase of the deformation was found to be such that the airfoil was inclined to the flow, thus reducing the effective angle of attack. The vortical flows from the three airfoils were found to be different. Vortex pairs were observed to be shed from the stiff airfoils, whereas a reverse von Kármán street was observed for the highly flexible airfoil. The circulation of the trailing-edge vortices, and the time-averaged momentum flux, were found to be greatest for the intermediate airfoil. The indications of improved performance for the wing of intermediate flexibility were confirmed with direct force measurements. The greatest thrust coefficients were found for the wing of intermediate stiffness. These findings suggested the existence of an optimum wing flexibility. Finally, a significantly improved performance in terms of thrust/power-input ratio was observed, a characteristic which may be attributed to the lower effective angles of attack.

7.2 JET SWITCHING PHENOMENON

The aim of the second chapter of results was to investigate the phenomena of deflected jets and jet switching for a two-dimensional airfoil in pure heave. Experimental findings in the literature show the deflected jet phenomenon, where the vortices from an oscillating airfoil lie at an angle to the freestream direction, to occur at high non-dimensional frequencies. The case of fluid at rest is the case of infinite Strouhal number. Experimental studies in the literature have found the direction of the jet to switch apparently randomly. Inviscid numerical simulations have simulated deflected wakes, although the direction of the jet is reported to be stable in one direction. One viscous simulation has predicted the jet to switch, although information about the periodicity of the switching, if any exists, is not given. Experiments were conducted in a water tank, and also in open air. A time history of the direction of the jet was obtained with LDV measurements. The vortex pattern downstream of the trailing-edge was captured with PIV measurements. Deflected jets were observed, and the angle of the jet was seen to change periodically. It is believed that the observation of periodic switching has not been reported in the literature to date. The switching period was found to depend on the heave frequency and amplitude and the stiffness of the airfoil; in general, the switching period was found to increase with increasing stiffness and decreasing frequency and amplitude. Over the ranges of stiffness, frequency and amplitude tested, the switching period was found to be two orders of magnitude greater than the heave period. Jet switching was still observed in pseudo 2D open-air smoke flow visualisation experiments, indicating that wall effects were not responsible for the switching phenomenon. The deflection of the jet, and thus the jet switching effect, was found to diminish for Strouhal numbers less than 0.34.

7.3 LOW REYNODS NUMBERS

In order to establish whether the benefits found to chordwise flexibility also applied in the case of non-zero Reynolds number, experiments were carried out in a water tunnel for Reynolds numbers of 9000-27000, constant heave amplitude, and for seven airfoil flexibilities. Flexibility was again found to yield benefits in terms of thrust coefficient. Peaks were observed at intermediate values of the plate thickness (constant Strouhal number), and also at intermediate values of the Strouhal number (constant thickness), indicating the optimum stiffness has a frequency dependence. The instantaneous wake

patterns corresponding to the optimum cases exhibited strong vortices, while the time-averaged jets were broader and higher velocity. The jets tended to become deflected at higher Strouhal numbers, consistent with the findings of the earlier chapters. Efficiency benefits were observed over a broad range of flexibility, with the optimum efficiency exceeding the efficiency of the inflexible airfoil by approximately 15%. Flow visualisation experiments showed the magnitude of the leading-edge vortices to be weaker in the flexible cases. The analogy was made with a rigid airfoil oscillating in coupled heave and pitch. The three shape characteristics - pitch phase angle, pitch amplitude and trailing-edge amplitude - were found to be interdependent. Points from measurements at all Reynolds numbers, plate thicknesses and heave frequencies were found to lie on a single line (pitch amplitude vs pitch phase angle) or a single curve (trailing-edge amplitude vs pitch phase angle). The phase angle of the "pitch" was found to lead the heaving motion. This finding was of significance because it is also the case in nature: the pitch motion of the fins of fish and aquatic mammals leads the heave motion by a phase angle of approximately 90 degrees. Thrust coefficient and propulsive efficiency were found to be functions of the Strouhal number and pitch phase angle. The effect of Reynolds number over the range $9000<Re<27000$ was found to be small. Contour plots of efficiency in the Strouhal number-pitch phase angle plane exhibited a distinct peak for a pitch phase angle of 95-100 degrees, (consistent with experimental and Navier-Stokes analyses of rigid airfoils in coupled heave and pitch) and a Strouhal number of 0.29, which lies in the middle of the range observed in nature. Contours of thrust coefficient exhibited a peak for a pitch phase angle of 110-120 degrees, higher than the value found to maximise efficiency and again consistent with studies of rigid wings in coupled motions in the literature. Flow visualisation indicated that leading-edge flow separation and vortex shedding may be responsible for a decline in efficiency.

7.4 SPANWISE FLEXIBILITY

The final chapter addressed the issue of spanwise flexibility, where it was noted that the fins of fish and aquatic mammals are flexible to some degree along the span. The chapter was unlike the previous, two-dimensional, investigations. Experiments were carried out with three NACA0012 airfoils of varying spanwise flexibility. All were inflexible in the chordwise direction. The wings were oscillated at the root in pure heave. Experiments were performed over a Reynolds number range of 10,000-30,000.

Introducing a degree of flexibility in the spanwise direction was found to increase the effective heave amplitude. A limited degree of flexibility was observed to be greatly beneficial in terms of thrust; a benefit of 50% was observed for a wing of intermediate flexibility. For the highly flexible wing, however, the root and tip were observed to move out of phase, and the thrust coefficient diminished.

When thrust coefficient was plotted against a Strouhal number based on the amplitude of the mid-span, as opposed to the amplitude of the root, the data was found to collapse for stiff to moderately flexible wings. A slight deviation was observed at high Strouhal numbers, where the thrust coefficient of the flexible wing was slightly higher. The plots of power input against Strouhal number were found to collapse for all wings and all Reynolds numbers. A slight deviation was observed at high Strouhal numbers, where the power requirements of the intermediate wing were slightly lower. The variation of thrust coefficient with Reynolds number was found to be very small. A slight increase in efficiency with Reynolds number was observed, consistent with declining viscous effects. A degree of flexibility was found to increase efficiency for Strouhal numbers greater than 0.2. Strikingly, this range coincides with the range of Strouhal numbers found in nature. The efficiency of the highly flexible airfoil was relatively low, and attributed to the large phase lag between the root and tip.

7.5 CLOSING COMMENTS

This thesis has described the results of a set of experiments on the effect of chordwise and spanwise flexibility on the thrust and efficiency characteristics of a heaving airfoil. The findings suggest that birds, bats and insects may benefit aerodynamically from the flexibility of their wings. From a design aspect, flexibility may benefit Micro Air Vehicles both aerodynamically and in the inherent lightness of flexible structures. A number of avenues of further work exist, one of which is to study in closer detail the leading-edge vortices, with PIV or dye flow visualisation techniques. A further potential area of work is to consider an airfoil with varying plate thickness. With appropriate stiffness variation, it may be possible to tune the wing to high efficiency.

8 PUBLICATIONS AND AWARDS

8.1 CONFERENCE PROCEEDINGS

[I] S. Heathcote and I. Gursul, "Flexible flapping wing propulsion at zero freestream velocity," presented at 33rd AIAA Fluid Dynamics Conference and Exhibit, Orlando, Florida, AIAA Paper 2003-3446, June 2003.

[II] S. Heathcote and I. Gursul, "Jet switching phenomenon for a plunging airfoil," presented at 34th AIAA Fluid Dynamics Conference and Exhibit, Portland, Oregon, AIAA Paper 2004-2150, June 2004.

[III] S. Heathcote and I. Gursul, "Flexible flapping airfoil propulsion at low Reynolds numbers," presented at 43rd AIAA Aerospace Sciences Conference and Exhibit, Reno, Nevada, AIAA Paper 2005-1405, January 2005.

[IV] S. Heathcote, Z. Wang, and I. Gursul, "Effect of Spanwise Flexibility on Flapping Wing Propulsion," accepted for presentation at 36th AIAA Fluid Dynamics Conference and Exhibit, San Francisco, AIAA Paper 2006-2870, June 2006.

8.2 JOURNAL PUBLICATIONS

S. Heathcote, D. Martin, and I. Gursul, "Flexible flapping airfoil propulsion at zero freestream velocity," AIAA Journal, vol. 42, pp. 2196-2205, 2004.

8.3 AWARDS

AIAA 2005 Best Paper – Fluid Dynamics: "Flexible flapping airfoil propulsion at low Reynolds numbers," presented at 43rd AIAA Aerospace Sciences Conference and Exhibit, Reno, Nevada, 2005.

9 REFERENCES

[1] T. N. Pornsin-sirirak, Y. C. Tai, H. Nassef, and C. M. Ho, "Titanium-alloy MEMS wing technology for a micro aerial vehicle application," *Sensors and Actuators A: Physical*, Vol. 89, No. 1-2, 2001, pp. 95-103.

[2] B. Peterson, B. Erath, K. Henry, M. Lyon, B. Walker, N. Powell, K. Fowkes, and W. J. Bowman, "Development of a Micro Air Vehicle for Maximum Endurance and Minimum Size," AIAA Paper 2003-416, *41st Aerospace Sciences Meeting and Exhibit*, 2003.

[3] P. G. Ifju, D. A. Jenkins, S. Ettinger, Y. Lian, W. Shyy, and M. R. Waszak, "Flexible-Wing-Based Micro Air Vehicles," AIAA Paper 2002-0705, *40th AIAA Aerospace Sciences Meeting & Exhibit*, 2002.

[4] G. R. Spedding and P. B. S. Lissaman, "Technical aspects of microscale flight systems," *Journal of Avian Biology*, Vol. 29, No. 4, 1998, pp. 458-468.

[5] T. J. Mueller and J. D. DeLaurier, "Aerodynamics of Small Vehicles," *Annu. Rev. Fluid Mech.*, Vol. 35, 2003, pp. 89-111.

[6] R. Knoller, "Die Gesetze des Luftwiderstandes," *Flug-und Motortechnik (Wien)*, Vol. 3, No. 21, 1909, pp. 1-7.

[7] A. Betz, "Ein Beitrag zur Erklaerung des Segelfluges," *Zeitschrift fuer Flugtechnik und Motorluftschiffahrt*, Vol. 3, No. 21, 1912, pp. 269-272.

[8] R. Katzmayr, "Effect of Periodic Changes of Angle of Attack on Behavior of Airfoils," Technical Memorandum 147, National Advisory Committee for Aeronautics, 1922

[9] I. E. Garrick, "Propulsion of a flapping and oscillating airfoil," Technical Report 567, National Advisory Committee for Aeronautics, 1936

[10] T. Y. Wu, "Hydromechanics of Swimming Propulsion, Part 2: Some Optimum Shape Problems," *J. Fluid Mech.*, Vol. 46, No. 3, 1971, pp. 521-544.

[11] M. J. Lighthill, "Aquatic Animal Propulsion of High Hydromechanical Efficiency," *J. Fluid Mech.*, Vol. 44, No. 2, 1970, pp. 265-301.

[12] M. G. Chopra, "Large Amplitude Lunate-Tail Theory of Fish Locomotion," *J. Fluid Mech.*, Vol. 74, No. 1, 1976, pp. 161-182.

[13] K. D. Jones, C. M. Dohring, and M. F. Platzer, "Experimental and Computational Investigation of the Knoller-Betz Effect," *AIAA Journal*, Vol. 36, No. 7, 1998, pp. 1240-1246.

[14] R. Bhaskaran and A. P. Rothmayer, "Separation and instabilities in the viscious flow over airfoil leading edges," *Computers & Fluids*, Vol. 27, No. 8, 1998, pp. 903-921.

[15] K. Isogai, Y. Shinmoto, and H. Watanabe, "Effects of Dynamic Stall on Propulsive Efficiency and Thrust of Flapping Airfoil," *AIAA Journal*, Vol. 37, No. 10, 1999, pp. 1145-1151.

[16] I. H. Tuncer and M. F. Platzer, "Computational Study of Flapping Airfoil Aerodynamics," *Journal of Aircraft*, Vol. 37, No. 3, 2000, pp. 514-520.

[17] G. C. Lewin and H. Haj-Hariri, "Modelling thrust generation of a two-dimensional heaving airfoil in a viscous flow," *J. Fluid Mech.*, Vol. 492, 2003, pp. 339-362.

[18] I. H. Tuncer and M. Kaya, "Optimization of Flapping Airfoils for Maximum Thrust and Propulsive Efficiency," *AIAA Journal*, Vol. 43, No. 11, 2005, pp. 2329-2336.

[19] P. Freymuth, "Thrust generation by an airfoil in hover modes," *Experiments in Fluids*, Vol. 9, 1990, pp. 17-24.

[20] S. Sunada, K. Kawachi, A. Matsumoto, and A. Sakaguchi, "Unsteady Forces on a Two-Dimensional Wing in Plunging and Pitching Motions," *AIAA Journal*, Vol. 39, No. 7, 2001, pp. 1230-1239.

[21] J. C. S. Lai and M. F. Platzer, "Characteristics of a Plunging Airfoil at Zero Freestream Velocity," *AIAA Journal*, Vol. 39, No. 3, 2001, pp. 531-534.

[22] J. M. Anderson, K. Streitlien, D. S. Barrett, and M. S. Triantafyllou, "Oscillating foils of high propulsive efficiency," *J. Fluid Mech.*, Vol. 360, 1998, pp. 41-72.

[23] D. G. Bohl and M. M. Koochesfahani, "MTV measurements of the flow structure downstream of an oscillating airfoil," AIAA Paper 2003-4017, *33rd AIAA Fluid Dynamics Conference and Exhibit*, 2003.

[24] J. C. S. Lai and M. F. Platzer, "Jet Characteristics of a Plunging Airfoil," *AIAA Journal*, Vol. 37, No. 12, 1999, pp. 1529-1537.

[25] A. Ihara and H. Watanabe, "On the Flow Around Flexible Plates, Oscillating with Large Amplitude," *Journal of Fluids and Structures*, Vol. 8, No. 6, 1994, pp. 601-619.

[26] M. M. Koochesfahani, "Vortical patterns in the wake of an oscillating airfoil," *AIAA Journal*, Vol. 27, No. 9, 1989, pp. 1200-1205.

[27] F. S. Hover, O. Haugsdal, and M. S. Triantafyllou, "Effect of angle of attack profiles in flapping foil propulsion," *Journal of Fluids and Structures*, Vol. 19, 2004, pp. 37-47.

[28] G. Pedro, A. Suleman, and N. Djilali, "A numerical study of the propulsive efficiency of a flapping hydrofoil," *International Journal for Numerical Methods in Fluids*, Vol. 42, 2003, pp. 493-526.

[29] M. Sfakiotakis, D. M. Lane, and J. B. C. Davies, "Review of fish swimming modes for aquatic locomotion," *IEEE Journal of Oceanic Engineering*, Vol. 24, No. 2, 1999, pp. 237-251.

[30] R. J. Wootton, "Support and deformability in insect wings," *J. Zool., Lond.*, Vol. 193, 1981, pp. 447-468.

[31] S. J. Steppan, "Flexural stiffness patterns of butterfly wings (Papilionoidea)," *Journal of Research on the Lepidoptera*, Vol. 35, 2000, pp. 61-77.

[32] T. Maxworthy, "The Fluid Dynamics of Insect Flight," *Annu. Rev. Fluid Mech.*, Vol. 13, 1981, pp. 329-350.

[33] M. S. Triantafyllou, G. S. Triantafyllou, and D. K. P. Yue, "Hydrodynamics of fishlike swimming," *Annu. Rev. Fluid Mech.*, Vol. 32, 2000, pp. 33-53.

[34] J. Katz and D. Weihs, "Hydrodynamic Propulsion by Large Amplitude Oscillation of an Airfoil with Chordwise Flexibility," *J. Fluid Mech.*, Vol. 88, No. 3, 1978, pp. 485-497.

[35] M. M. Murray and L. E. Howle, "Spring stiffness influence on an oscillating propulsor," *Journal of Fluids and Structures*, Vol. 17, No. 7, 2003, pp. 915–926.

[36] J.-M. Miao and M.-H. Ho, "Effect of Flexure on Aerodynamic Propulsive Efficiency of Flapping Flexible Airfoil," *Journal of Fluids and Structures*, Vol. In Press, 2006

[37] M. M. Murray. "Hydroelasticity Modeling of Flexible Propulsors," Ph.D. Dissertation, Mechanical Engineering and Materials Science Dept., Duke Univ., Durham, NC, 2000.

[38] M. Bozkurttas, H. Dong, R. Mittal, P. Madden, and G. V. Lauder, "Hydrodynamic Performance of Deformable Fish Fins and Flapping Foils," AIAA Paper 2006-1392, *44th AIAA Aerospace Sciences Meeting and Exhibit*, 2006.

[39] S. Heathcote, D. Martin, and I. Gursul, "Flexible flapping airfoil propulsion at zero freestream velocity," *AIAA Journal*, Vol. 42, No. 22, 2004, pp. 2196-2205.

[40] K. D. Jones and M. F. Platzer, "Experimental investigation of the aerodynamic characteristics of flapping-wing micro air vehicles," AIAA Paper 2003-0418, *41st Aerospace Sciences Meeting & Exhibit*, 2003.

[41] P. Prempraneerach, F. S. Hover, and M. S. Triantafyllou, "The effect of chordwise flexibility on the thrust and efficiency of a flapping foil," *Proceedings of the Thirteenth International Symposium on Unmanned Untethered Submersible Technology*, 2003.

[42] G. K. Taylor, R. L. Nudds, and A. L. R. Thomas, "Flying and swimming animals cruise at a Strouhal number tuned for high power efficiency," *Nature*, Vol. 425, 2003, pp. 707-711.

[43] K. D. Jones, T. C. Lund, and M. F. Platzer, "Experimental and computational investigation of flapping wing propulsion for micro air vehicles," *Fixed and flapping wing aerodynamics for micro air vehicle applications*, edited by T. J. Mueller, Progress in Astronautics and Aeronautics, AIAA, Vol. 195, Virginia, 2001, pp. 307-339.

[44] J. Young and J. C. S. Lai, "Oscillation Frequency and Amplitude Effects on the Wake of a Plunging Airfoil," *AIAA Journal*, Vol. 42, No. 10, 2004, pp. 2042-2052.

[45] Z. J. Wang, "Vortex shedding and frequency selection in flapping flight," *J. Fluid Mech.*, Vol. 410, 2000, pp. 323-341.

[46] N. Vandenberghe, J. Zhang, and S. Childress, "Symmetry breaking leads to forward flapping flight," *J. Fluid Mech.*, Vol. 506, 2004, pp. 147-155.

[47] C. Van Den Berg and C. P. Ellington, "The vortex wake of a 'hovering' model hawkmoth," *Phil. Trans. R. Soc. Lond.*, Vol. 352, No. B, 1997, pp. 317-328.

[48] J. B. Bratt, "Flow Patterns in the Wake of an Oscillating Airfoil," Aeronautical Research Council, R&M 2773, 1953

[49] L. Schouveiler, F. S. Hover, and M. S. Triantafyllou, "Performance of flapping foil propulsion," *Journal of Fluids and Structures*, Vol. 20, 2005, pp. 949-959.

[50] M. S. Chandrasekhara and L. W. Carr, "Flow Visualization Studies of the Mach Number Effects on the Dynamic Stall of an Oscillating Airfoil," AIAA Paper 89-0023, *27th Aerospace Sciences Meeting*, 1989.

[51] T. Theodorsen, "General theory of aerodynamic instability and the mechanism of flutter," Technical Report 496, NACA, 1935

[52] K. D. Jones, S. J. Duggan, and M. F. Platzer, "Flapping-wing propulsion for a micro air vehicle," AIAA Paper 2001-0126, *39th Aerospace Sciences Meeting & Exhibit*, 2001.

[53] K. D. Jones and M. F. Platzer, "Numerical computation of flapping-wing propulsion and power extraction," AIAA Paper 97-0826, *35th Aerospace Sciences Meeting & Exhibit*, 1997.

[54] N. H. Teng. "The development of a computer code for the numerical solution of unsteady, inviscid and incompressible flow over an airfoil," Master's Thesis, Aeronautics and Astronautics, Naval Postgraduate School Univ., Monterey, CA, 1987.

[55] J. L. Hess and A. M. O. Smith, "Calculation of Potential Flow About Arbitrary Bodies," *Progress in Aeronautical Sciences*, Vol. 8, 1966, pp. 1-138.

[56] J. Young. "Numerical Simulation of the Unsteady Aerodynamics of Flapping Airfoils," Ph.D. Dissertation, School of Aerospace, Civil and Mechanical Engineering, New South Wales Univ., Canberra, 2005.

[57] G. R. Srinivasan, J. A. Ekaterinaris, and W. J. McCroskey, "Evaluation of turbulence models for unsteady flows of an oscillating airfoil," *Computers & Fluids*, Vol. 24, No. 7, 1995, pp. 833-861.

[58] K. Hannemann and H. Oertel, "Numerical Simulation of the Absolutely and Convectively Unstable Wake," *J. Fluid Mech.*, Vol. 199, 1989, pp. 55-88.

[59] P. Liu and N. Bose, "Propulsive performance from oscillating propulsors with spanwise flexibility," *Proc. R. Soc. Lond.*, Vol. 453, 1997, pp. 1763-1770.

[60] J. E. Emblemsvag, R. Suzuki, and G. V. Candler, "Numerical simulation of flapping micro air vehicles," AIAA Paper 2002-3197, *32nd Fluid Dynamics Conference and Exhibit*, 2002.

[61] K. D. Frampton, M. Goldfarb, D. Monopoli, and D. Cveticanin, "Passive Aeroelastic Tailoring for Optimal Flapping Wings," *Fixed and Flapping Wing Aerodynamics for Micro Air Vehicle Applications*, edited by T. J. Mueller, Progress in Astronautics and Aeronautics, AIAA, Vol. 185, Virginia, 2001, pp. 473-482.

[62] H. Liu, R. J. Wassersug, and K. Kawachi, "A Computational Fluid Dynamics Study of Tadpole Swimming," *Journal of Experimental Biology*, Vol. 199, 1996, pp. 1245-1260.

[63] R. E. Sheldahl and P. C. Klimas, "Aerodynamic Characteristics of Seven Symmetrical Airfoil Sections Through 180-Degree Angle of Attack for Use in Aerodynamic Analysis of Vertical Axis Wind Turbines," Technical Report SAND80-2114, Sandia National Laboratories, 1981

[64] K. D. Jones, B. M. Castro, O. Mahmoud, S. J. Pollard, M. F. Platzer, M. F. Neef, K. Gonet, and D. Hummel, "A collaborative numerical and experimental investigation of flapping-wing propulsion," AIAA Paper 2002-0706, *40th Aerospace Sciences Meeting & Exhibit*, 2002.

[65] K. Streitlien and G. S. Triantafyllou, "On thrust estimates for flapping foils," *Journal of Fluids and Structures*, Vol. 12, No. 1, 1998, pp. 47-55.

[66] C. M. Dohring, M. F. Platzer, K. D. Jones, and I. H. Tuncer, "Computational and experimental investigation of the wakes shed from flapping airfoils and their wake interference/impingement characteristics," *78th AGARD Fluid Dynamics Panel Symposium*, 1996.

[67] K. D. Jones and M. F. Platzer, "An experimental and numerical investigation of flapping-wing propulsion," AIAA Paper 99-0995, *37th Aerospace Sciences Meeting & Exhibit*, 1999.

[68] J. E. Emblemsvag, R. Suzuki, and G. V. Candler, "Simulation of a three-dimensional flapping cantilever for micro air vehicle propulsion," AIAA Paper 2003-4012, *33rd AIAA Fluid Dynamics Conference*, 2003.

[69] M. F. Platzer and K. D. Jones, "Flapping Wing Aerodynamics - Progress and Challenges," AIAA Paper 2006-500, *44th AIAA Aerospace Sciences Meeting and Exhibit*, 2006.

[70] I. H. Tuncer, R. Walz, and M. F. Platzer, "A Computational Study of the Dynamic Stall of a Flapping Airfoil," AIAA Paper 1998-2519, *16th AIAA Applied Aerodynamics Conference*, 1998.

[71] R. Ramamurti and W. C. Sandberg, "Simulation of Flow About Flapping Airfoils Using Finite Element Incompressible Flow Solver," *AIAA Journal*, Vol. 39, No. 2, 2001, pp. 253-260.

[72] K. V. Rozhdestvensky and V. A. Ryzhov, "Aerohydrodynamics of flapping-wing propulsors," *Progress in Aerospace Sciences*, Vol. 39, No. 8, 2003, pp. 585-633.

[73] D. A. Read, F. S. Hover, and M. S. Triantafyllou, "Forces on oscillating foils for propulsion and maneuvering," *Journal of Fluids and Structures*, Vol. 17, 2003, pp. 163-183.